Bangor University

DOCTOR OF PHILOSOPHY

The application of acoustic doppler techniques to the measurement of turbulent flow over mussel beds : new techniques and applications.

Wiles, Philip J.

Award date:
2007

Awarding institution:
University of Wales, Bangor

The Application of Acoustic Doppler Techniques to the Measurement of Turbulent Flow Over Mussel Beds.

New techniques and applications

Philip J. Wiles

Abstract

The quest for sustainable fisheries has been accompanied by a rapid expansion of the aquaculture industry worldwide. In order to investigate the effects of commercial mussel beds on the surrounding environment it is necessary to understand the coupling of the benthic mussels to the overlying water column. Vertical transport of plankton, nutrients and oxygen to benthic mussels is usually dominated by turbulent processes. This thesis investigates vertical mixing at 2 field sites which were used in the European Union framework 5 project MaBenE (Management of Benthic Ecosystems in relation to physical forcing and environmental constraints).

The first site is the Limfjorden in Denmark, where vertical mixing is driven by meteorological forcing. Because the turbulence levels were generally too low for the ADCP techniques to provide meaningful turbulence data, a water column potential energy model is developed. The model incorporates surface heat exchange, wind mixing and wave mixing. It is found that the significant wave height is the most appropriate parameter to represent the meteorological forcing of turbulence.

The second site is the Oosterschelde in The Netherlands. The strong tides in this embayment produce relatively high levels of turbulence, which can be detected using the ADCP techniques. Analysis of the turbulence generated over a mussel bed and a sand site allow the comparison of bottom drag coefficients which were 0.0032 over mussels and 0.0026 over sand.

An overview of turbulence in the bottom boundary layer is presented, along with a description of the ADCP techniques employed and developed during these studies. A description of the field sites is followed by results from the observational campaigns. The thesis finishes with a discussion of the results, comparing the two different study sites and the differences in turbulence over mussel beds and sand.

Acknowledgements

I owe thanks to a large number of people. First and foremost my supervisor John Simpson, whose patience, insight and skill at explaining concepts is invaluable. His ability to keep an eye on proceedings while giving me enough responsibility to make mistakes and learn from them was very much appreciated. The School of Ocean Sciences in Menai Bridge provided a fertile environment in which to pose questions and receive well thought answers. In particular, Tom Rippeth always has an open door and provides a warm reception. The surrounding post docs and contemporary PhD students, Neil Fisher, Graeme Riley, Eirwen Williams, Kath Ellis, Matt Palmer, Mattias Greene, Ole Mikkelson, Pete Sykes, Barbara Berx and Biz Kyte provided a wide range of experience and knowledge against which to bounce ideas.

Ben Powell was invaluable in preparing for and carrying out the fieldwork and also gave a fresh view on the scientific matters at hand. He also proved a great travelling companion and entertaining company whilst on the road around the mussel sites throughout Europe. Gwyn Parry-Jones and Ray Wilton gave the technical expertise required for the Menai Strait fieldwork. Peter Hendricks, Alex Nimmo Smith, Steve Thorpe, Tom Osborn and Anne Gargett were a thorough board of questioners while developing the structure function manuscript. Financial support from DSTL, managed by Bob Hornby, was very much appreciated.

The members of the MaBenE consortium cheerily explained basic ecological and biological principles to a novice. Specifically, Luca van Duren linked the physical processes to the mussels themselves and Peter Herman provided good, clear leadership within the project. Tom Ysebaert, Jens Petersen, Jens Larsen, Torkel Nielsen, Birgit, Rolf Riethmüller, Clivia Häse, Hans Burchard, Karsten Bolding and the Iberians; Paco, Isabel Teixera, Bibiana, Ramiro, Luis Fernandes and Sophia were great to work with and left some very good memories of the MaBenE field campaigns. MaBenE was a European Union framework 5 project, number EVK3-CT-2002-00071.

From a personal viewpoint, the Menai Bridge community has been an extremely friendly and welcoming environment to live in. The opportunity to take out frustrations legally on a rugby pitch with friends from the Porthaethwy Rugby Club was needed at times. My family; Mum, Dad, Janine, Nat and Jeremy have often listened to me rant about turbulence and mussels which allowed basic concepts to form in my own head Lucy Jacob over the last 2 years has been superb. I'm forever indebted to Lucy for the time, love, support and perspective she's given me.

Table of Contents

List of Figures

List of Tables

Definitions

Acronyms

ADCP	Acoustic Doppler Current Profiler
ADV	Acoustic Doppler Velocimeter
CBL	Concentration Boundary Layer
CTD	Conductivity Temperature Depth instrument
FLY	Fast Light Yo-yo turbulence profiler
GETM	Generalised Estuarine Transport Model
SWH	Significant Wave Height
TKE	Turbulent Kinetic Energy

Operators

~	Denotes an instantaneous variable (e.g. $\tilde{u}$ is an instantaneous velocity)
–	Time average (e.g. $\overline{u}$)
‘	Fluctuating component (e.g. u‘)
i	Denotes i^{th} component (e.g. u_2 is a velocity in the y direction)

Variables

α	Thermal expansion coefficient (K^{-1})
γ	Ratio of surface current speed to wind speed
δ	Wind mixing efficiency
δ_{ij}	Kronecker delta function ($\delta_{ij} = \begin{matrix} 0, i \neq j \\ 1, i = j \end{matrix}$)
ε	Rate of turbulence dissipation ($W\ m^{-3}$).
η	Wave mixing efficiency
θ	Angle of the ADCP beam from vertical (°)
κ	Von Karman’s constant (0.41)
λ	Wavelength (m)
ρ	Density ($kg\ m^{-3}$)
ρ_a	Density of air (~ 1 $kg\ m^{-3}$)
ρ_0	Ambient density (~ 1025 $kg\ m^{-3}$ for seawater)
σ	Wave angular frequency

σ_N	Doppler noise of along beam velocities (m s^{-1})
τ_{ij}	ij^{th} component of the stress tensor (Pa).
τ_b	Bed shear stress (Pa)
υ	Kinematic viscosity (~10^{-6} m^2 s^{-1} for sewater)
φ	Water column stability (J m^{-3})
φ_2	ADCP pitch (°)
φ_3	ADCP roll (°)
ψ	Tidal stirring efficiency
ω	Angular frequency (s^{-1})
A	Albedo
Amp	Wave amplitude (m)
b_i	Along beam velocity of i^{th} beam. (+ ve indicates away from the ADCP)
C_{200}	Sea bed drag coefficient relative to 2m above the bed
C_d	Wind drag coefficient of the sea surface
C_v^2	Structure function constant
c	General concentration
c_d	Standard seabed drag coefficient (0.0025)
c_p	Heat capacity (~ 4×10^3 J kg^{-1} K^{-1} for seawater)
$D(z,r)$	2^{nd} order structure function (m^2 s^{-2})
e	ADCP error velocity (m s^{-1})
e_{ij}	Strain tensor (s^{-1})
$G(kh)$	Shallow water correction for surface radiative stabilising effect
K_z	Vertical turbulent eddy diffusivity
g	Gravity (9.81 m s^{-1})
h	Water depth (m)
k	Tidal stirring efficiency
l_k	Kolmogorov scale (m)
l_o	Ozmidov scale (m)
N	Noise in structure function (m s^{-1})
N_z	Vertical turbulent eddy viscosity (m^2 s^{-1})
P	TKE shear production (W m^{-3})
p	Pressure (Pa)
Q	Surface heat flux (J m^{-2})

Q_s	Incoming short wave radiation heat flux (J m^{-2})
Q_e	Evaporative heat flux (J m^{-2})
Q_b	Long wave radiation heat flux (J m^{-2})
Q_c	Sensible heat flux (J m^{-2})
r	Length scale (m)
SWH	Significant wave height (m)
s	Velocity scale (m s^{-1})
T	Temperature (°C)
T_0	Ambient temperature (°C)
T_w	Wave period (s)
TKE	Turbulent Kinetic Energy (J m^{-3})
t	Time (s)
u_*	Friction velocity (m s^{-1})
W	Wind speed (m s^{-1})

1 Introduction

The mechanisms of turbulence in geophysics - and oceanography in particular - are still being revealed. Important steps regarding the theory of fundamental processes in turbulence were formulated many decades or even centuries ago, da Vinci described the slow decay of turbulence in around 1500 as:

"where the turbulence of water is generated
where the turbulence of water maintains for long
where the turbulence of water comes to rest"

(Frisch, 1995). Over the last century, turbulence has been described in a more rigorous mathematical framework (Kolmogorov, 1941: Taylor, 1938). Advances in technology have allowed investigators to test, adjust and advance these hypotheses against processes in the real world (Turner, 1981).

The aim of this thesis is to develop and evaluate methods for estimating turbulence parameters around commercial mussel beds. The study was undertaken within the framework of a larger European Union project, MaBenE (**Ma**nagement of **Ben**thic **E**cosystems in Relation to physical forcing and environmental constraints) using Acoustic Doppler Current Profilers (ADCPs - RDInstruments, 1996). The overall goal of MaBenE is to investigate processes affecting commercial mussel beds, and to adapt two 3D numerical models (GETM and Mohid) to accurately model physical, ecological and chemical processes around commercial mussel beds in order to increase yield, prevent eutrophication and optimise environmental quality and biodiversity. Both models include turbulence closure schemes – which parameterise turbulent coefficients (e.g. vertical diffusion, turbulent kinetic energy production and dissipation) by large scale flow characteristics (e.g. mean velocity, velocity shear, stratification, etc.). This is a process employed by almost all modern geophysical flow models attempting to accurately simulate large scale fluid movement while using realistic computational resources. A complete turbulence closure scheme has not yet been achieved, indeed modern hydrodynamic models often need to use unrealistically large background turbulent viscosities (by up to a factor of 10 larger than those observed Rippeth, 2005) in order to produce accurate results. The validation of turbulence closure schemes by measuring turbulence in the marine environment is an ongoing development.

A major advance in technology allowing direct measurement of turbulence in the marine environment is the development of ADCPs . The capacity of these devices to remotely estimate mean currents has attained 'turn-key' status, so that operators with minimal training can plan and execute fieldwork with relative ease. The capability of ADCPs to remotely estimate turbulence in water was identified by Pinkel (1979) at an early stage in acoustic Doppler developments.

The approach taken in this thesis is to exploit the potential of ADCPs to estimate turbulent parameters around regions of mussel aquaculture. This involves evaluating innovative methods such as the variance method (Lohrmann *et al.*, 1990, Rippeth *et al.*, 2003), and also developing new approaches, such as the structure function method (Wiles, Rippeth *et al.*, 2006). Apart from ADCP techniques, other approaches used to estimate turbulence in estuaries include microstructure profiling instruments (Peters *et al.*, 2001), dye diffusion experiments (Oakey *et al.*, 2004) and point measurements (e.g. Acoustic Doppler Velocimeteres – ADVs, Nikora *et al.*, 1998 - see next chapter). Microstrucure profiling instruments and dye diffusion experminents are limited by the intensive labour and ship time required while ADV's are limited to a single point measurement. In contrast, an ADCP can observe turbulence profiles over large sections of the water column for extended periods of time, limited only by the battery life and memory capacity.

Turbulent diffusion is often the dominant process transporting phytoplankton vertically through the water column. Phytoplankton sinking can also be important, at times, depending on the phytoplankton settling veocities. Benthic mussel communities filter phytoplankton from water in their local vicinity and create a 'concentration boundary layer' - which is a layer of water near the mussels with a low phytoplankton concentration (Wildish *et al.*, 1984). This concentration boundary layer can also become low in dissolved oxygen due to respiration by the mussel community (Herman *et al.*, 1999). The combination of these effects can drastically affect benthic mussel populations. The replenishment of concentration boundary layers can usually be attributed to turbulence. In the case studies presented in this thesis, turbulence is driven by wind in the Limfjorden and by tides in the Oosterschelde. The capacity of ADCPs to measure turbulence over much of the water column and over extended periods of time allows us to observe the cycles of turbulence over mussel beds and link this to vertical transport of phytoplankton, nutrients, etc. to the mussels. A hypothesis has been proposed that mussels themselves can act to enhance turbulence through a larger bed roughness, this hypothesis is to be tested with the results in this thesis.

The three field sites chosen for the MaBenE campaigns are among the largest mussel farming regions in Europe and each is characterised by different driving physical forces. Limfjorden, in Denmark, is a micro tidal estuary, where the hydrodynamics are driven predominantly by meteorological forcing. There is a mean horizontal flow through the estuary from west to east driven by atmospheric barotropic pressure differences and vertical mixing is driven by wind and wave forcing. By contrast, the Oosterschelde in The Netherlands is a macrotidal estuary. Tidal currents are principally driven by exchange with the North Sea through a storm surge barrier and vertical exchange is dominated by bed generated turbulence. The third MaBenE field site, which is not included in this thesis, is the Ria de Vigo, in Spain, where phytoplankton supply to mussel rope cultures is strongly influenced by offshore seasonal upwelling.

Mussel aquaculture is a booming industry worldwide and has increased exponentially since the 1950s (figure 1.1). Mussel landings in Spain have increased from low levels in 1960 to well over 200,000 tonnes per annum. However the most marked increase in production has been in China where production was over 700,000 tonnes in 2004, which is similar to the figure for combined production throughout the rest of the world. The wealth and jobs generated by the industry have a major effect in often economically deprived regions. Understanding the environmental impacts of this anthropogenic disturbance is essential for mussel aquaculture sustainability.

The measurement of turbulence in relation to ecology has implications beyond mussels, aquaculture and even the marine environment. Turbulence controls the supply of many basic properties to and from organisms – for example food, oxygen, nutrients and waste products. This can determine where individuals and communities place themselves within their environment and how they interact with each other.

This thesis is structured so that the reader is first introducted to the basic parameters of turbulence and then the ADCP and the Doppler methods to be used (chapter 2). A detailed account of the new structure function method and it's validation is given in chapter 3. The application to measurements at two of the MaBenE sites follows with site descriptions in chapter 4 and the observational strategies in chapter 5. The results of the two campaigns are presented in chapters 6 and 7 before the final chapter 8, which recaps the main results and discusses their significance.

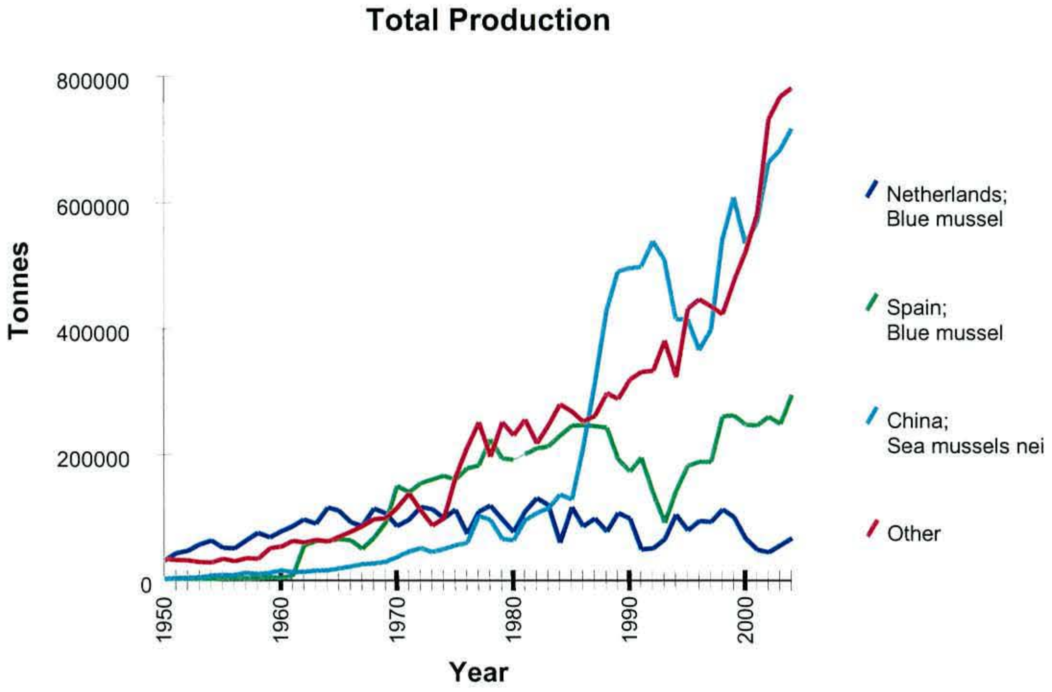

Figure 1.1. Mussel production in some major regions around the world from the period 1950-2004 (Food and Agriculture Organisation of the United Nations).

2 Introduction to turbulence parameters used.

Throughout this thesis, various stastistical parameters will be used to describe turbulence in the vicinity of mussel beds. A brief introduction is given here which follows Kundu (1990).

The flows considered here are in shallow (< 10 m) water, are considered to be unstratified and are relatively far from lateral boundaries. Hence the flow can be considered as a bottom-bounded shear flow. The turbulent parameters relevant to understanding this turbulent environment are the Reynolds stresses, the eddy viscosity and the rates of production and dissipation of turbulent kinetic energy. This chapter introduces these concepts by decomposing the Navier Stokes equations into it's mean and fluctuating parts.

2.1 The Navier Stokes equations

If it is assumed that density variations are caused by temperature fluctuations alone (ignoring salinity effects for simplification) and under the Boussinesq approximation, the instantaneous equations of fluid motion are the momentum equation:

Equation 2.1
$$\frac{D\tilde{u}_i}{Dt} = -\frac{1}{\rho_0}\frac{\partial \tilde{p}}{\partial x_j} - g\left[1-\alpha\left(\tilde{T}-T_0\right)\right]\delta_{i3} + \frac{\partial}{\partial x_j}\left(\upsilon\frac{\partial \tilde{u}_i}{\partial x_j}\right)$$

The continuity equation:

Equation 2.2
$$\frac{\partial \tilde{u}_i}{\partial x_i} = 0$$

And the scalar transport equation:

Equation 2.3
$$\frac{\partial \tilde{T}}{\partial t} + \tilde{u}_j\frac{\partial \tilde{T}}{\partial x_j} = \kappa\frac{\partial^2 \tilde{T}}{\partial x_j \partial x_j}$$

The instantaneous variables (denoted by a tilde) can be broken into their mean (denoted by an overbar) and a fluctuating (denoted by a prime) components, i.e.

Equation 2.4
$$\tilde{u}_i = \overline{u} + u'$$
$$\tilde{p} = \overline{p} + p'$$
$$\tilde{T} = \overline{T} + T'$$

2.2 Reynolds Stresses

Substituting equation 2.4 into equation 2.1 gives the momentum equation for the mean water velocities:

Equation 2.5 $$\frac{D\overline{u}_i}{Dt} = -\frac{1}{\rho_0}\frac{\partial \overline{p}}{\partial x_i} - g\left[1-\alpha\left(\overline{T}-T_0\right)\right]\delta_{i3} + \frac{\partial}{\partial x_j}\left(\upsilon\frac{\partial \overline{u}_i}{\partial x_j} + \overline{u_i'u_j'}\right)$$

which is identical to the momentum equation for instananeous velocities (equation 2.1) except for the third term on the right. The first term in the brackets is the viscous stress and the second term is the turbulent Reynolds stress tensor. In a turbulent flow, the Reynolds stresses are generally much larger than the viscous stresses.

The Reynolds stress tensor has 9 cartesian components and is symmetric:

$$\tau = -\rho_0\begin{bmatrix} \overline{u'^2} & \overline{u'v'} & \overline{u'w'} \\ \overline{u'v'} & \overline{v'^2} & \overline{v'w'} \\ \overline{u'w'} & \overline{v'w'} & \overline{w'^2} \end{bmatrix}$$

If the turbulent flucuations are completely isotropic, then the off-diagonal terms become zero (see section 3.3.1).

The component $\overline{u'w'}$ of the tensor represents the vertical transport of horizontal momentum which is conceptualised in figure 2.1. If a shear flow exists where velocity increases with height, then as a parcel of water is moved upwards (by a turbulent fluctuation), it carries less momentum than the water it moves up into. The flow above is therefore decreased. Conversely, if a parcel of water is moved down, it carries more momentum than the water it moves into, and hence it increases the speed of the lower water level. The shear is thus 'smeared' or diffused through the water column.

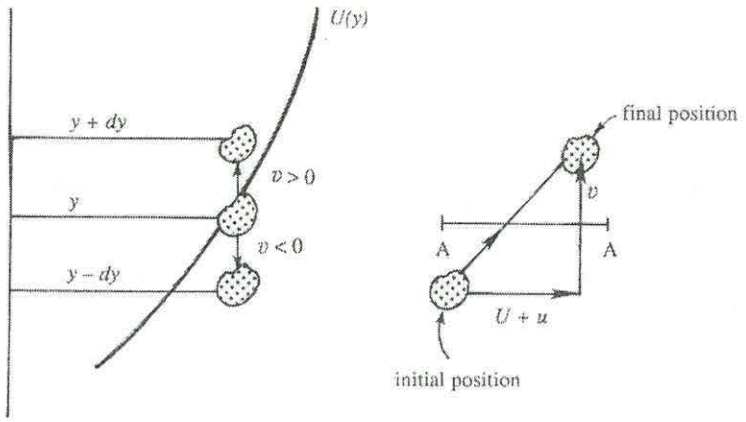

Figure 2.1. Movement of a particle in turbulent shear flow (from Kundu, 1990).

2.3 The Turbulent Kinetic Energy (TKE) Equation

Using equation 2.1 to obtain an expression for $\frac{\partial \widetilde{u}}{\partial t}$ then multiplying this by $\widetilde{u}$ gives an equation for the turbulent kinetic energy budget:

Equation 2.6

$$\underbrace{\frac{D\left(\frac{1}{2}u_i'^2\right)}{Dt}}_{\substack{\text{change in}\\ \text{TKE w.r.t.}\\ \text{time}}} = \underbrace{-\overline{u_i'u_j'}\frac{\partial \overline{u_i}}{\partial x_j}}_{\substack{\text{shear}\\ \text{production}}} + \underbrace{g\alpha\overline{u_3'T'}}_{\substack{\text{buoyant}\\ \text{production}}} - \underbrace{2\upsilon\overline{e_{ij}e_{ij}}}_{\substack{\text{viscous}\\ \text{dissipation}}} - \underbrace{\frac{\partial}{\partial x_j}\left(\frac{\overline{p'u_j'}}{\rho_0} + \frac{1}{2}\overline{u_i'^2 u_j'} - 2\upsilon\overline{u_i'e_{ij}}\right)}_{\text{transport}}$$

where e_{ij} is the strain tensor:

Equation 2.7 $$e_{ij} \equiv \frac{1}{2}\left(\frac{\partial u_i}{\partial x_j} + \frac{\partial u_j}{\partial x_i}\right)$$

The term on the left and side is the change in TKE over time. Writing the TKE in normal cartesian coordinates gives the TKE as:

Equation 2.8 $$TKE = \frac{1}{2}\rho\left(\overline{u'^2} + \overline{v'^2} + \overline{w'^2}\right)$$

2.4 TKE Production

The first two terms on the right side of equation 2.6 are the sources of turbulent energy.

2.4.1 Shear production

The shear production is the energy converted from the mean flow to turbulence by friction and is given by the dot product of the mean shear and the Reynolds stress. In a bottom boundary layer where the shear is in the horizontal plane, this becomes (expressed in normal cartesian coordinates),

Equation 2.9 $$P = -\left(\overline{u'w'}\frac{\partial \overline{u}}{\partial z} + \overline{v'w'}\frac{\partial \overline{v}}{\partial z}\right)$$

which will usually have a positive value.

2.4.2 Buoyant production

Buoyant production is the interaction of turbulence with the mean density stratification. If the stratification is stable, then turbulence will act to mix denser water higher into the water column, thereby taking energy away from turbulence – in this case the buoyancy term will be negative. If the stratification is unstable (e.g. caused by cooling from above or heating from below), then relaxation of the instability transfers energy to turbulence – in this case the buoyancy term will be positive.

2.5 Viscous dissipation

The third term on the right is the rate of viscous dissipation of turbulent kinetic energy, denoted by the symbol ε. As turbulent fluctuations decrease in size to the Kolmogorov micro-scale, viscosity dissipates the turbulent energy into heat via friction. Under isotropic conditions, the viscous dissipation term reduces to

Equation 2.10 $$\varepsilon = 7.5\overline{\left(\frac{\partial u'}{\partial z}\right)^2}$$

The value of $\partial u'/\partial z$ and hence dissipation rates can be estimated in the marine environment by the use of microstructure shear probes (Baumert *et al.*, 2005).

2.6 Balance between P and ε

Under certain assumptions, the TKE equation (equation 2.6) can be simplified. If the environment is in steady state, then the left hand side is equal to zero. If there is no or limited stratification and no cooling or salt water flux from above, the buoyant production term is equal to zero. If there is lateral uniformity, then horizontal parts of the transport term are also equal to zero. Our current state of knowledge suggests that usually the vertical diffusion of TKE is negligible compared to the production and dissipation terms. Hence the TKE equation can be simplified to:

Equation 2.11 $$-\overline{u_i'u_j'}\frac{\partial \overline{u_i}}{\partial x_j} \approx 2\upsilon e_{ij}e_{ij}$$

or to clarify even further:

Equation 2.12 $$P \approx \varepsilon$$

i.e. the rate of production of turbulent kinetic energy is about equal to the rate of dissipation of turbulent kinetic energy.

2.7 Eddy viscosity

Turbulence breaks down large gradients of scalars both by transporting the scalar and by increasing gradients at the viscous scale. When considering the transport of properties in a turbulent flow, it is impractical to identify each individual turbulent fluctuation and it's implications. It is therefore useful to parameterise this transport by the mean state of the flow.

The diffusion of a gradient by turbulence can be represented by a diffusion parameter K_z. For example considering the vertical turbulent flux of a scalar, c, in a vertical gradient gives:

Equation 2.13 $$Flux_{turbulent} = \overline{c'u_3'} = K\frac{\overline{\partial c}}{\partial x_3}$$

Similarly, turbulence acts to smooth a velocity gradient by diffusing momentum across the gradient (via the Reynolds stresses).

Equation 2.14 $$N_z = \frac{\overline{u_i'u_j'}}{\partial u_i / \partial x_j}$$

i.e. the diffusion of momentum is governed by the eddy viscosity N_Z.

In a well mixed turbulent flow, the diffusivity of scalars is similar to the diffusivity of momentum, and the ratio of N_z/K_z (also known as the Prandtl number) is about 1 (Kundu, 1990).

2.8 Law of the wall.

Dimensional analysis near a flat bottom boundary in a homogeneously turbulent flow suggests that shear is inversely proportional to the distance from the boundary,

Equation 2.15 $$\frac{\partial U}{\partial z} = \frac{u_*}{\kappa z}$$

where κ is von Karman's constant, which has been empirically found to be 0.41.

Upon integration with respect to z, this gives the logarithmic velocity profile,

Equation 2.16 $$U(z) = \frac{u_*}{\kappa} \ln\left(\frac{z}{z_0}\right)$$

where u_* is the friction velocity of the flow (see below) and z_o is the roughness length. This relation holds from the region far enough from the wall such that viscous effects are no longer important out to a range of $0.03 - 0.04 u_* \omega^{-1}$ where ω is the angular frequency of an oscillating tidal current, e.g. 1.4×10^{-4} s^{-1} for a M2 tide (Sanford *et al.*, 1999).

2.9 Turbulent length scales

Two length scales are used in this thesis. The first is the Ozmidov scale (l_0), which is the size of the largest eddies that can overturn in a stable stratified water column. This is given by

Equation 2.17 $$l_0 = \left(\frac{\varepsilon}{N^3}\right)^{\frac{1}{2}}$$

where N is the buoyancy freqency, given by $N^2 = -\frac{g}{\rho_0}\left(\frac{\partial \rho}{\partial z}\right)$. The Ozmidov scale increases with increasing turbulence dissipation rates and decreases with increased stratification.

The second length scale is the Kolmogorov microscale (l_k), which is the scale at which turblent motions become dominated by friction and are dissipated to heat. The Kolmogorov scale is given by

Equation 2.18 $$l_k = \left(\frac{\upsilon^3}{\varepsilon}\right)^{\frac{1}{4}}$$

3 Acoustic Doppler Methods

The Acsoutic Doppler Current Profiler (ADCP) was developed to non-invasively measure water velocities throughout the water column using the acoustic Doppler shift from passive scatterers (figure 3.1). This has provided a remarkably effective tool that has transformed velocity measurements in oceanography. Previous *in–situ* measurements of water velocity were made either using mechanical current meters based on a design pioneered by Ekman in 1905 or on electromagnetic current meters which exploit the voltage potential created by conductive seawater moving in a magnetic field. Both of these approaches provided only point measurements and the physical presence of the current meters themselves affected the local water velocities measured. By contrast, the ADCP measures a profile of velocities throughout the water column, as it's name implies. The instrument itself is not located in the measuring volume, so does not affect the measured flow.

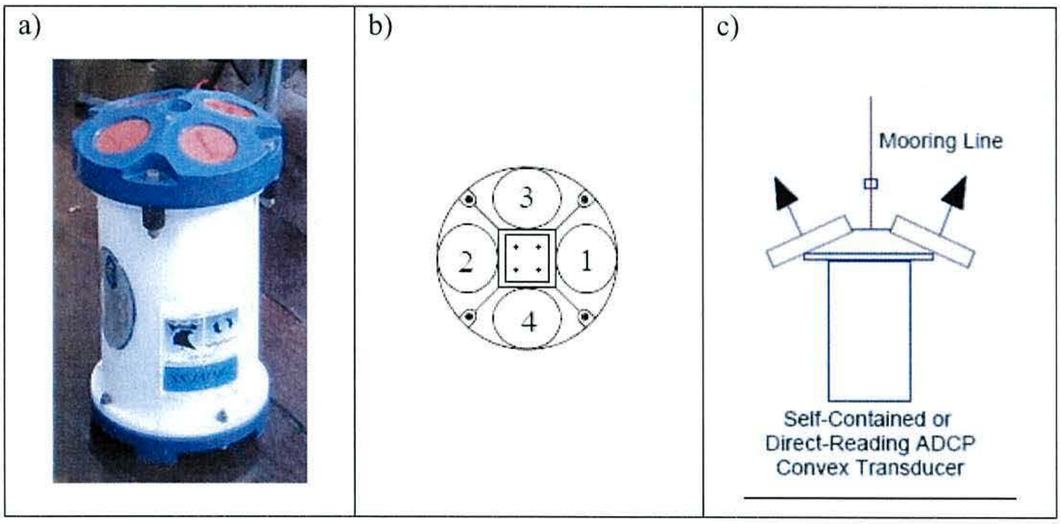

Figure 3.1. a) An ADCP manufactured by RDI (courtesy of Ben Powell). b) the beam layout of the ADCP viewed from above. c) the 'Janus' or convex configuration used by the ADCPs discussed in this thesis (also see figure 3.4) Taken from RDInstruments (1996).

3.1 *Acoustic Doppler measurement of water velocity*

The ADCP measures currents remotely by using the Doppler effect. In the original 'narrow-band' ADCP, a short pulse of sound with a specific frequency is sent out along a narrow 'pencil' beam from the ADCP. The sound bounces off particles in the water (figure 3.2). If the particles are moving, the scattered sound is Doppler shifted. By assuming the particles are passively drifting with the water currents, this gives a measure of the water velocity. The accuracy of the water velocity measurement is therefore determined by the accuracy of the Doppler shift measurement. If larger bin sizes are used, there is a greater scattering volume, so the Doppler shift can be measured more accurately, however the vertical resolution is diminished. ADCPs with a higher frequency (the current maximum is 1200 kHz) can measure velocities with greater accuracy and vertical resolution, however the range of the ADCP is limited to ~ 20m. ADCPs with lower frequencys (the current minimum is 75 kHz) can measure much greater range (up to 1000m), however the accuracy and vertical resolution are compromised.

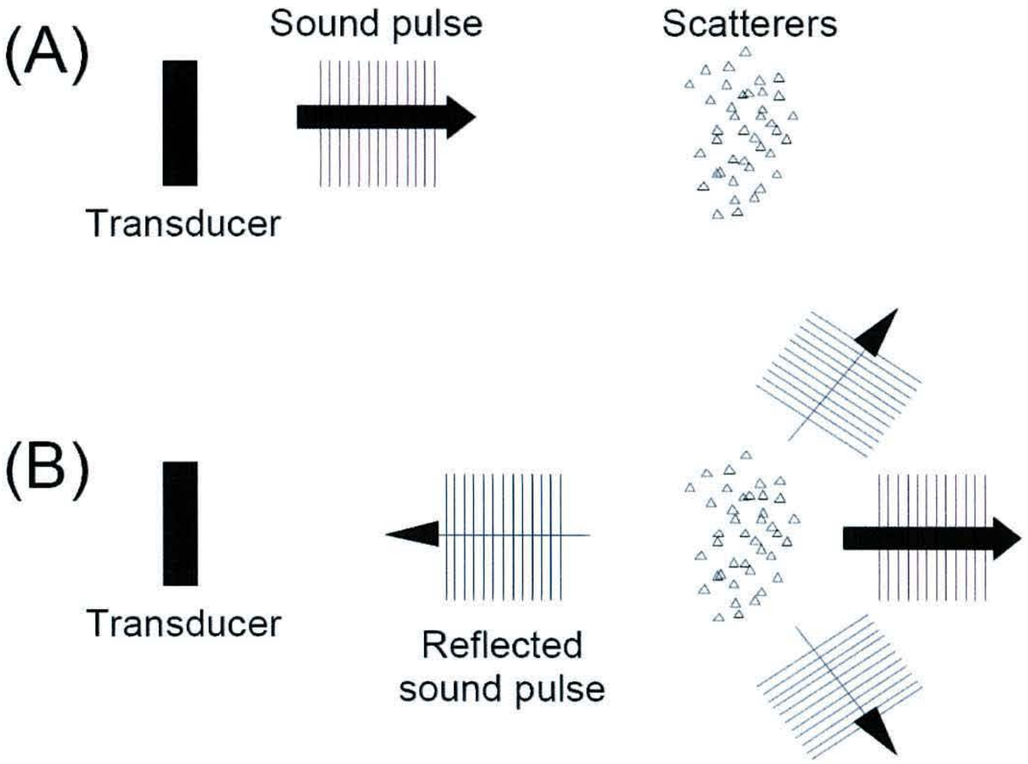

Figure 3.2. The ADCP employs a Doppler shift to measure velocities. (a) a precise frequency narrow beam of sound is sent from the ADCP transducer. (b) The sound bounces off scatterers in the water. The reflected sound pulse is Doppler shifted according to the speed of the particles. In a narrow-band ADCP, the transducer measures the change in frequency and hence the speed of the particles (from RDInstruments, 1996).

The introduction of 'broad-band' technology (patented by RDInstruments) has made the Doppler shift (and hence velocity) measurement more accurate (figure 3.3). A broad band ADCP transducer sends two acoustic pulses separated by a short period of time. The phase change between the returned Doppler pulses is determined by the distance the scatterers have moved in that time period, giving the velocity of the scatterers. The shorter pulses allow more accurate velocity readings and smaller depth cells (hence higher resolution in the vertical).

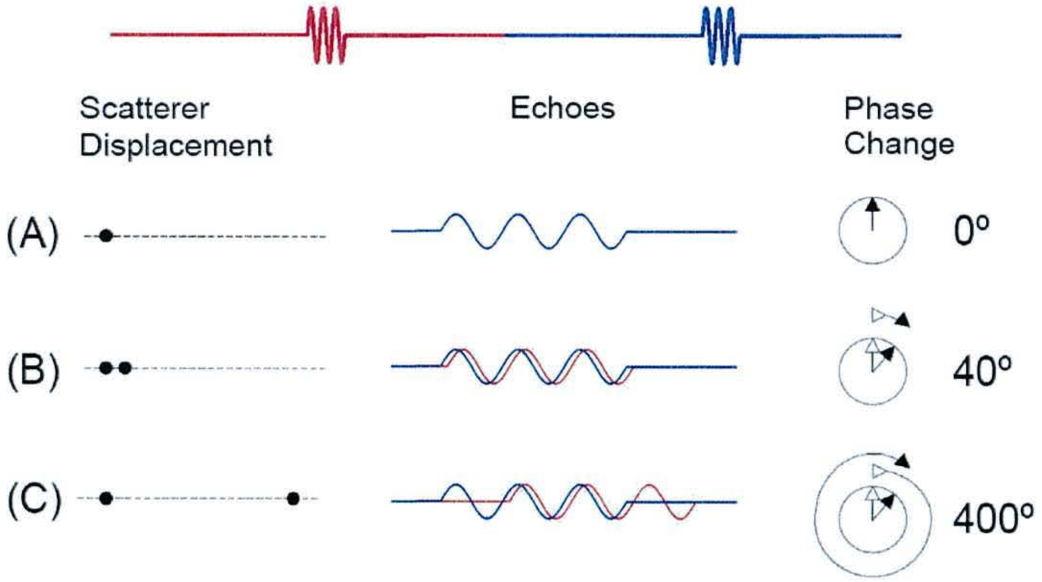

Figure 3.3. Broadband processing. Two short acoustic pulses are sent from the transducer, illustrated as the blue (first) and red (second) pulses at the top of the figure. The two pulses reflect off scatterers in the water and return to the transducer. If the scatterers are stationery, then there is no phase change, and the sound waves overly each other as shown in (a). If the scatterers have moved a small distance during the interval between the acoustic pulses reflecting from them, then there is a small change in phase as shown in (b). If the scatterers have moved a larger distance in the time interval, then the phase difference may 'wrap-around' and be indistinguisable from a smaller phase change (adapted from RDInstruments, 1996)

As mentioned above, the frequency of the ADCP affects the accuracy of the measurement. Higher frequency ADCPs (up to 1200 kHz with a range of 20 m) can measure more accurate water velocities than lower frequency ADCPs (down to 75 kHz with a range of ~1000m). For the applications discussed in this thesis, a 1200 kHz ADCP was used as the water depths were < 10m.

3.2 Mean Flow Estimates of water velocity

If beam 1 is oriented towards the x direction, the radial velocity along each beam (positive radial velocity is directed away from the instrument) is given by geometry (Lu *et al.*, 1999a)

Equation 3.1 $$b_1 = u_1 \sin\theta + w_1 \cos\theta$$

Equation 3.2 $$b_2 = -u_2 \sin\theta + w_2 \cos\theta$$

Equation 3.3 $$b_3 = v_3 \sin\theta + w_3 \cos\theta$$

Equation 3.4 $$b_4 = -v_4 \sin\theta + w_4 \cos\theta$$

Where b_i is the along beam velocity along beams i = 1-4. In this case, u_i , v_i and w_i are the flows towards the x, y and z directions respectively in beam i. θ is the angle of the beams from vertical (figure 3.4). By averaging over a suitable time period which is short enough to be able to assume stationarity of the turbulent parameters yet long enough to give statistically reliable estimates (10 minutes is used in this thesis) and assuming spatial homogeneity (i.e. the same flow characteristics in each of the four beams), the above equations can be rearranged to give

Equation 3.5 $$\overline{u} = \frac{\overline{b_1} - \overline{b_2}}{2\sin\theta}$$

Equation 3.6 $$\overline{v} = \frac{\overline{b_3} - \overline{b_4}}{2\sin\theta}$$

Equation 3.7 $$\overline{w} = \frac{\overline{\mathrm{b}_1} + \overline{\mathrm{b}_2} + \overline{\mathrm{b}_3} + \overline{\mathrm{b}_4}}{4\sin\theta}$$

Equation 3.8 $$\overline{e} \equiv -\frac{(\overline{b_1} + \overline{b_2}) - (\overline{b_3} + \overline{b_4}))}{2\sin\theta}$$

where e is an error velocity from the ADCP indicating the homogeneity of the water flow over the ADCP among other errors and the overbar denotes a time average.

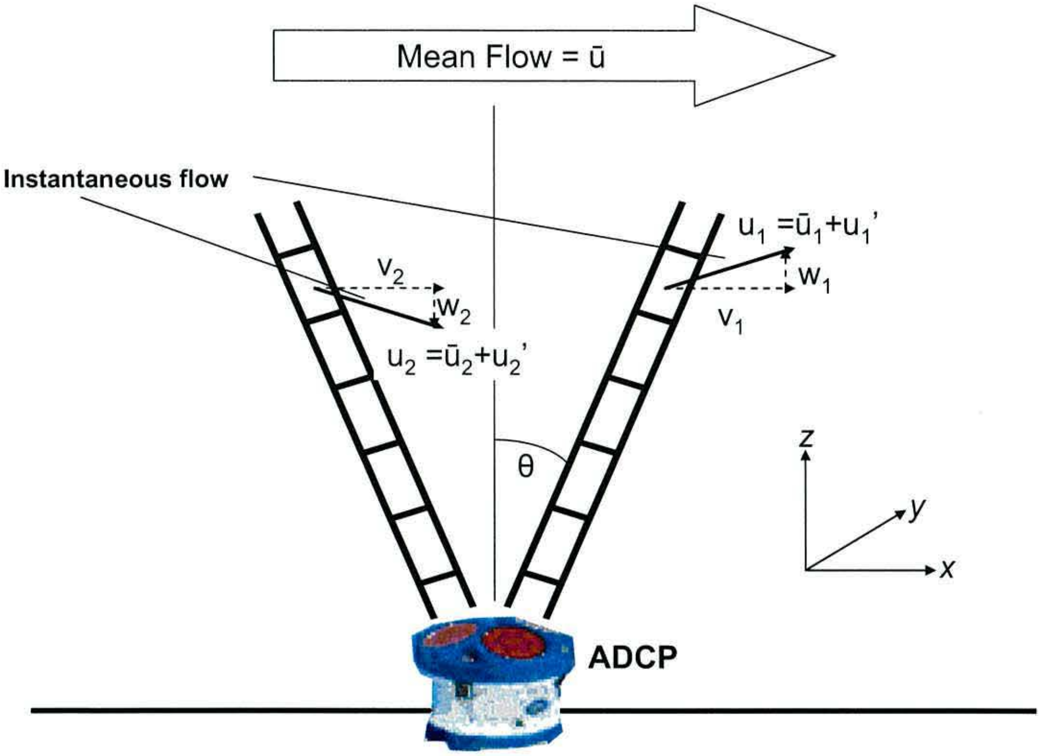

Figure 3.4. Velocities measured by a bed mounted ADCP. Each beam measures the radial component of the water velocity. u is the horizontal velocity, w is the vertical velocity and θ is the angle of the ADCP beam from vertical. The coordinate frame is shown: x (right) y (into the page), z (up).

3.3 Turbulence measurements - The Variance method

From the first experiments with acoustic Doppler devices, the potential to identify and measure turbulent events was recognised (Pinkel, 1979: Seitz, 1971). The break-through in measuring ocean turbulence using acoustic Doppler devices came, however, from the atmospheric community. Meteorologists have used atmospheric radar (the atmospheric equivalent of the Doppler sonar) to probe atmospheric turbulence for decades (Lhermitte, 1973). During the 1960's, a rotating atmospheric radar was used to estimate vertical momentum fluxes (Reynolds stresses) in the atmosphere (Lhermitte, 1968) using an approach similar to the variance method now used in oceanography (Lohrmann *et al.*, 1990).

The variance method uses along beam ADCP data from opposing beams to estimate Reynolds stresses. This can be combined with the shear estimates from the ADCP to infer turbulent kinetic energy (TKE) production rates and Fickian eddy viscosity values.

The method is detailed in other publications (Lu *et al.*, 1999b: Rippeth *et al.*, 2002: Stacey *et al.*, 1999a: Stacey *et al.*, 1999b) so only an overview is presented here.

3.3.1 Reynolds Shear Stress Estimates

By performing a 'Reynolds decomposition' (breaking the measured along beam velocities into a mean component, denoted by an overbar, and a fluctuating component, denoted by an apostrophe), turbulent parameters in the water column can be estimated.

The along beam velocities become;

Equation 3.9 $$b_1 = \overline{b_1} + b_1' \qquad b_2 = \overline{b_2} + b_2' \qquad b_3 = \overline{b_3} + b_3' \qquad b_4 = \overline{b_4} + b_4'$$

And similarly the east, north and vertical velocities become;

Equation 3.10 $$u = \overline{u} + u' \qquad v = \overline{v} + v' \qquad w = \overline{w} + w'$$

Equation 3.1 and equation 3.2 give

Equation 3.11 $$b_1' = u_1'\sin\theta + w_1'\cos\theta$$

Equation 3.12 $$b_2' = -u_2'\sin\theta + w_2'\cos\theta$$

Which can be squared and averaged to give

Equation 3.13 $$\overline{b_1'^2} = \overline{u_1'^2}\sin^2\theta + \overline{w_1'^2}\cos^2\theta + \overline{u_1'w_1'}\sin\theta\cos\theta$$

Equation 3.14 $$\overline{b_2'^2} = \overline{u_2'^2}\sin^2\theta + \overline{w_2'^2}\cos^2\theta - \overline{u_2'w_2'}\sin\theta\cos\theta$$

If the flow is laterally homogeneous over all four beams, then at a given depth bin in beams 1 and 2, $\overline{u'^2} = \overline{u_1'^2} = \overline{u_2'^2}$, $\overline{v'^2} = \overline{v_1'^2} = \overline{v_2'^2}$ and $\overline{u'w'} = \overline{u_1'w_1'} = \overline{u_2'w_2'}$. Equation 3.14 can then be subtracted from Equation 3.13 to give

Equation 3.15 $$-\frac{\tau_{xz}}{\rho} = \overline{u'w'} = \frac{\left(\overline{b_1'^2} - \overline{b_2'^2}\right)}{2\sin 2\theta}$$

Similar reasoning using equation 3.3 and equation 3.4 gives

Equation 3.16 $$-\frac{\tau_{yz}}{\rho}=\overline{v'w'}=\frac{\left(\overline{b_3'^2}-\overline{b_4'^2}\right)}{2\sin 2\theta}$$

where τ_{xz} is the Reynolds stress in the x direction and τ_{yz} is the Reynolds stress in the y direction. Therefore, the Reynolds stress in the water column above the ADCP can be estimated by the difference in the variance between opposing beams.

Figure 3.5 (taken from Kundu, 1990) provides physical reasoning for this. If Reynolds stresses are present in the water column (i.e. $\overline{u'v'}\neq 0$), and one of the ADCP beams is aligned with this correlation (e.g. upstream), then the opposing ADCP beam will be aligned across the direction of correlation. The upstream beam will therefore measure a higher along beam velocity variance than the downstream beam. This difference in variance will be proportional to the Reynolds stress ($\overline{u'v'}$) above the ADCP.

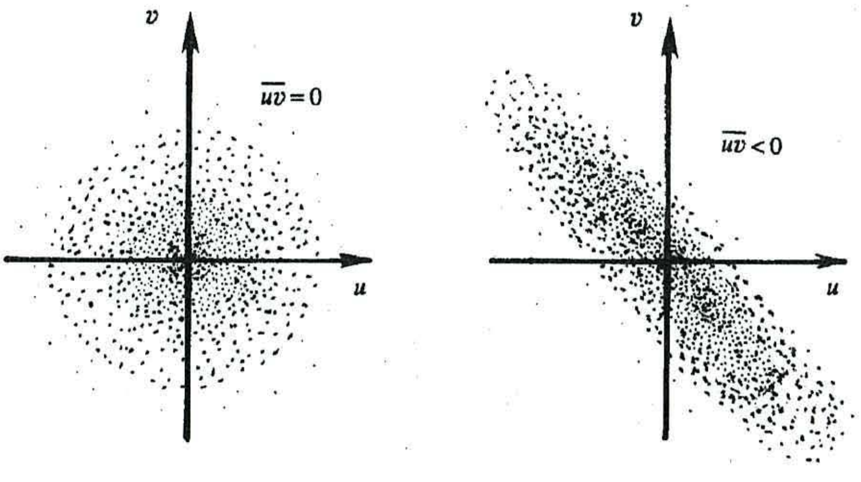

Isotropic

Anisotropic

Figure 3.5. Isotropic and anisotropic turbulence fields. Each dot represents a *uv*-pair at a certain time (Kundu, 1990). In an anisotropic case the along beam variance measured by an ADCP beam will be greater if the beam is aligned with the variation in *uv*.

The above analysis assumes that the ADCP is accurately levelled (to within 1° in both pitch and roll). If pitch and roll are present, then Equation 3.15 and Equation 3.16 are modified to

$$\overline{v'w'}=\frac{\left(\overline{b_3'^2}-\overline{b_4'^2}\right)}{2\sin 2\theta}-\varphi_2\left(\overline{v'^2-w'^2}\right)+\varphi_3\overline{v'w'}$$

where φ_2 is the pitch and φ_3 is the roll of the instrument (Howarth *et al.*, 2005).

If turbulent length scales are limited (e.g. by stratification or proximity to a boundary) such that the turbulent fluctuations contributing to $\overline{u'w'}$ are smaller than the ADCP bin size, this can lead to an underestimate in the Reynolds stresses. Such a decrease in the Reynolds stresses has been observed near the bed (Rippeth *et al.*, 2002), although no evidence exists in published literature indicating a decrease in Reynolds stress estimates due to decreased length scales in stratified conditions. However, the effect of limited length scales on measured Reynolds stresses has been seen in unpublished datasets (O'Donnell personal communication). It is also postulated that near the bed, form drag becomes an important retarding force so the Reynolds stresses decrease (Sanford *et al.*, 1999).

3.3.2 Calculation of bed shear stress from Reynolds stress profiles

Estimates of the bed shear stress can be made from midwater measurements of the Reynolds shear stresses using certain assumptions.

The mean momentum equation (derived from the Navier-Stokes equations, see Kundu, 1990, p 429) simplified into the along channel direction gives:

Equation 3.17 $$-\frac{Du}{Dt} = \frac{1}{\rho}\frac{\partial p}{\partial x} + \frac{\partial \tau_{xz}}{\partial z}$$

If stationarity can be assumed (which seems reasonable over the 10 minute averaging periods used here), equation 3.17 reduces to $\frac{\partial \tau_{xz}}{\partial z} = -\frac{1}{\rho}\frac{\partial p}{\partial x}$. The assumption that the horizontal pressure gradient ($\frac{\partial p}{\partial x}$) is constant over depth (which is a reasonable assumption in a fully mixed water column) leads to:

$$\frac{\partial \tau_{xz}}{\partial z} = \text{constant}$$

Using the boundary condition that the Reynolds stress is zero at the surface, the Reynolds stress can be expressed as a function of bed stress (τ_b), height above bed (z, where $z = 0$ at the bed) and absolute water depth (h).

Equation 3.18 $\tau = \tau_b\left(1-\frac{z}{h}\right)$

The bed shear stress can hence be calculated by linearly interpolating midwater stresses to the sea bed.

The bed shear stress can also be expressed as a friction velocity, u_* . The friction velocity is related to the bed stress by

Equation 3.19 $\tau_b = \rho u_*^2$

Estimates of the bed shear stress can be combined with a reference velocity to give a drag coefficient estimate by, for example:

Equation 3.20 $\tau_b = \rho C_{200}\overline{u(200)}^2$

(see Kundu, 1990) where $u(200)$ is the velocity at 2m above the bed and C_{200} is the associated drag coefficient. The choice of 2m above the bed is an arbitrary reference height which will be used throughout this thesis. 2 metres was taken because both ADCPs measured velocities and stresses at this height.

3.4 Law of the Wall

A log profile (see section 2.8) is fitted to the 10 minute averaged data from the ADCP. Using the criteria that the log layer extends to $0.03-0.04u_*\omega^{-1}$ and using a u_* of 0.05 m s^{-1} [†] and ω^{-1}=12.42/2π hours indicates that the log layer should extend to a depth of ~ 12m, i.e. the log layer should encompass the entire water column during peak flow. In this analysis, the log layer is fitted up until a height where the variance explained by the log fit drops below 99%.

The vertical averaging due to the range gating from the ADCP influences the velocity readings in the high shear region close to the bed. An analysis presented in appendix 10.2 shows that this is not a significant factor in the results presented here.

The log profile of velocity (equation 2.16) can be combined with the quadratic drag law (equation 3.20) and the definition of the friction velocity (equation 3.19) to give an independent estimate of the drag coefficient from that estimated in section 3.3.2:

[†] A u_* of 0.05 m s^{-1} corresponds to a mean flow velocity of ~ 1 m s^{-1} and a bed drag coefficient of ~ 0.0025.

Equation 3.21 $$C_{200} = \left(\frac{u_*}{\overline{u}(200)} \right)^2 = \left(\frac{\kappa}{\ln(2/z_0)} \right)^2$$

3.4.1 Turbulent Kinetic Energy Production Rate

By multiplying the Reynolds shear stress by the mean shear, the input to turbulent kinetic energy due to the shear flow can be estimated (Kundu, 1990);

Equation 3.22 $$P = -\rho \left(\overline{u'w'} \frac{\partial \overline{u}}{\partial z} + \overline{v'w'} \frac{\partial \overline{v}}{\partial z} \right)$$

The vertical derivative of equation 3.5 and equation 3.6 gives the mean shear components of flow ($\frac{\partial \overline{u}}{\partial z}$ and $\frac{\partial \overline{v}}{\partial z}$) over the ADCP. Therefore an ADCP can estimate TKE production with no further information.

3.4.2 Vertical Eddy Viscosity Estimation

Dividing the Reynolds stress by the shear, the eddy viscosity N_z can be estimated (Williams *et al.*, 2004):

Equation 2.9 $$N_z = \frac{\overline{u'w'}}{\partial \overline{u} / \partial z}$$

This is the diffusion parameter representing the vertical flux of horizontal momentum. Estimates of N_z provide an indication of the accuracy of the variance method, as shown in figure 8.11 and figure 8.12.

3.5 Limitations of the variance method.

The variance method has been widely adopted by a number of researchers, and comparison of the results with independent measurements have proven it's reliability (Howarth, 2002: Rippeth *et al.*, 2003). However a major limitation of the method is the requirement for the ADCP to be accurately levelled. If the ADCP is not accurately levelled, then the Reynolds stress estimates may be biased by up to 6% for 1° of tilt and 17% for 2° of tilt.

The method for levelling the ADCP involved divers examining two orthogonal spirit levels mounted on the heads of the ADCPs.

3.6 *Acoustic Doppler Velocimeter*

The Acoustic Doppler Velocimeter (ADV) also uses the Doppler effect. It sends out a pulse of sound (at 6 MHz) from a single acoustic transmitter (figure 3.6), then listens to the echo from a small volume of water (diameter 0.015m, length 0.020m) with 3 recievers. The 3 components of velocity in the can then be determined in the measuring volume. The ADV can take measurements at 64 Hz.

Direct estimates of the Reynolds stresses (section 2.2) and TKE levels (section 2.3) in the measuring volume can then be made.

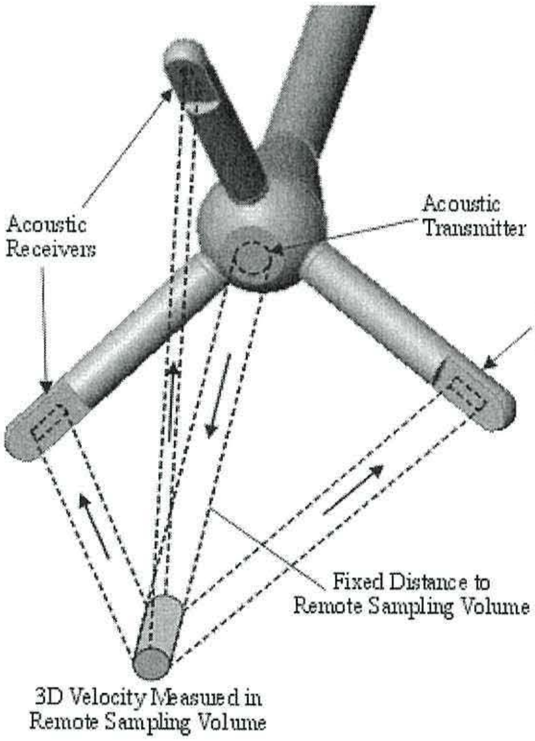

Figure 3.6. Schematic of ADV. The ADV sends a short pulse at 6 MHz from the acoustic transmitter. The 3 acoustic receivers detect the doppler shift of the scattered sound from the sampling volume and hence determine the 3D velocity in the sampling volume. From http://www.sontek.com/.

4 Dissipation via the Structure Function

Analogy with meteorological Doppler radar indicates more information about turbulence can be obtained from the ADCP data. An approach for estimating the rate of dissipation of TKE using a structure function approach has been developed. An outline is given below and a more rigorous mathematical approach is presented in appendix 10.1.

4.1 Theory

A second order structure function *D(z,r)* can be defined at a location *z* using the along beam velocity, *v'* (with the temporal mean and hence shear removed) such that,

Equation 4.1 $$D(z,r)=\overline{(v'(z)-v'(z+r))^2}$$

D(*z*,*r*) is the mean-square of the velocity fluctuation difference between two points separated by a distance *r*. The second order refers to the square of the velocity difference. The velocity difference between two points separated by r is largely due to eddies with a length scale comparable to *r* and an associated velocity scale of *s'* (which is thus a function of *r* and *z*) . i.e.

Equation 4.2 $$D(z,r)\sim s'^2$$

(where the ~ denotes proportionality). If an eddy is characterised by a velocity scale *s'* and a length scale *r* , the kinetic energy contained by the eddy is proportional to s'^2. If the eddy loses most of it's energy within a certain number of overturns, then this time scale will be proportional to *r*/*s'*. Therefore the rate of transfer of energy through the scale of the eddies and eventually on to viscous dissipation is given by (Taylor, 1935)

Equation 4.3 $$\varepsilon=\frac{s'^2}{r/s'}=\frac{s'^3}{r}$$

Therefore, the structure function can be related to the dissipation rate via:

$$\varepsilon=\frac{D(z,r)^{3/2}}{C_v^{\,3}}\frac{1}{r}$$

leading to:

Equation 4.4 $$D(z,r)=C_v^{\,2}\varepsilon^{2/3}r^{2/3}$$

where C_v^2 is a constant, which in atmospheric studies has been found to be between 2.0 and 2.2 (Sauvageot, 1992). No current literature exists indicating a different value of C_v^2 that should be used in the marine environment, hence 2.1 is used in this thesis. The results given show that this is a reasonable value to use.

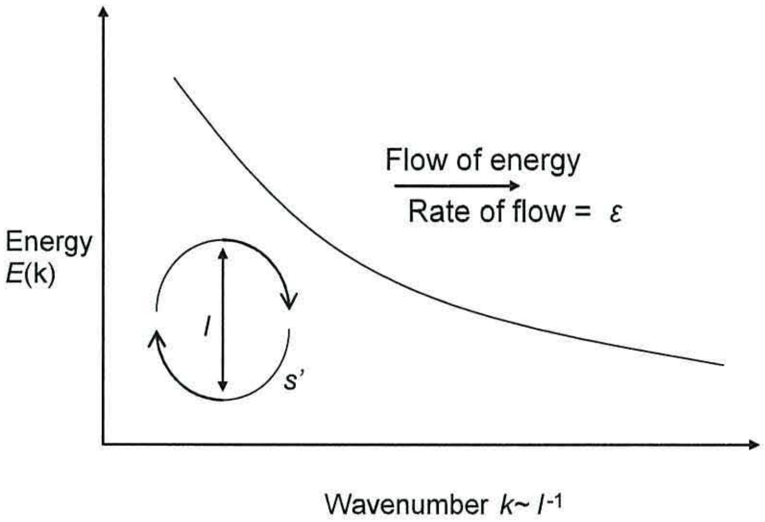

Figure 4.1. The energy contained at different scales of eddies, r. The energy 'cascades' from larger to smaller scales (left to right). The characteristic velocity scale of each eddy is s'.

Equation 4.4 will hold for values of r within the inertial sub-range, i.e. $l_K << r << l_O$ (Frisch, 1995).

4.2 Application

For each acoustic beam the along beam component of the water velocity is estimated from the Doppler shift in the return signal for a series of heights above the transducer. The water column is divided into depth bins and the along beam velocity is calculated for each bin from a 1 or 2 second ensemble average (depending on the dataset). The time series for each bin is then averaged over a period long enough to give statistical reliability but short enough that the time series can be assumed stationary. For the instrument setup and semidiurnal tidal conditions at the locations of interest, a 10 minute averaging period is selected. The temporal mean is then subtracted for each bin, leaving the turbulent velocity fluctuations, v'.

A 'centered difference' technique is then used to obtain the turbulent velocity difference for each height bin of each acoustic beam (see table 4-1). The turbulent velocity differences are squared and then averaged over 10 minutes to obtain $D(z,r)$ (from equation 4.1).

Differences between adjacent bins are not used as the velocities are not totally independent because of the weighted average used in the RDI ADCP signal processing software (RDInstruments, 1996). There are fundamental limitations on r: at the small scale, the limit is set by the Kolmogorov microscale (e.g. for a low limit of dissipation of 10^{-6} W m^{-3}, the Kolmogorov dissipation scale is ≈ 5×10^{-3} m, i.e. more than an order of magnitude smaller than the smallest possible bin size using current coherent Doppler technology). At the large scale the limitation is the Ozmidov scale (in a stratified environment) and the minimum distance to the boundary (in a homogeneous environment). The value of $r^{2/3}$ fitted to the data is limited to a length comparable to the largest eddies in the inertial subrange.

Separation (bins)	General Algorithm	Example (i=6).
2	$v(i+1)-v(i-1)$	$v(7)-v(5)$
3	$v(i+2)-v(i-1)$, $v(i+1)-v(i-2)$	$[\{v(8)-v(5)\}+\{v(7)-v(4)\}]/2$
4	$v(i+2)-v(i-2)$	$v(8)-v(4)$
5	$v(i+3)-v(i-2)$, $v(i+2)-v(i-3)$	$[\{v(9)-v(4)\}+\{v(8)-v(3)\}]/2$

Table 4-1 Centred Difference scheme used to calculate the value of the velocity difference in equation 4.1 . Column 1 is the number of bins used for the separation r, column 2 is the general algorithm used to calculate $v(z)$- $v(z+r)$ when z is centred about the i^{th} bin and column 3 is an example of the bins used in the algorithm when the height z is equivalent to the 6th bin (i=6). Note for odd values of r there are two estimates of the velocity difference. An average value of the two estimates is used in these odd cases.

To examine the sensitivity of the technique to the maximum value of r, the data was tested with a number of maximum values for r, ranging from 4 to 12 m (in the vertical). The results of this sensitivity analysis show a small increase in estimates of ε with increased r by ~ 10% per metre for the up and downstream beams, and by ~ 4% for the beams oriented transverse to the mean flow. In a stratified environment, estimates of ε would be expected to decrease as r approaches the Ozmidov scale. However in a well mixed environment such as those studied here, the greater vertical averaging increases the estimates of ε.

The mean squared velocity difference $D(z,r)$ is then fitted to an equation of the form,

Equation 4.5 $$D(z,r) = N + Ar^{2/3}$$

(see figure 4.2) in order to find a value for A. N is an offset which represents an uncertainty due largely to instrument Doppler noise and other errors in the ADCP velocity estimates (or due to non-turbulent velocity fluctuations, e.g. waves). Assuming that the uncertainties in the along beam velocities can be accounted for by a variance, σ_N^2, which is independent of height, then the noise will be independent of the range r and the offset will be $N = 2\sigma_N^2$. The uncertainty in the ADCP estimates will be dependent on the system frequency, number of pings, bin size and other system variables.

Defining the coefficient A as;

Equation 4.6 $$A = C_v^2 \varepsilon^{2/3}$$

(where $C_v^2 = 2.1$, a value used in radar meteorology Sauvageot, 1992) ε is readily obtained, thus providing estimates of ε and the uncertainty in the along beam velocity estimate ($N = 2\sigma_N^2$).

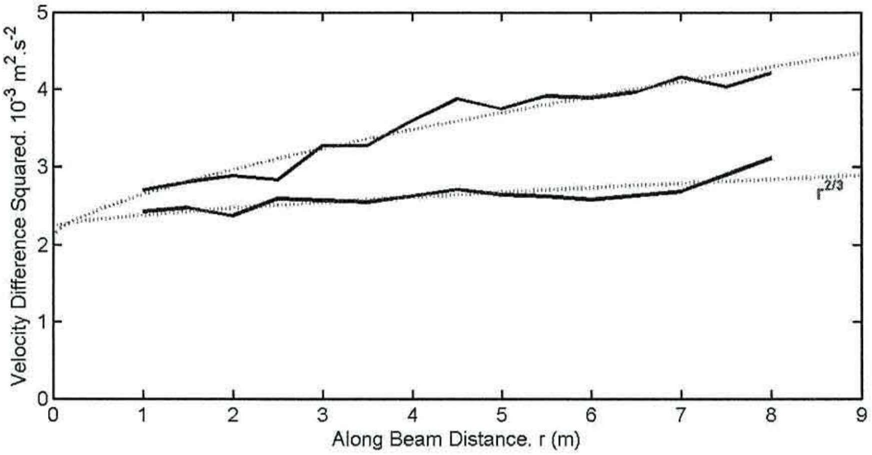

Figure 4.2. The $r^{2/3}$ fit on 2 sets of along beam ADCP data. The dotted lines are the polynomial from equation 4.5, fitted to along beam velocity data from 2 different 2s ensemble (black line). The upper line has a greater slope than the lower line and hence provides a greater dissipation estimate. The *y* intercepts of the polynomials are the estimates of the inherent Doppler noise (*N* in equation 4.5).

4.3 Testing and Validation of Structure Function

Dissipation estimates made using this new structure function method have been compared with dissipation estimates made using a microstructure profiler. Microstructure profilers have been used since the 1970s to estimate turbulence dissipation rates in the marine environment. Details of the microstructure profiler operation and data processing have been widely published (Dewey *et al.*, 1987: Gargett, 1978: Osborn, 1980: Peters *et al.*, 2001: Rippeth *et al.*, 2003). The ability of microstructure profilers to measure turbulence dissipation rates at the viscous dissipation scale ensures that they are the benchmark measure of turbulence.

Two datasets are presented in this section. The first, which is from Red Wharf Bay, is used to compare structure function and microstructure dissipation measurements. An upstream/downstream asymmetry was identified in the Red Wharf Bay dataset so a second dataset from the Menai Strait is also presented in an attempt to shed light on the source of this asymmetry.

4.3.1 Red Wharf Bay – Comparison with microstructure profiler

The first data set was collected from Red Wharf Bay during a University of Wales, Bangor, cruise led by Tom Rippeth, close to the north coast of Anglesey at a site (53°22.8'N, 4°12.5'W), where the water depth ranged from 19 m at low water to 25 m at high water, and there is a rectilinear tidal flow and maximum currents of order 1 m s^{-1}. The water column was homogeneous throughout most of the observational period except for some weak stratification in the upper part of the water column around low water. The location was selected as having a flat bottom and being far

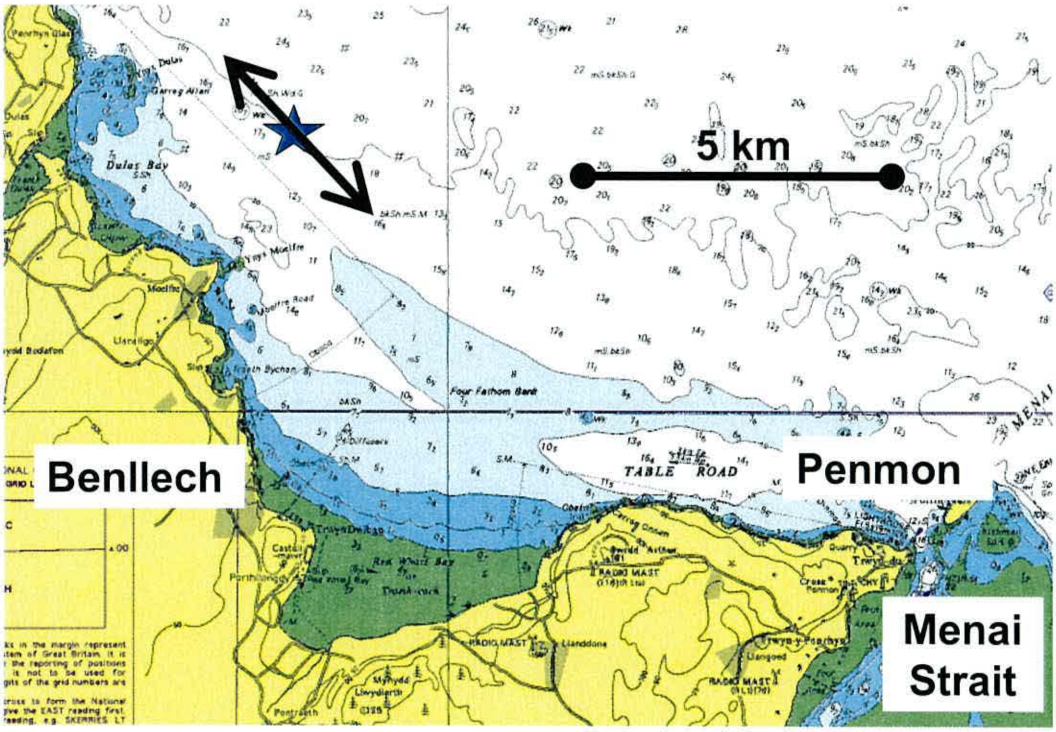

Figure 4.3. Location of the Red Wharf Bay ADCP (blue star). The black arrow shows the direction of tidal flow.

from any major topographic features so that, to a first order, a local equilibrium between the rates of production and dissipation of TKE can be assumed (i.e. $\varepsilon \approx P$).

A self contained 1200 kHz RDI workhorse ADCP deployed on a rigid bed frame was set up with a 1 m vertical bin size and 'pinged' at a rate of 2Hz. The data were ensemble averaged over 2 seconds (i.e. 4 pings). Beam 3 of the ADCP was orientated to the northeast and aligned parallel to both the local coastline and the main component of tidal flow. The ADCP pitch angle (beams 3 and 4) measured by the internal pitch and roll sensors was initially 3.5° but settling to ~ 1° for the second tidal cycle of the deployment. The instrument roll (beams 1 and 2) was within 1° throughout. A Fast-Light-Yoyo (FLY) microstructure profiler was operated from the RV Prince Madog for a period of 24 hours. The loosely tethered FLY profiler falls through the water column at a speed of 0.7-0.8 m s^{-1} while measuring shear data on a scale of ~ 0.6 cm from which ε is estimated. During each hour of the observations 10-12 FLY profiles were made (full experimental details are given in Rippeth *et al.*, 2003).

For this first deployment, the separation r was limited to an along beam distance of 5.3m, which corresponds to a vertical distance of 5 m. This limiting scale was shortened near the boundaries so that the distance between differenced bins was always less than the distance from the centre bin to the boundary. These limiting scales are within the fundamental limitations on r as stratification was weak. An averaging period of 10 minutes is used.

Estimates of P and ε from the ADCP along beam velocity data and ε from velocity microstructure are shown in figure 4.4. The flow is predominantly a result of a rectilinear semidiurnal tide which consists of a short, strong flood phase, with velocities up to 0.85 m s^{-1}, and a longer slower ebb phase, with maximum velocities of 0.65 m s^{-1}.

The TKE production rate (P) varied with a quarter diurnal frequency. Maximum P which coincided with the strongest flow near the bed, however a delay in maximum P is evident higher in the water column. Production was highest near the bed where the Reynolds stress and shear is largest. No P estimates are available below 4 metres above bed (mab) due to the height of the bed mounting frame and the ADCP blanking interval. Maximum values for production rate of $5\text{x}10^{-2}$ W m^{-3} are estimated during peak flood tide, while on the ebb tide the maximum value was $1\text{x}10^{-2}$ W m^{-3}.

The values of P decrease by an order of magnitude over the first 10 m above the bed. The threshold for the TKE production estimates due to noise is estimated to be of the order 5×10^{-4}W m^{-3} (Rippeth *et al.*, 2003) and so P estimates are not reliable in the upper part of the water column around slack water.

The velocity microstructure measurements indicate that the dissipation rate follows a similar quarter diurnal pattern with stronger dissipation on the flood phase of the tide than the ebb. The FLY profiler makes reliable measurements across much of the water column (from ~ 5 m below the surface to 0.15 m above the bed) and so sampling the higher dissipations close to the bed. The maximum value of dissipation observed in this region is about 10^{-1} W m^{-3}. The noise threshold of the FLY profiler is estimated to be ~ 10^{-6} W m^{-3}.

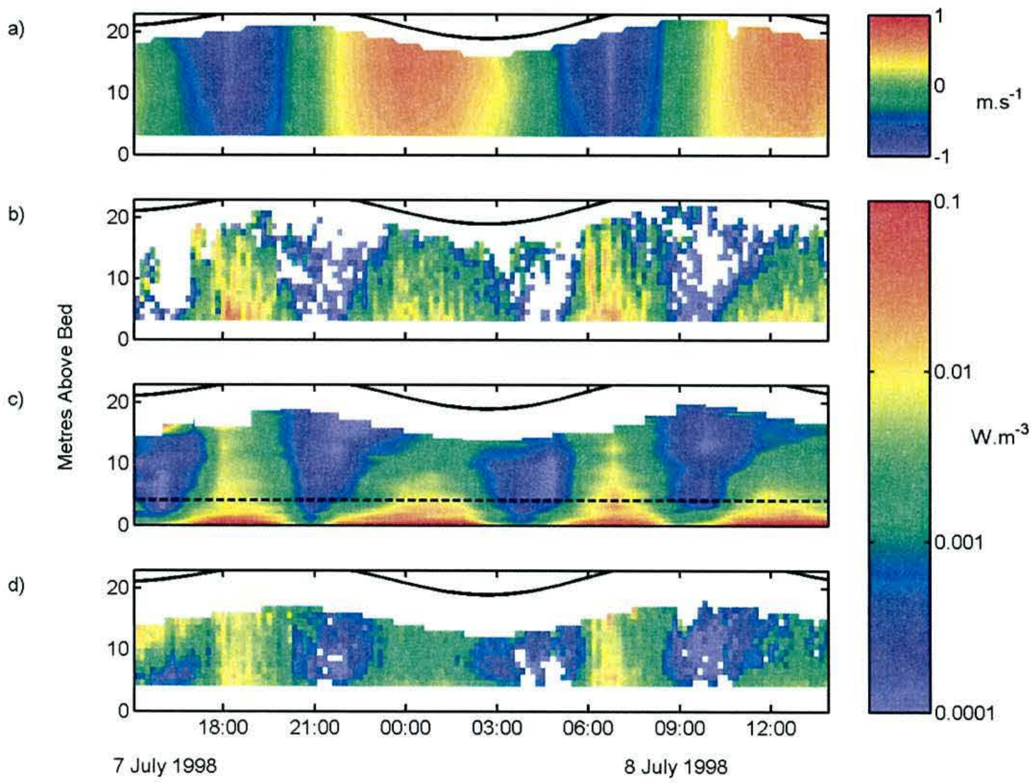

Figure 4.4. Red Wharf Bay data: a) shows the along stream component of velocity (+ve towards 321°T), b) is the TKE shear production, c) is the TKE dissipation measured by the FLY profiler and d) is the TKE dissipation from the structure function method. The white gaps in b) and c) are when the data becomes unreliable from the ADCP turbulence estimates. The dashed line in c) indicates where the structure function starts measuring.

A logarithmically averaged value of ε using the structure function method for all 4 beams is shown in figure 4.4d. The time evolution of ε from the structure function (figure 4.2b) shows fair agreement with the velocity microstructure estimates of ε and the ADCP production rate estimates (figure 4.2c,d). In particular, the microstructure and structure function ε profiles track each other reasonably well and exhibit a similar range of dissipation values (10^{-4} W m^{-3} < ε < 10^{-1} W m^{-3}).

4.3.2 Upstream – downstream asymmetry

A comparison of ε for the different acoustic beams (figure 4.5) shows that the upstream facing beam consistently gives a higher estimate of the TKE ε than the downstream beam (by up to a factor of 3). For example, during the flood tides (6th July 1700-2100 and 7th July 0500-0900), beam 3 is pointing upstream and beam 4 is directed downstream with $\varepsilon_3 > 3\ \varepsilon_4$. The ε estimates made from beams 1 and 2 (the beams which are orientated perpendicular to the flow) lie between those estimated using beams 3 and 4.

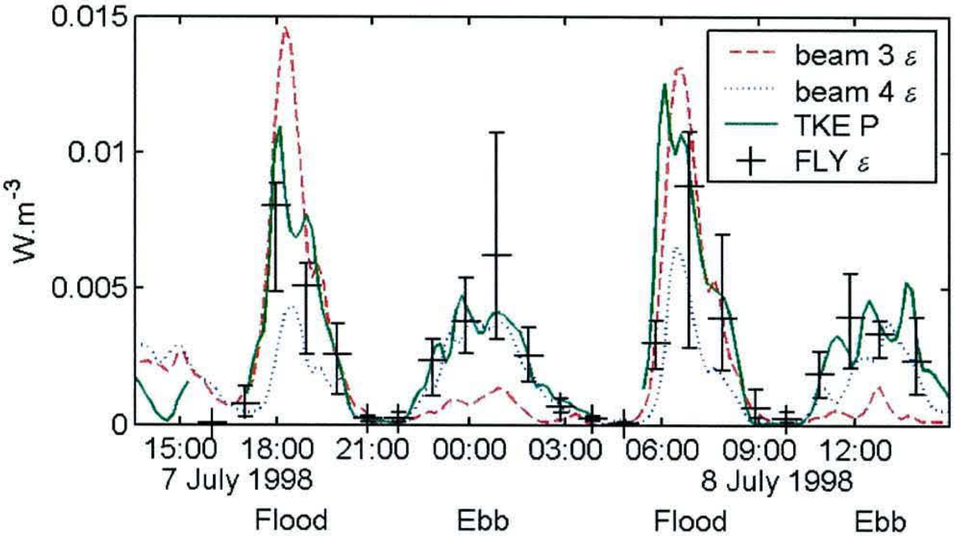

Figure 4.5. Red Wharf Bay data: Comparison of TKE production rates from the variance method, TKE dissipation rates from the FLY profiler (including 95% Confidence interval limits) and TKE dissipation rates from the structure function method applied to the upstream and downstream beams. All measurements are taken at 7.5 metres above the bed. The flood and ebb phases of the tide are shown below the *x* axis.

Direct comparisons of the structure function estimates of ε_{SF} to microstructure estimates of ε_{FLY} and TKE P estimates are given in figure 4.6. The comparison of TKE P from the variance method and FLY dissipation showed that the 2 are consitent over all water depths. The structure function gave lower estimates of ε than production and FLY dissipation estimates in the lower water column and higher estimates in the upper water column. The larger bin sizes of the structure function do smooth the vertical profile, which would decrease the structure function estimates near the bed and increase them near the surface.

Comparisons of the structure function and microstructure estimates of ε are given in table 4-2. During the first tidal cycle there is a significant difference in the ratio between the two phases of the tide. A similar result was obtained for the ε_{FLY} / P ratio using the same data (Rippeth et al., 2003) and is explained by the presence of surface gravity waves (Howarth, 1999), particularly when the wind blows against the ebbing tide. The orbital motions of the waves produce a bias in the stress estimates. A full evaluation of the effect of surface gravity waves on the structure function technique awaits further analysis. For the second tidal cycle, by which time the wind had died away and the waves diminished, the ratio is $\varepsilon_{SF} / \varepsilon_{FLY} = 0.68 \pm 0.23$, with no significant difference between the flood and ebb phases of the tide.

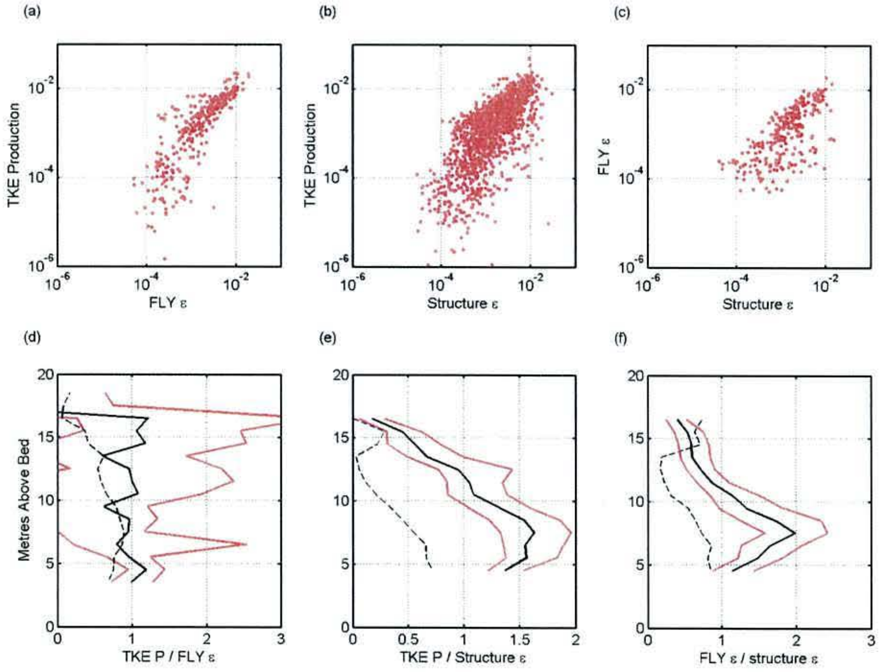

Figure 4.6. Comparison of TKE Production rates from the variance method, TKE dissipation rates from the FLY and TKE dissipation rates from the structure function method (an average of all 4 beams). (a), (b) and (c) show depth and time matched values plotted against each other. (d),

(e) and (f) show the depth mean ratios. The red lines show the 95% confidence intervals calculated using a bootstrap resampling method. The dotted line is an estimate of an R^2 correlation value.

Data Subset	Structure ε / FLY ε	Lower 95% CI	Upper 95% CI
All data	0.88	0.69	1.17
Tidal Cycle 1	1.09	0.83	1.57
Tidal Cycle 2	0.68	0.51	0.97
Flood 1	0.76	0.62	0.97
Flood 2	0.52	0.40	0.73
Ebb 1	1.55	1.06	2.89
Ebb2	0.86	0.60	1.48

Table 4-2. The ratio of structure function dissipation to FLY dissipation for the main dataset and for subsamples. The 95% confidence intervals were calculated using a bootstrap resampling technique.

4.3.3 Effect of averaging period

Variation in the averaging time period did not significantly change the mean dissipation estimates (figure 4.7). Shorter averaging periods introduce more variability into the ε estimates. Whether the increased variability is due to turbulent events or increased noise is not clear.

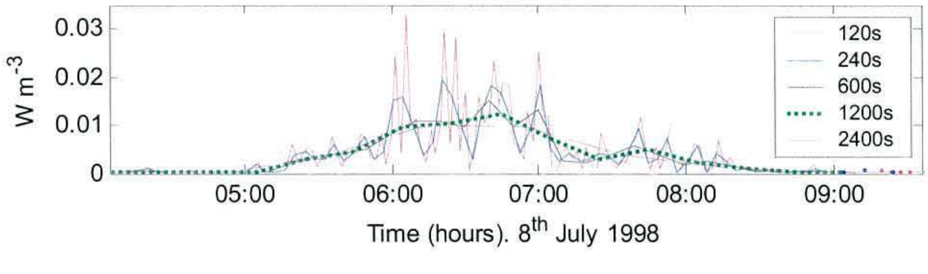

Figure 4.7. The effect of different averaging periods on the dissipation estimates.

4.3.4 Doppler noise measurement

The mean values of the Doppler noise estimated using (3.8) and averaged over the entire deployment are shown in figure 4.8. The average value of the inherent Doppler noise is ~ 30% larger than the value given by RDI's PlanADCP software.

This ratio of measured to predicted Doppler noise is consistent with previous studies (Williams and Simpson, 2004).

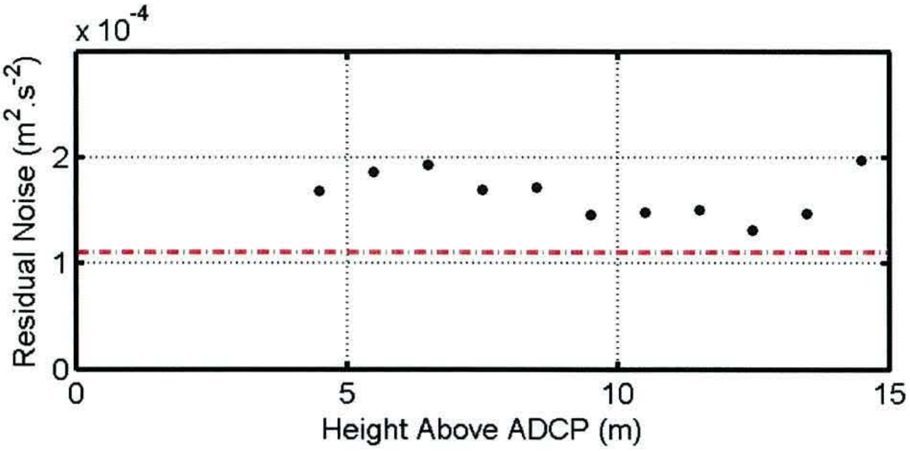

Figure 4.8. Noise estimates for the ADCP. The black dots are the estimates of the inherent Doppler noise of the ADCP velocity estimates calculated from equation 4.5. The dashed line is twice the along beam Doppler variance for this deployment predicted by RDI's PlanADCP software.

4.3.5 The Menai Strait Observations

The mismatch between the upstream and downstream beams is likely to be due to anisotropic effects in shear and Reynolds stress. In order to investigate the effect of shear and Reynolds stress a second experiment was undertaken in an energetic tidal channel, the Menai Strait (Rippeth et al., 2002), where the horizontal advection of turbulence is thought to be an important term in the local TKE balance. The flow in the Menai Strait is again dominated by a strong and rectilinear semidiurnal tidal flow.

A 600 kHz ADCP was deployed 150m from the shore near the School of Ocean Sciences in Menai Bridge in a region where the depth ranged from 4 to 10 metres. The cable allowed the ADCP to be re-configured without having to re-deploy the instrument.

During flood tides (when the flow is to the North West), the main flow of water between the menai suspension bridge and the ADCP mooring site hugs the south bank, probably due to centripetal effects as the flow passes under the bridge (figure 4.9a). The ADCP is thus located on the edge of a tidal eddy during flood tides (Hyder *et al.*, 1995). The cross-channel component of the tidal eddy carries

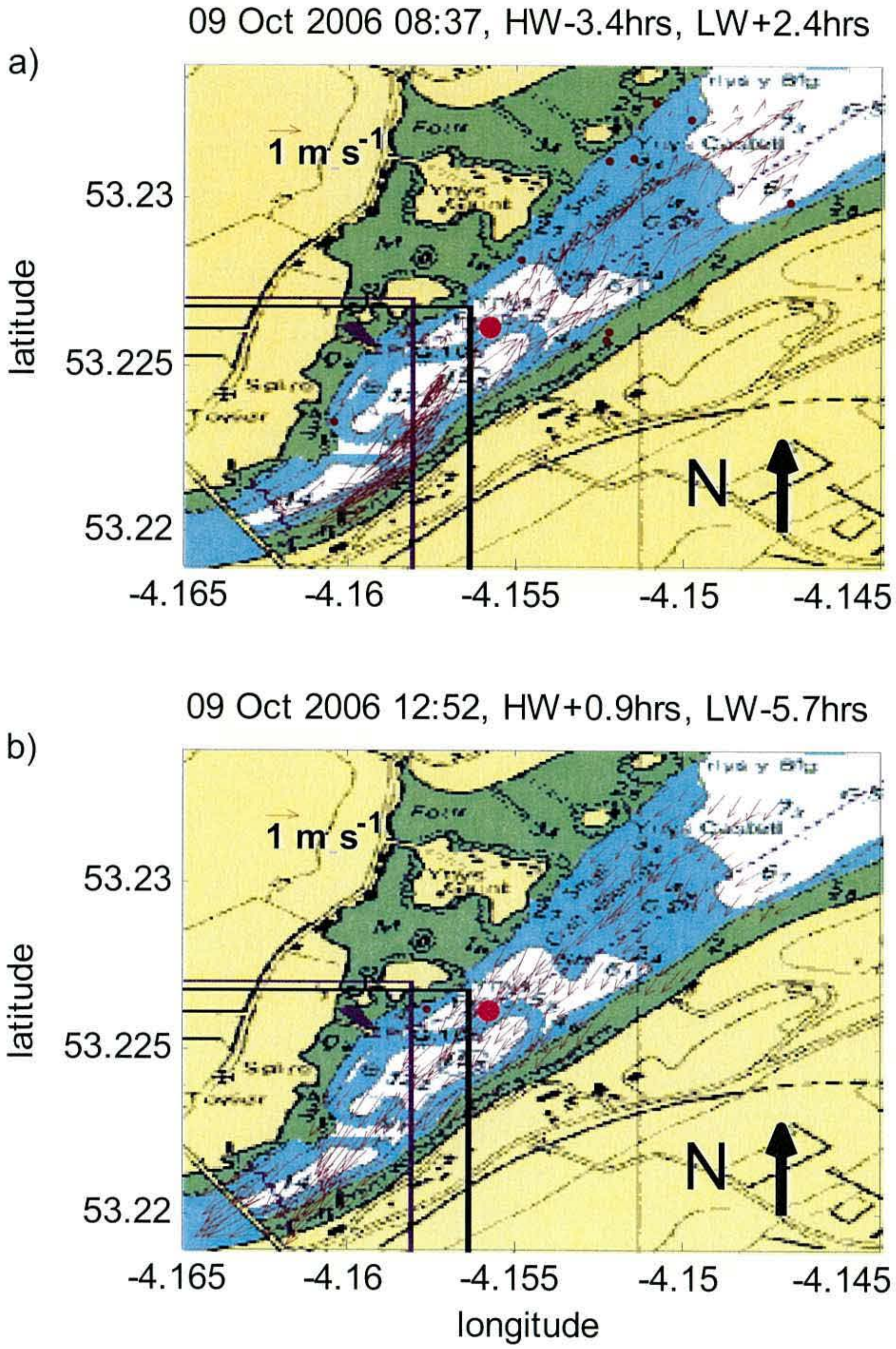

Figure 4.9. ADCP location in the Menai Strait (the red dot denotes the mooring position). The brown arrows indicate the water speed and direction measured during a roving ADCP survey conducted on October 9th (spring tides) during (a) the flood tide and (b) the ebb tide. Beam 1 is orientated towards the north east and beam 2 is orientated to the south west. The Menai suspension bridge is the road crossing the water in the south west corner.

turbulence generated in the main flow over the ADCP. Therefore the ADCP is in a location where local generation of turbulence is relatively low, however turbulence which is generated in the main flow in the channel and advected to this region is being dissipated. This allows relatively high dissipation rates to be observed in a location where the mean flow is relatively low.During ebb tides, the main flow of water is directly over the ADCP (figure 4.9b) and turbulence is being generated and dissipated locally. There is also a strong and consistent direction of flow over the ADCP.

The ADCP was setup to collect data in mode 12 (rapid pinging mode), with 12 'subpings' averaged over each second to produce a single velocity estimate. The vertical bin size was set to be 0.5 m and the along beam velocity data recorded. On the ebb tide strong flows (> 1 m s^{-1}), Reynolds stresses (> 2 N m^{-2}) and mid water dissipation rates (> 2×10^{-1} W m^{-3}) were estimated for the water column above the ADCP. During the flood tide the ADCP measured much lower currents (maximum ~ 0.2 m s^{-1}), although strong Reynolds stresses (~ 1.5 N m^{-2}) and dissipation rates (~ 0.1 W m^{-3}) were observed. It is assumed that the occurrence of high stresses and dissipation rates in the absence of a strong mean flow on the flood tide is due to advection by a weak secondary cross channel flow, bringing turbulence from the main channel into the region of the strait where the ADCP was located.

On the ebb tide, there is a linear relation between the square of the velocities and the Reynolds stress. However, on the flood tide strong stresses were observed during periods of low flow (figure 4.10), i.e. the velocities and stresses are no longer correlated. The difference in dissipation rates between the up and downstream beams correlate with the Reynolds stress and the shear – i.e. the difference in dissipation rates increased with both increasing Reynolds stresses and shear. However, large differences in the dissipation rates were observed at low velocities during the flood, and the correlation is not symmetric about zero. The difference between up and downstream beams is proportional to the Reynolds stress both when the flow is strong and when the flow is weak. Therefore, figure 4.10b and c are symmetric, however figure 4.10d is not.

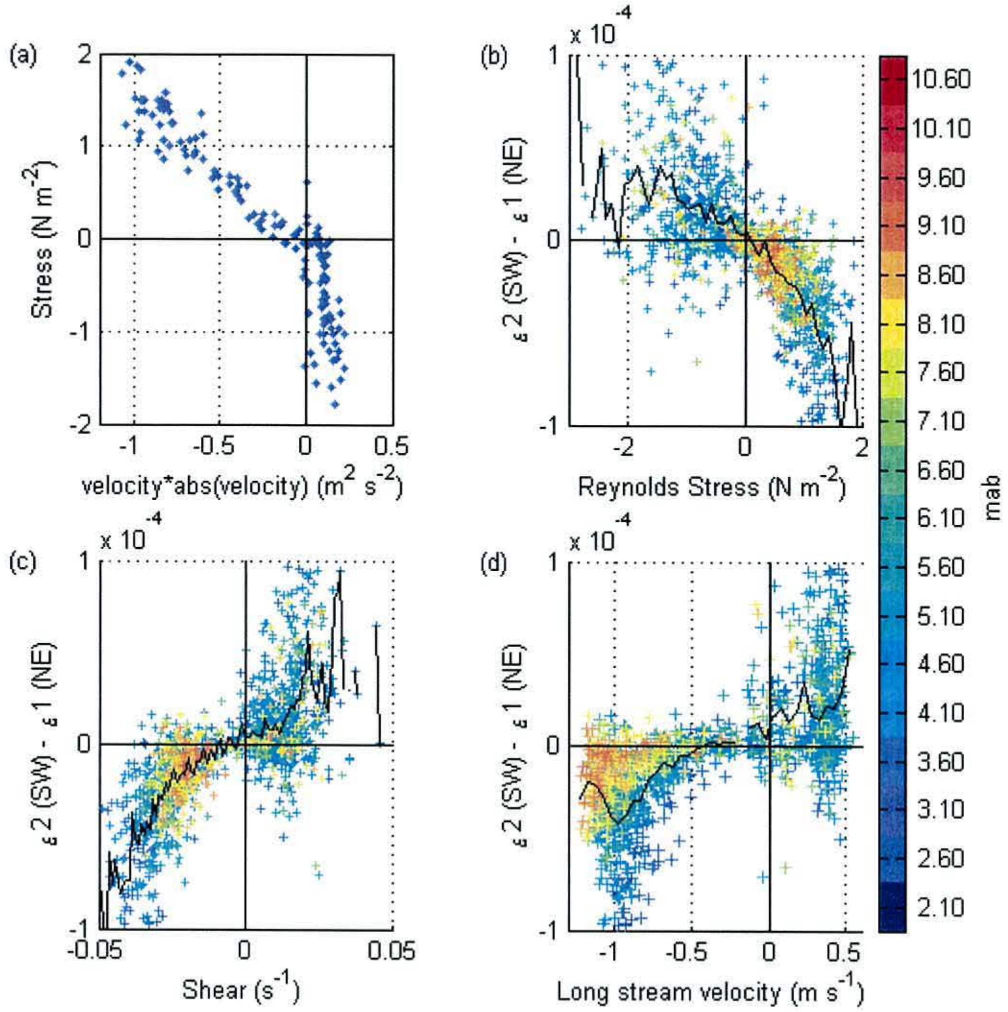

Figure 4.10. (a) stress vs velocity^2 at 3.1 mab (flood direction, which is positive flow is towards north east). (b) the difference in dissipation between beams 1 and 2 vs Reynolds stress, (c) the difference in dissipation between beams 1 and 2 vs along stream shear and (d) the difference in dissipation between beams 1 and 2 vs along stream velocity. The colours in (b), (c) and (d) are the height above the bed at which the dissipation rates, Reynolds stresses and velocities were measured. The black lines in (a), (b) and (c) are averages (binned by the x-axis) of the data.

4.4 Summary

The basic theory and a technique for measuring the turbulent dissipation rate in the ocean using standard off-the-shelf ADCPs has been presented. TKE dissipation rates made using this method compare well with simultaneously collected FLY microstucture profiler dissipation rates (ratio ~ 0.68) and TKE production rates estimated using the same ADCP data by applying the variance method (ratio ~ 0.47).

The advantage of this technique is that it can be used to provide relatively long term, continuous time series of ε-profiles with power and memory capacity of the ADCP the only limiting factors. There are restrictions on the applicability of the technique in stratified environments where the maximum value of r is restricted to the Ozmidov scale (typically up to 5 m in a weakly stratified tidal channel – Stansfield (2001) - and of the order <0.1 m to 0.4 m in the thermocline of seasonally stratified shelf seas - Rippeth *et al.*, 2005). However, if an accurate estimate of the noise N can be made, the dissipation can be calculated over a much reduced scale of twice the bin size; i.e. from equation 4.5 and equation 4.6;

Equation 4.7 $$\varepsilon = \frac{\left(D(z,r) - N\right)^{\frac{3}{2}}}{C_v^{\,3} r}$$

As it is possible to extract the rms Doppler noise, N, which varies only slightly with height above the bed, this modification may, in future, allow the estimation of ε using the structure function technique on scales appropriate to the stratified marine environment.

The observation that the upstream facing ADCP beam constently gives a larger value of ε indicates that the assumption of isotropy required for Taylor's cascade theory is not strictly ture. Other than this isotropic effect there is no requirement for the ADCP to be oriented vertically, as is the case with the variance technique and so it should be possible to deploy an ADCP on a range of platforms, e.g. non-gimbaled bed frames, mid-water buoys or possibly moving vessels, in order to make estimates of ε.

5 Description of sites

As the goal of the MaBenE project was to build a 3D numerical model with the ability to simulate estuaries containing shellfish aquaculture, different field sites with varying attributes were chosen. Turbulence and vertical mixing are key components in the system, so it was important that sites with varying levels of turbulence were chosen.

The first site discussed, Limfjorden, is a very low energy estuary, in which stratification persists for much of the time during summer. The low turbulence levels limit the supply of food, oxygen and nutrients to the mussels. By contrast, the Oosterschelde is a tidally energetic environment which remains mixed throughout the tidal cycle.

5.1 Limfjorden

Limfjorden in Denmark is a large, shallow body of water lying across the Jutland peninsular connected to the North Sea on the west coast, and the Kattegat on the east coast. Both connections, Sallingsund in the West, and Aggersund in the East are shallow channels. The two other channels draining into the central basin (Risgårde and Feggesund) are of limited importance for the main through flow. The centre of Limfjorden opens in to a large shallow basin, Løgstør Bredning, where the field sites of the present study were located (figure 5.1). The total volume of water in Limfjorden amounts to 7.1 km^3, the average water depth is about 4.5 m. The depth of Løgstør Bredning is on average 5.8 m (Wiles, van Duren *et al.*, 2006).

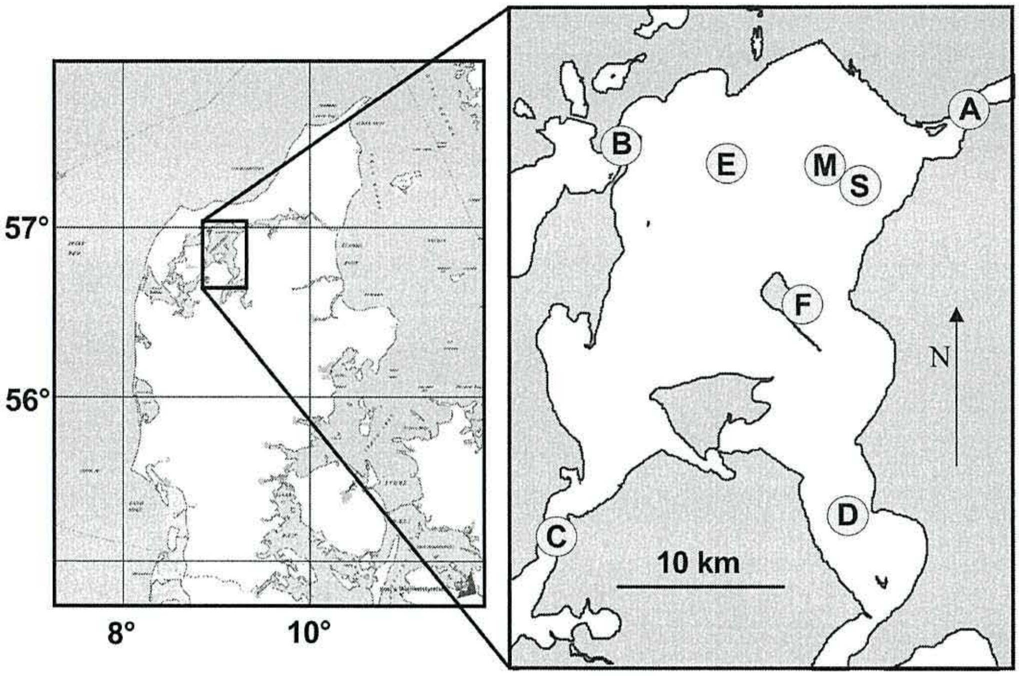

Figure 5.1. Map of Løgstør Bredning study area. Sallingsund (C), Feggesund (B), Aggersund (A) and Risgårde (D) are the 4 boundary mooring locations. E indicates the long term monitoring station 3708 operated by the council and F indicates the Livø meteorological station. M and S represent the mussel and sandy sites, respectively.

Throughout most of the year, the wind blows from a westerly direction, with the exception of the summer period, which is dominated by easterly winds that are usually low in energy. Water temperatures in Limfjorden average around 2-3 °C in the winter period, and 15-17 °C in the summer period. There is a constant intrusion of high saline water from the North Sea (32-34 psu) and an input from the Kattegat of low saline water (19-25 psu). Furthermore, there is a freshwater input of 2.7 km^3 per year from the surrounding area. Limfjorden is a micro tidal system with a tidal amplitude of 0.1-0.2 m. During summer, water exchange and circulation through Limfjorden are mainly driven by a predominantly easterly wind (Dolmer, 2000). A combination of wind and tide is responsible for a net flow from the North Sea (Thyborøn kanal) through Limfjorden to the Kattegat of 8.7 km^3 $year^{-1}$ on average. The corresponding residence time of the water is around 225 days on average for the entire water body (Dame *et al.*, 1998).

Limfjorden is a eutrophic water body affected by nutrient input from the surrounding watershed. This results in high primary production rates of up to 1000 mg C m^{-2} d^{-1} in summer (Dolmer *et al.*, 2002) which supports a high level of biomass of benthic suspension feeders. Limfjorden contains a large mussel fishery based primarily on a wild population with annual landings of 80,000-100,000 t of mussels. A large proportion of these fisheries are located in Løgstør Bredning. The majority of mussels are harvested from the bed, although mussels grown from rafts are becoming more common.

In Limfjorden little displacement of mussels takes place. In a cycle over several years different zones of the fjord are harvested for mussels. Restocking takes place by natural recruitment, and the population re-develops after a harvesting event over several years before it is harvested again. A production cycle typically takes 4 years.

5.2 Oosterschelde

The Oosterschelde is the southernmost estuary in the Netherlands, and also supports a large mussel industry. The estuary was part of a delta for the rivers Rhine, Meuse and Scheldt, but as a result of major engineering works over the period 1957 to 1987 (following a catastrophic storm surge event in 1953) the characteristics of the Oosterschelde have been irreversibly changed (Smaal *et al.*, 1992).

In 1987, the completion of a storm surge barrier across the mouth of the Oosterschelde allowed the control of the major exchange mechanism with the North Sea (figure 5.2). Areas in the Northern and Eastern branches of the Oosterschelde were segregated from the estuary by the Grevelingendam (1967), the Volkerakdam (1969), the Philipsdam (1986) and the Oesterdam (1987) (Mulder *et al.*, 1994).

As a result, tidal exchange with the North Sea has been reduced – the cross-sectional area at the mouth of the estuary was reduced from 80,000 m^2 to 17,900 m^2, the mean tidal range and current velocities within the estuary have decreased while the salinity has increased (table 5-1). The volume of water passing through the storm surge barrier dropped from 1283×10^6 m^3 to 915×10^6 m^3 per tidal cycle. This controlled entrance to the North Sea through the storm surge barrier is now effectively the only exchange mechanism in the Oosterschelde.

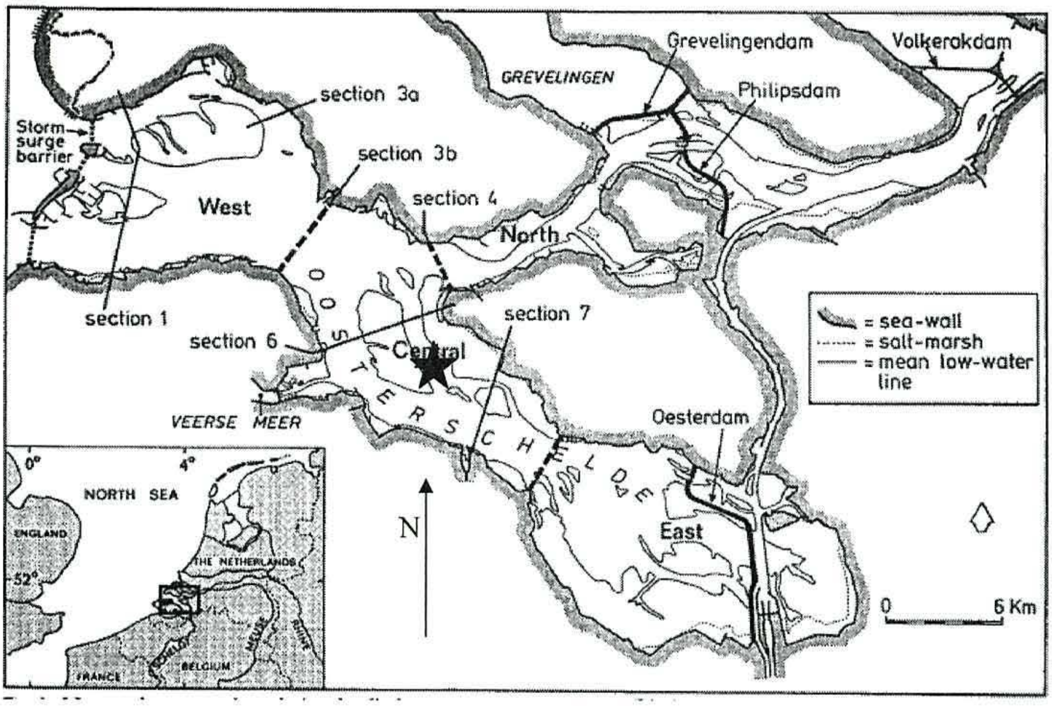

Figure 5.2 The geography of the Oosterschelde. The major engineering works (storm surge barrier, Grevelingdam, Volkerakdam, Philipsdam and Oesterdam) are labelled on the diagram, as are the descriptive regions (West, Central, East and North). The black contour line indicates the 10 m depth contour relative to the National Dutch datum (from Vroon, 1994). The star indicates the study site used in this dissertation. More detailed maps of the study site are given in figure 5.3 and figure 5.4.

The reduction in river input from 70 m3 s-1 to 25 m3 s-1 (the freshwater inputs are now completely managed) caused nutrient levels to decrease in the estuary in the post barrier era (Smaal et al., 1992). Primary production remained relatively constant with a annual range of 550 to 1100 mgC m-2 d-1, probably because the decrease in nutrients was offset by increased light penetration (Nienhuis et al., 1994).

Smaal *et al.*, 1992 concluded "The import of food from the North Sea, was a non-significant contribution in the food web of the total Oosterschelde ecosystem", but that "On a local scale, import of phytoplankton from the North Sea has been an important food source for mussels cultivated in the western section of the Oosterschelde". The building of the storm surge barrier has reduced this import of phytoplankton from the North Sea. While average concentrations of chlorophyll have decreased in the western and central sections, they have remained constant in the eastern section and increased in the northern section.

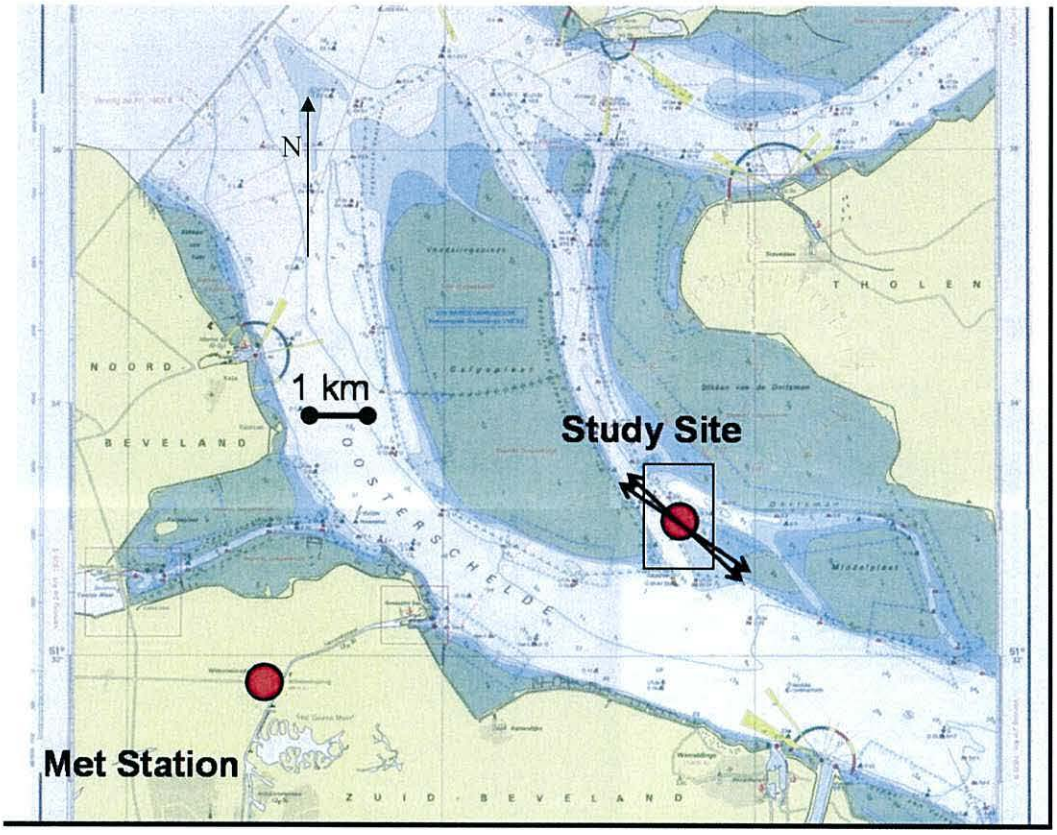

Figure 5.3. A map of the region surrounding the study site. A map of all the Oosterschelde is given in figure 5.2. The black rectangle indicates the region blown up in figure 5.4. The two arrows marked at the study site show the directions of the rectilinear M2 tide over mussels and sand.

The residence time of the estuary was estimated by Luis Fernandez using Mohid (see Coelho *et al.*, 2002) model runs of the estuary. The model was 'seeded' with tracer particles, and the fraction of particles remaining in the estuary over time was calculated, giving an e-folding time of ~ 6 days. The numbers given in table 5-1 also give a flushing time of ~ 6 days.

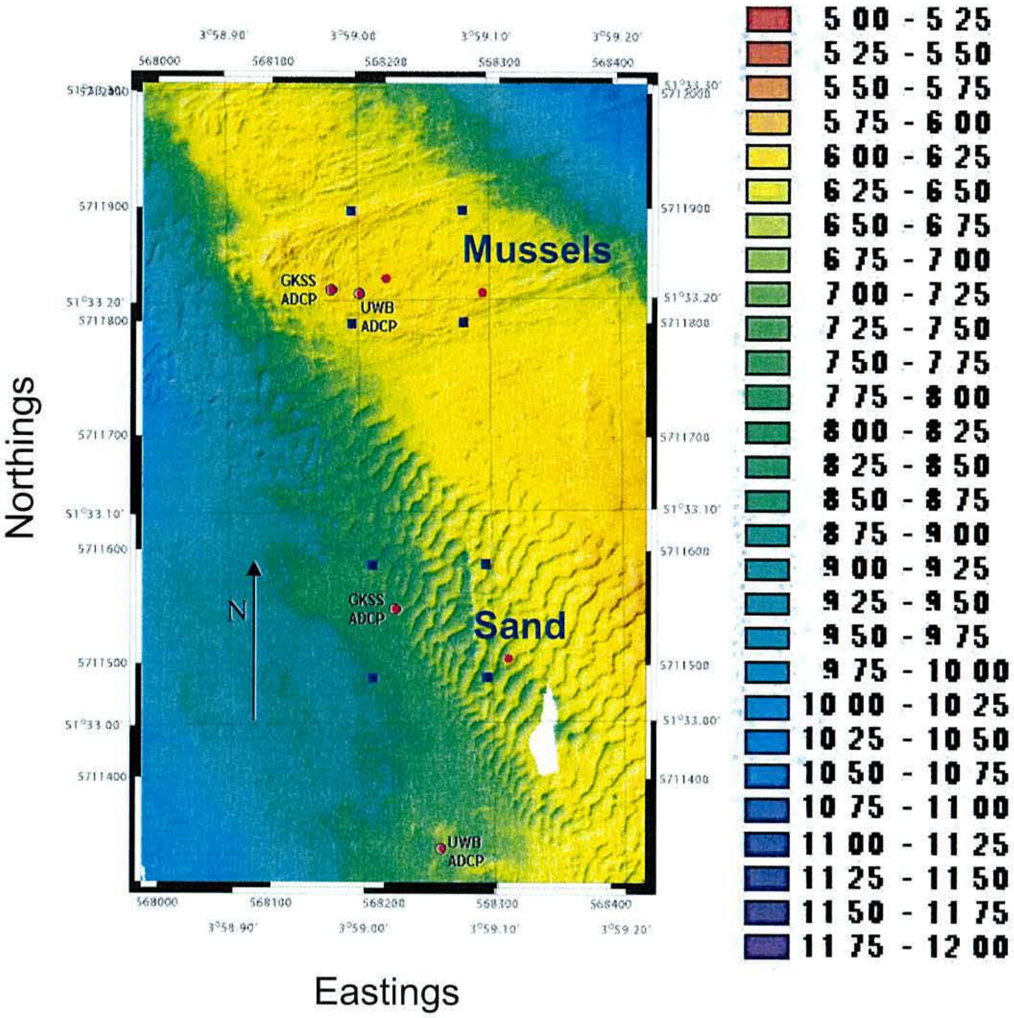

Figure 5.4. Bathymetry and equipment locations at the Oosterschelde field sites. The colour scale is given on the right in centimetres below Dutch datum. Data is from the GKSS Multibeam sonar. The Mussel site is shown by the 4 blue dots at the top of the figure (the upwards looking ADCP is denoted by the UWB ADCP mark) and the sand site is shown by the 4 dots at the bottom of the picture (the upwards looking ADCP is south of the marked square).

The ecosystem is dominated by benthic filter feeders; cockles, mussels (Klepper, 1989: Smaal *et al.*, 1986), and more recently the pacific oyster (Drinkwaard, 1998). 50,000 tonne of mussels were landed in the season 2003/2004 (http://www.pvis.nl/mosselkantoor/), however this is down from 150,000 tonne landed in the 1993/1994 and 1997/1998 seasons (the price per kilo of mussels has doubled since 1998). This drop in harvest is caused by a low availability of spat from the Wadden sea. Mussels are cultivated on an area of 22.53 km^2 of marked lots (Smaal *et al.*, 1992), mostly in the central and western region and are predominantly harvested from the bed. The mussel spat is imported into the Oosterschelde and laid onto marked lots of area 100m×500m aligned across the flow (figure 5.4). The mussels then congregate into patches a few metres across, separated by sand (Van de Koppel *et al.*, 2001). Unfortunately, photos couldn't be taken as the visibility was poor during a phaeocystis bloom at the time of the campaign.

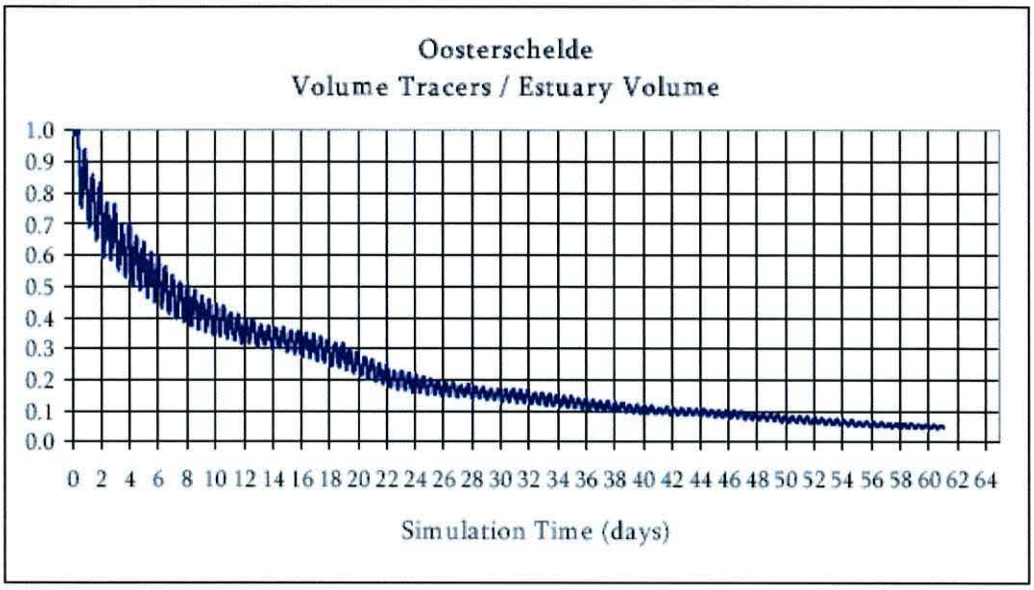

Figure 5.5. Residence time of the Oosterschelde estuary. A large number of tracers were 'released' into a numerical model and allowed to advect with the tidal flow. The fraction of tracers left inside as a function of time is shown (Fernandes *et al.*, 2006).

In Oosterschelde, stocking is mainly by transport of mussel spat from the Dutch Wadden Sea onto culture plots. Mussels on the plots are relocated to different plots if needed, and also sometimes dredged and replaced to remove starfish and crabs. Production cycles take 2 to 3 years.

The western and central sections of the Oosterschelde consist of large sandy shoals and gullies of up to 55m deep, while the eastern section is relatively shallow with a mean depth of 4.13m. The mean gully depth decreases from 30m at the storm surge barrier to 10m in a landwards direction – the mean basin depth decreases from 12 m at the barrier to 4 m in a landwards direction.

	Pre-Barrier	Post-Barrier
Total Surface, km^2	452	351
Water surface (MWL), km^2	362	304
Intertidal area, km^2	183	118
Salt Marshes, km^2	17.2	6.4
Cross section, barrier in open position, m^2	80000	17900
Mean tidal range, Yerseke, m	3.70	3.25
Max. flow velocity, m s^{-1}	1.5	1.0
Mean tidal volume m^3 × 10^6	1283	915
Total volume m^3 × 10^6	3050	2750
Mean freshwater load, m^3 s^{-1}	70	25
Salinity (ppt)	>25	>30

Table 5-1. Properties of the Oosterschelde pre-barrier (1987) and post barrier. Data from Nienhuis *et al.*, 1994 and Ten Brinke *et al.*, 1994.

5.3 Comparison

The low energy environment in Limfjorden results in low levels of vertical mixing and therefore vertical transport of food to benthic mussels. Hence boundary layer depletion occurs readily during calm periods. The low flow velocities in Limfjorden make the role of mussels as roughness elements almost irrelevant. The only discernable influence of mussels on turbulence levels is the energy dissipated from their exhalant jets, which is confined to the very near bed region and maintains a level of ~2 J m^{-3} (see section 8.2 and van Duren *et al.*, 2005). Meteorological forcing is the major driving force of vertical mixing, so that periods of stratification and limited mussel food supply are determined by the timescale of weather events (from days to weeks). During prolonged periods of calm conditions, stratification becomes significant in the Limfjorden, inhibiting the vertical transport of phytoplankton, nutrients and oxygen in the water column. This can be disastrous for benthic mussel communities.

In Oosterschelde, local food depletion above the mussels is of limited importance due to strong vertical mixing by the tidal currents. Nevertheless a reduction in particle concentration above the mussel bed was observed by divers at slack tide. Although the enhanced roughness of the mussel bed does influence turbulent mixing of the water column, this process is not a limiting factor for the supply of food to mussels. A mussel bed in this tidal system can attain very high mussel biomass without limitations due to local vertical food depletion. By contrast, lateral transport processes are important. Advection of phytoplankton from primary production (source) regions to consumption (sink) regions has a large influence on food supply to mussels. The positioning of the mussel bed with respect to the depth and current distribution in the estuary, as well as its proximity to the boundary to the sea (which acts as a source of nutrients and phytoplankton), is important to determine a site's suitability for mussel culture.

The observational challenge in Limfjorden is to measure turbulence in the very low energy environment, which will challenge existing current measuring instruments. The strong turbulence signal in the Oosterschelde is an opportunity to apply new methods of turbulence measurement.

6 Experimental Design:

The aim of the field campaigns at both sites was to investigate the different processes occuring above a benthic mussel bed and above a control sand site. Do mussels enhance turbulence? If so, under what conditions? What levels of turbulence are observed around mussel aquaculture and how does this affect the coupling of the mussels to the upper water column?

Originally, microstructure profilers were to be used to estimate turbulence parameters in the study environments. This turned out to be impractical, as the shallow environments do not allow the profiler to attain a suitable fall speed. The alternative approach taken is to use ADCPs by applying the variance and structure function methods. Unfortunately, ADCPs do not measure the very near bed region (which is immediately adjacent to the mussels) because of the ADCP blanking region. ADV's were used to take spot measurements in this near bed area, and during the Limfjorden campaign, 2 other high resolution ADCPs were also orientated downwards in order to capture the near bed region.

Under the MaBenE framework, the turbulence results reported here have been combined with supporting biology and sediment measurements in order to investigate the effects of turbulence upon the mussels. The results of these inter-disciplinary studies will be published elsewhere.

6.1 Limfjorden

Field observations were undertaken in Limfjorden from the 26th of May until the 6th of June 2003 with a focus on the study site in Løgstør Bredning (figure 5.1). Current meters with temperature and salinity loggers were deployed at a long term monitoring station (E), at the study site (M and S) and at the 4 boundaries to Løgstør Bredning (Sallingsund, Feggesund, Aggersund and Risgårde). A permanent meteorological station was located on the island of Livø, which measured wind speed and direction, temperature, humidity and solar radiation. During the two weeks of the campaign, the weather was, on average, exceptionally warm and calm for the area. For several consecutive days there was virtually no wind.

Two sites of interest were identified before field measurements commenced: one area over mussel beds (M – see figure 5.1) and the other, which was 950 m to the southeast, over sand (S). Water depth at the mussel site was about 7 m, and at the sandy site around 5 m. In Limfjorden the mussels tend to be distributed in banded patterns. A video survey of the mussel site indicated that the width of most of these bands was around 25 cm, although there were a few larger patches with a cross-section of several meters.

Four 1200 kHz RDI ADCPs were placed by divers on the bed, two at the mussel site and two at the sandy site. Over each location one ADCP was configured to 'look' upwards form the bed to measure water currents in 30 cm bins (figure 6.1a) and one ADCP was configured to look downwards to measure high-resolution water currents in 5cm bins as close to the bed as possible. The upward looking ADCPs were levelled and configured to measure turbulent kinetic energy and shear stresses. The accuracy of the height of the ADCP bins above the bed is difficult to gauge. As the bed is not completely flat and level, the definition of a particular height above the bed can only be accurate to within O(10cm).

During the two weeks of field observations, two vessels were collecting CTD data over both the mussel site and the sandy site. The *RV Storch* used a CTD that was also equipped with optical sensors (transmission and backscatter) and the *RV Genetica II* used a CTD equipped with a fluorometer. A thermistor string was set up to record the temperature profile over the mussel site but only the bottom three thermistors survived recovery. CTD casts were taken every 2-3 days at the boundary points. Scientists from the County of Viborg were also performing routine CTD measurements at a number of locations throughout Limfjorden at the same time as our observations.

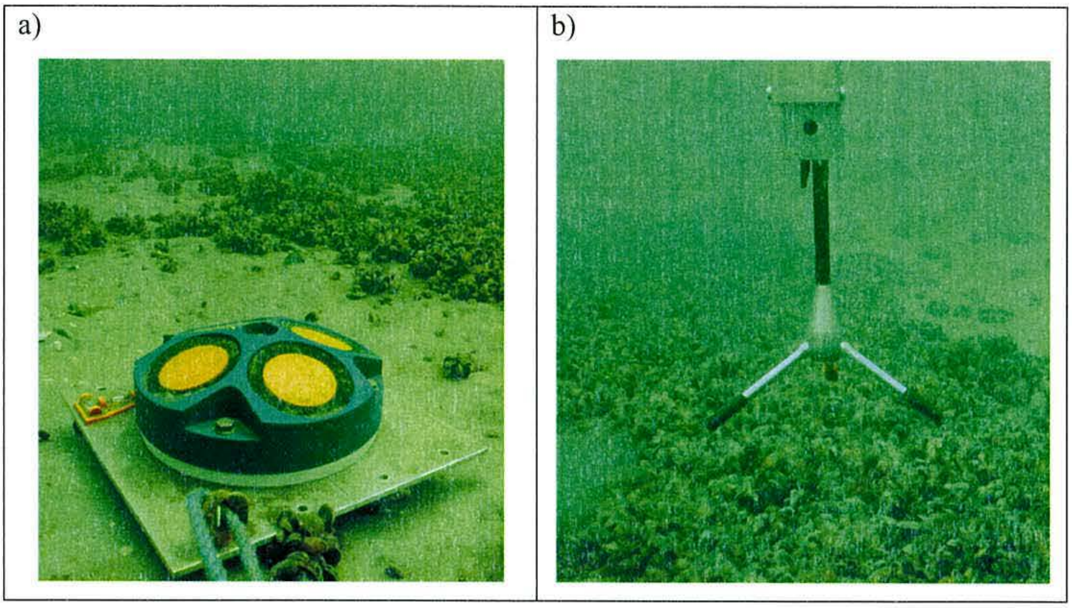

Figure 6.1. (a) The ADCP deployed at the mussel site in Limfjorden. (b) The Nortek Vector ADV in situ above a mussel bed. The background of both photos shows examples of the banded mussel patterns found in Limfjorden (Photos courtesy of Jens Larsen, NERI).

A Nortek 'Vector' ADV (figure 6.1b) was employed to obtain fine scale velocity and turbulence measurements. This instruments was set to measure two time series at a height of 1.9 m from the bed, one series at the mussel site and one series at the sandy site, each of about one day duration. The height of 1.9m was chosen such that the ADV was within the ADCP measuring range. They consisted of burst measurements of 9600 data points collected at 16 Hz These series were used to provide more direct and detailed measurements of turbulent kinetic energy to supplement the ADCP estimates. Three other ADV series were collected with the measuring volume of the ADV 2-3 cm off the bed. One series over the middle of a mussel patch, one series over the sandy site and one series over the edge of one of the mussel patches. These series consisted of burst measurements of 8192 data points collected at 32 Hz.

The turbulence and mean flow measurements were complemented by surface wave records from a Directional Wave Rider Buoy (Datawell, NL), which was moored over the mussel site to determine the period and amplitude of waves passing through the system.

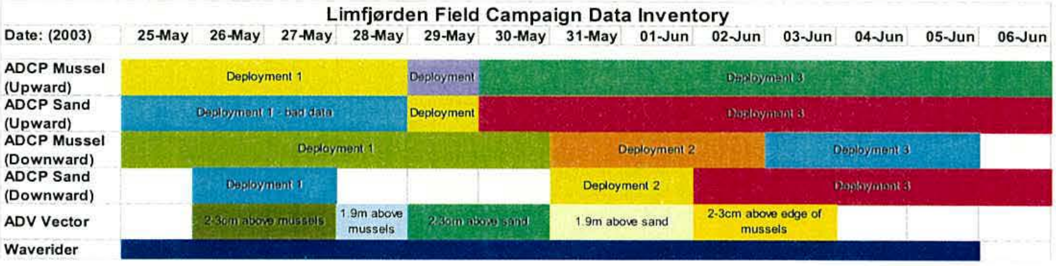

Limfjørden Field Campaign Data Inventory

Date: (2003)	25-May	26-May	27-May	28-May	29-May	30-May	31-May	01-Jun	02-Jun	03-Jun	04-Jun	05-Jun	06-Jun
ADCP Mussel (Upward)	Deployment 1				Deployment	Deployment 3							
ADCP Sand (Upward)	Deployment 1 - bad data				Deployment	Deployment 3							
ADCP Mussel (Downward)	Deployment 1						Deployment 2			Deployment 3			
ADCP Sand (Downward)		Deployment 1					Deployment 2		Deployment 3				
ADV Vector		2-3cm above mussels		1.9m above mussels	2-3cm above sand		1.9m above sand		2-3cm above edge of mussels				
Waverider	■												

Table 6-1. Hydrodynamic data collected during the Limfjorden field campaign.

6.2 Oosterschelde

Field observations were undertaken in the Oosterschelde from 4th May 2004 until 13th May 2004. Two sites of interest were identified, a control site over a sandy region and a mussel site situated 240m to the north. A 100 by 100 m square area was marked at each site with navigation buoys to deter ship traffic, and most of the scientific equipment used during the campaign was deployed within these squares (figure 5.3 and figure 5.4). The second ADCP sand deployment could not be placed inside the experimental square.

A meteorological station, recording temperature, relative humidity, irradiance and wind speed and direction, was located at Wilhelminadorp (51° 31.8'N 3° 53.6'E see figure 5.3). A Directional Wave Rider Buoy (Datawell, NL) was situated between the two sites. The mean period of the waves is ~ 2.5s, therefore the wavelength of the dominant waves is $\lambda = gT^2/2\pi \approx 6\,\mathrm{m}$ (figure 6.2). The waves can therefore be classified as deep water waves. During the peak wave periods (May 4th and May 7th), the significant wave height reached 0.6m. Linear wave theory gives the wave velocities at the bed as 0.017 m s^{-1} at these times. Hence the near bed wave orbital velocities are insignificant compared to the tidal velocities.

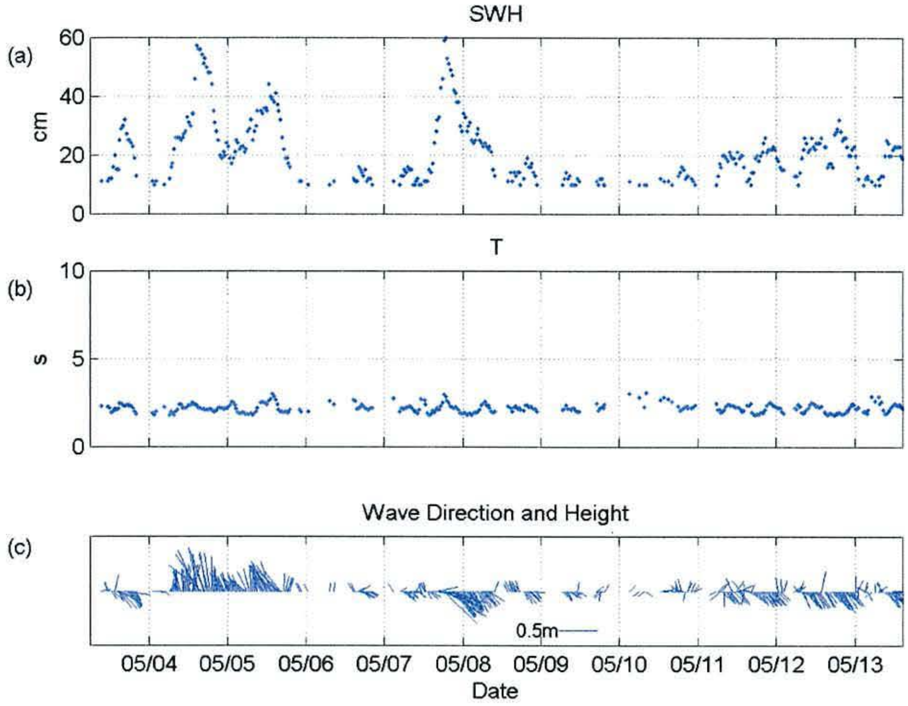

Figure 6.2. Wave conditions at the Oosterschelde field site. (a) Significant Wave Height, (b) wave period and (c) wave direction and height (stick indicates direction to).

Upward-looking ADCPs were deployed over the sand site and the mussel site. The ADCPs had identical configuration files, except the ADCP deployed at the mussel bed had a lower blanking interval as this ADCP was equipped with zed-hed technology allowing a smaller blanking interval. The ADCP at the mussel site was buried into the sediment by divers (figure 6.3a) such that the transducer was 5 cm above the bed. This was also attempted at the sand site, but the ADCP was scoured out due to the strong flow and mobile bed. This meant the first deployment gave no good data, so an aluminium frame was used for the second deployment (figure 6.3b) which raised the height of the ADCP transducer to 0.5 metres above the bed.

The ADCPs employed RDI's mode 12 (rapid pinging mode) and were configured to average 10 subpings over one second to create one velocity estimate. The bin sizes were 30cm and the ambiguity velocity was set to 1.75 m s^{-1}. The distance from the bed to the centre of the first bin was 0.5 m for the mussel bed site ADCP and 1.34 m for the sand site ADCP.

The ADCPs were levelled by divers and were set to record the along beam velocities so they could be used to estimate turbulent parameters. The ADCPs were recovered mid-way through the field campaign for data downloading and battery replacement.

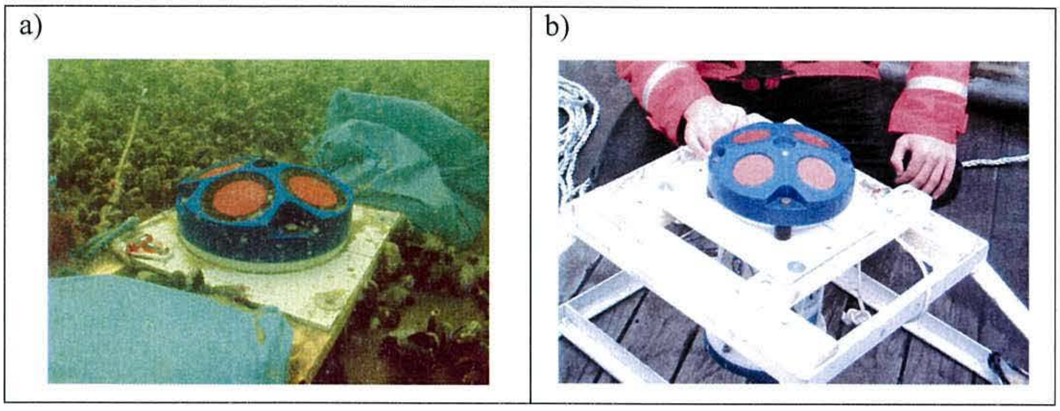

Figure 6.3. The ADCP moorings used in the Oosterschelde. (a) over the mussel site the ADCP was buried into the sediment to reduce the blanking interval near the bed. (b) at the sand site the ADCP was mounted in an aluminium frame because the bed was more mobile.

Two ADVs were used to take spot measurements of velocities in the Oosterschelde. They were a Sontek Hydra ADV and a Nortek Vector ADV.

The frame supporting the Sontek Hydra ADV was quickly covered in macro-algae which drastically affected the local water flow so data was not used for analysis. The Nortek ADV was used for two deployments, the first over the centre of a mussel patch and the second over a sand region.

The deployment over the centre of a mussel patch was from 0900 on 6th May until 1100 on 8th May. The measuring volume was set by divers to be 7 cm above the mussel bed, although this could not be precisely measured as the level of the bed was not well defined due to roughness elements (mussel bedforms). The ADV took bursts of samples every 28 minutes. Velocity samples were taken at 64 Hz for a period of 129 seconds (i.e. 8256 samples).

The deployment over the sand site was from 1120 on May 9th until 0800 on May 13th. The ADV measuring volume was again set to be 7 cm above the bed. The time between bursts in this deployment was 58 minutes (to conserve memory usage). Velocity samples were again taken at 64 Hz for a period of 129 seconds.

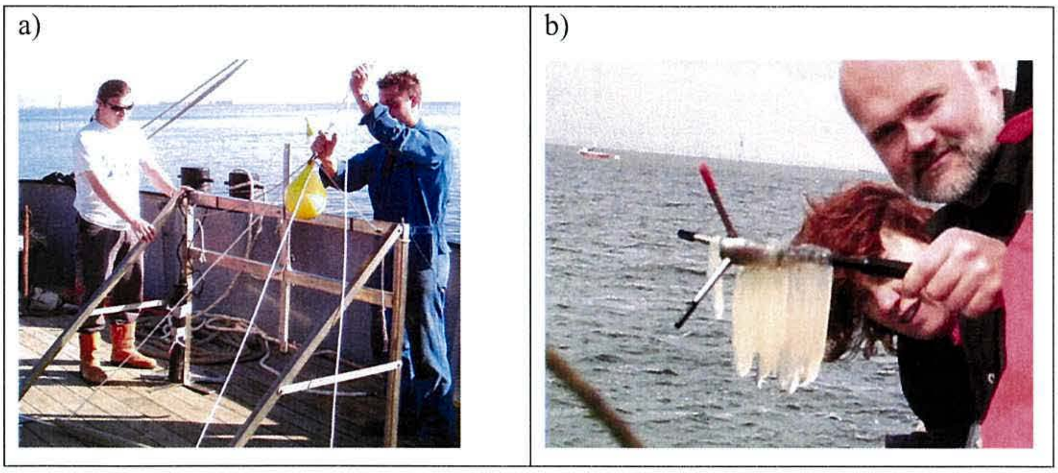

Figure 6.4 a) Nortek vector ADV prior to deployment. The ADV data recording casing and the sensor head were strapped to the furthest leg during deployment. After deployment, the divers attached the sensor head to the bottom side of the spar (below the yellow buoy). b) The ADV sensor head on recovery. Biology had attached itself to the sensor head, however this did not appear to affect ADV's performance.

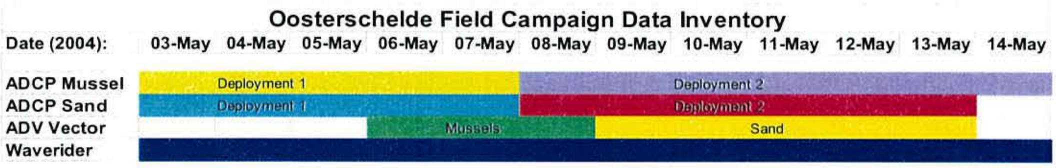

<table>
<tr><th colspan="13">Oosterschelde Field Campaign Data Inventory</th></tr>
<tr><th>Date (2004):</th><th>03-May</th><th>04-May</th><th>05-May</th><th>06-May</th><th>07-May</th><th>08-May</th><th>09-May</th><th>10-May</th><th>11-May</th><th>12-May</th><th>13-May</th><th>14-May</th></tr>
<tr><td>ADCP Mussel</td><td colspan="5">Deployment 1</td><td colspan="7">Deployment 2</td></tr>
<tr><td>ADCP Sand</td><td colspan="5">Deployment 1</td><td colspan="6">Deployment 2</td><td></td></tr>
<tr><td>ADV Vector</td><td></td><td></td><td></td><td colspan="3">Mussels</td><td colspan="5">Sand</td><td></td></tr>
<tr><td>Waverider</td><td colspan="12">■</td></tr>
</table>

Table 6-2. Hydrodynamic data collected during the Oosterschelde campaign.

7 Limfjorden results

The field campaign in Limfjorden was designed to measure turbulence parameters alongside vertical gradients of nutrients, phytoplankton, etc. above a mussel bed and compare this to similar parameters measured above a sand site. The water column structure is presented, then the mean flow structure, followed by the measurements of turbulence.

The turbulence levels were low. Spot measurements were taken with an ADV, however the turbulence was below the noise limit for the ADCP. An analytical model describing stratification (and associated vertical mixing) using a potential energy model (Simpson *et al.*, 1981) is developed.

7.1 Results of the observational campaign.

7.1.1 Water column structure

The CTD time series during the campaign over the mussel bed and sandy site are contoured in figure 7.1. There was a general warming trend over the period (from 13°C to 17°C) along with a salinity increase. These two effects opposed each other such that the density of the water remained approximately constant. The contour plots show switching of the water column between mixed (e.g. decimal days 152-153) and stratified (e.g. decimal day 148-149). There is the signal of a cool, saline tongue of water advecting over the mussel bed and the sandy site around decimal day 149.

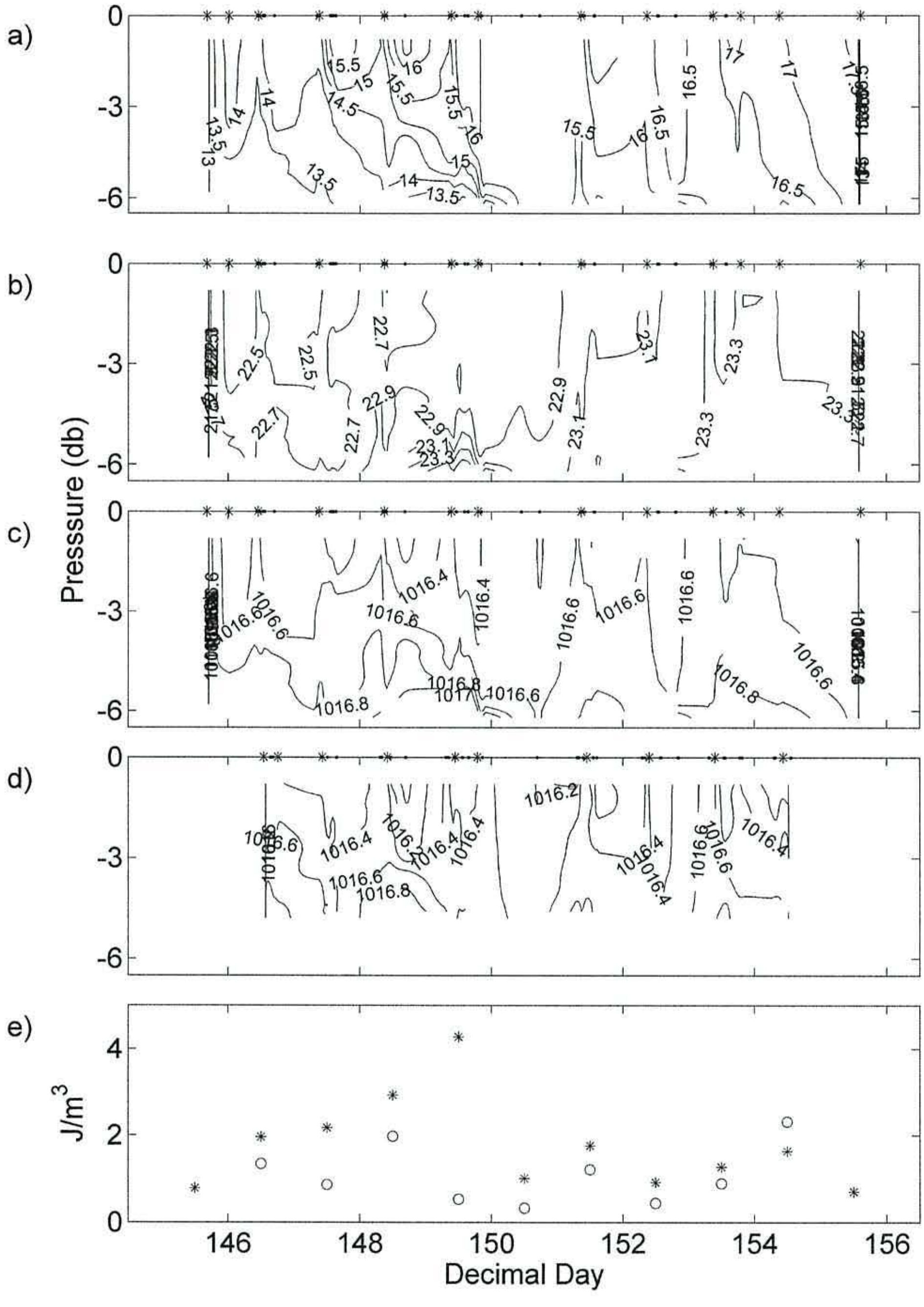

Figure 7.1. Water column properties from CTD casts. Data here is taken from both the *RV Genetica II* ctd and the *RV Storch* ctd. a) Temperature over the mussel bed (°C); b) salinity over the mussel bed (psu); c) density over the mussel bed (kg m^{-3}); d) density over the sandy site (kg m^{-3}). The marks on the upper x axis indicate the times of the CTD casts (* - *Genetica*, . - *Storch*). e) Daily average potential energy anomaly φ calculated from mussel (*) and sand (o) density profiles (see section 7.2.1).

7.1.2 Mean flow field

The ADCP data for the corresponding time period is plotted in figure 7.2. The vertical structure of the velocities varied substantially depending on whether the water column was mixed or stratified. During periods when the water column was well mixed, the velocities were close to being uniform with depth. By contrast, during periods of stratification, there was evidence of a periodic signal in the velocities with the upper and lower-layer velocities in anti-phase. This component has a period of ~14 hours, predominantly in the clockwise direction, which is close to the inertial period for 57 °N (figure 7.3). This indicates a significant component of wind-forced near inertial motion with the bottom layer responding in anti-phase due to the presence of the lateral boundaries (Simpson *et al.*, 2002). As the 21 hour moving window only allows limited resolution near the inertial frequency, a rotary spectra analysis was also performed on the whole of deployment 3 (figure 7.4). This shows a clearer peak in the clockwise spectra around 14.3 hours.

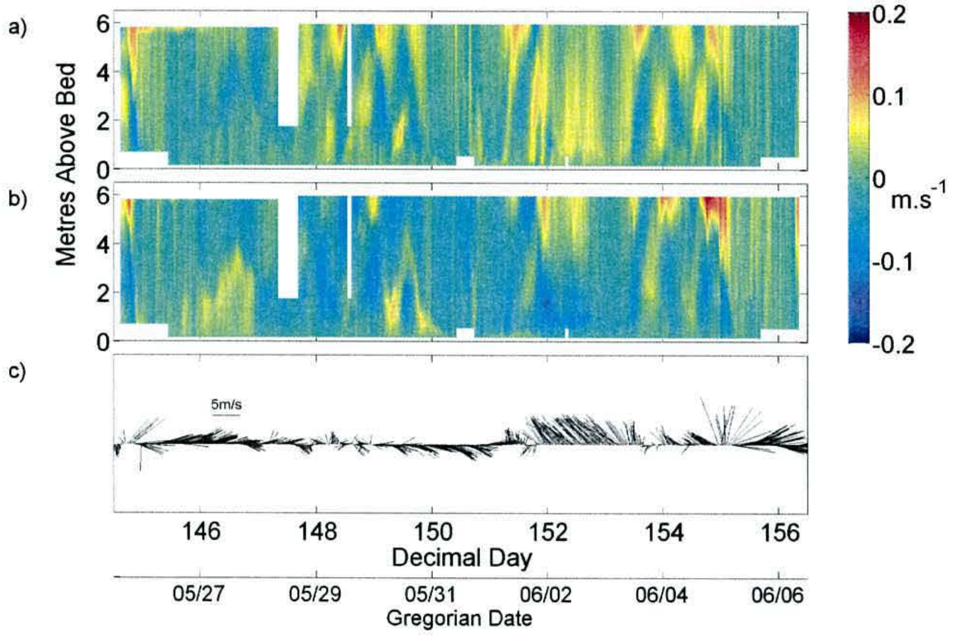

Figure 7.2. a) East velocities and b) north velocities measured by both the upwards looking and downwards looking 1200 kHz ADCPs over the mussel bed. The white gaps in a) and b) are when the ADCPs were removed for downloading. c) Wind velocity and direction.

The two layer flow observed did not appear to have a signal of estuarine circulation. The background density field of a density gradient from south west to north east would imply a residual estuarine circulation with water near the bed flowing towards the north east and water near the surface flowing towards the south west.

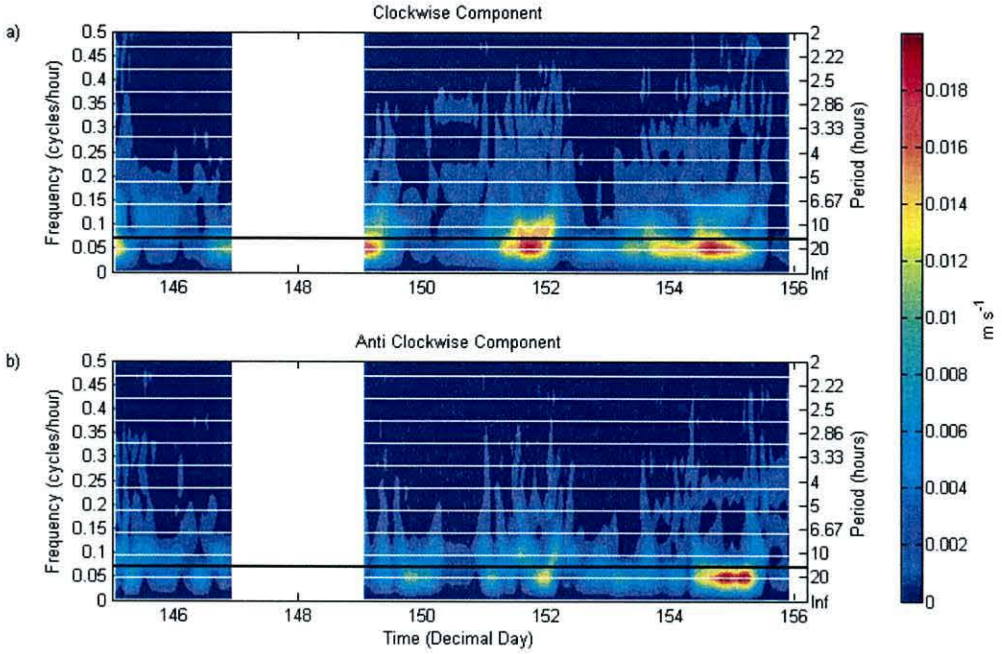

Figure 7.3. Rotary spectra of the ADCP mean velocity data at the Mussel site (figure 7.2). (a) Clockwise spectra and (b) anti-clockwise spectra. The black line shows the inertial period of 14.3 hours. The white horizontal lines indicate where the frequencies are resolved by the fouier transform. The spectra were calculated over a 21 hour moving window for the velocities between 5.35 and 5.95 m. Deployment 2 is not included as the length of the deployment did not exceed 21 hours.

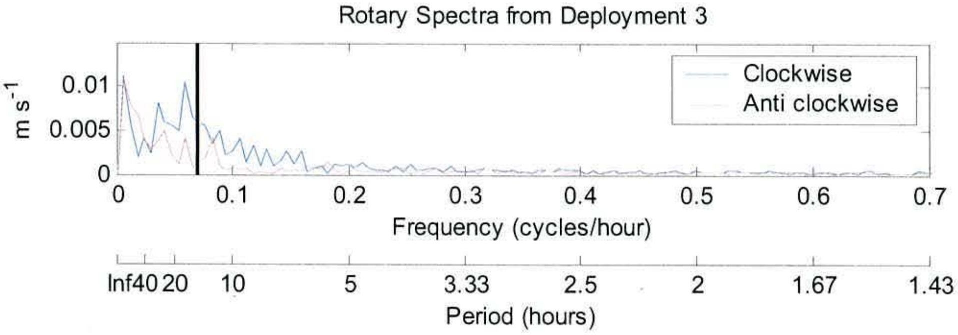

Figure 7.4. Rotary spectra calculated between the heights of 5.35 and 5.95 m for the whole of deployment 3. The black line shows the inertial period of 14.3 hours.

7.1.3 Mixing and Turbulence

Due to the low energy levels encountered in the Limfjorden, the turbulent parameters could not be determined using the ADCP variance method. However the ADV was able to take detailed turbulence measurements in the field due to it's high sampling frequency. The ADV measured maximum Reynolds stresses near the bed of ~ 0.002 Pa, supporting our assumption that tidal stirring was very low. Estimates of turbulent kinetic energy (TKE) levels from ADV measurements were made directly on the basis of the fluctuations of the velocity components ($TKE = \frac{\rho}{2}\left(\overline{u'^2} + \overline{v'^2} + \overline{w'^2}\right)$). The 5 series of ADV measurements taken in Limfjorden were at different locations and under different weather conditions, which makes direct comparison difficult. Comparison of the *TKE* levels measured by the ADV with the significant wave height (figure 7.5) closely tracked the wave conditions.

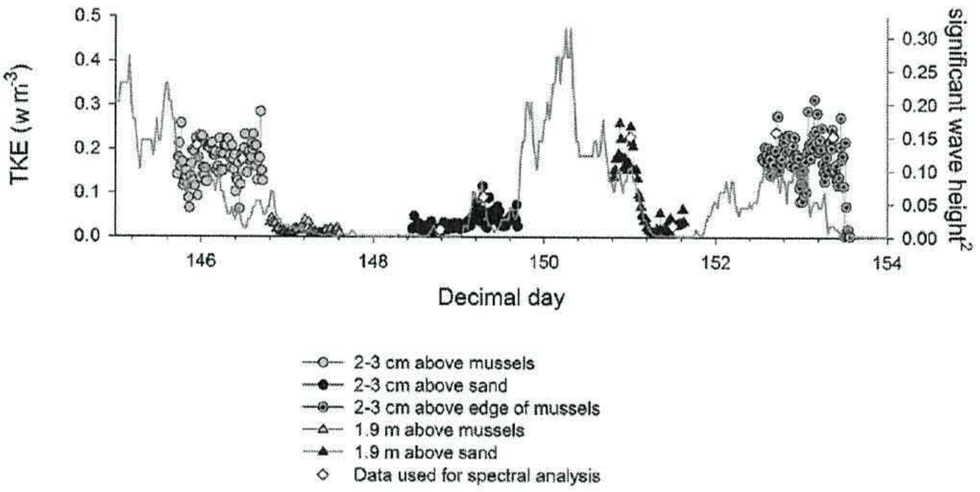

Figure 7.5. The comparison of TKE as measured by the ADV and Significant Wave Height (SWH). The two track each other well, however wave orbital motions have not been removed.

7.1.4 Boundary Conditions

In order to predict the turbulence conditions at the study site in the absence of reliable direct measurements, boundary forcings on the estuary were observed.

The wind measured at the met station on Livø is shown in figure 7.6. The winds were generally light (< 5 m s^{-1}) with 3 intervals when the wind was consistently stronger than 5 m s^{-1}: decimal day 145-157, when the wind was from the west-southwest, 152-153.5 from southeast and 155-156 shifting from south to west. There was also a period of moderate winds (~ 5 m s^{-1}) from decimal day 150-151 from the west-northwest, which has a relatively large fetch.

The wind speed and wave height (figure 7.6a and b) are clearly correlated but there are significant differences, for example the strongest winds (at decimal day 153.0, around 7 m s^{-1}) do not coincide with the highest waves. At this time the wind is coming from the southeast and so has a relatively small fetch at the study site. These intervals of strong wind speed and large waves coincide with the mixed periods shown by the density and velocity data (figure 7.1 & 2).

The surface heat exchange (figure 7.6c) was estimated for Limfjorden on the basis of the measurements at Livø of solar radiation, wind, atmospheric temperature and humidity. The surface heat exchange consisted of solar heating, evaporation and sensible heat transfer. A strong positive heat input occurred on most days of the campaign with relatively weak cooling at night. Net heat input during the entire period was at a rate of ~ 160 W m^{-2}, which was in accordance with the measured temperature increase of ~ 4°C.

The salinity gradient within Løgstør Bredning during our observations was from 28.5 psu at Sallingsund to 23 psu at Aggersund (figure 7.6d) over a distance of 34 km. Limited tidal ventilation of Limfjorden occurs mainly via Sallingsund and Aggersund, which are relatively narrow and constricted channels with peak flows during the observational period of order 0.25 m s-1. The tidal flows within the Løgstør Bredning are correspondingly small with velocities generally < 0.1 m s^{-1}. Flushing by the mean flow is also slow; the volume of Løgstør Bredning is around 3.2 km^3, while the volume flow through the Aggersund channel is about 280 m^3 s^{-1} giving a residence time of approximately 140 days, i.e. slightly more than half of the full residence time estimated for the whole of Limfjorden.

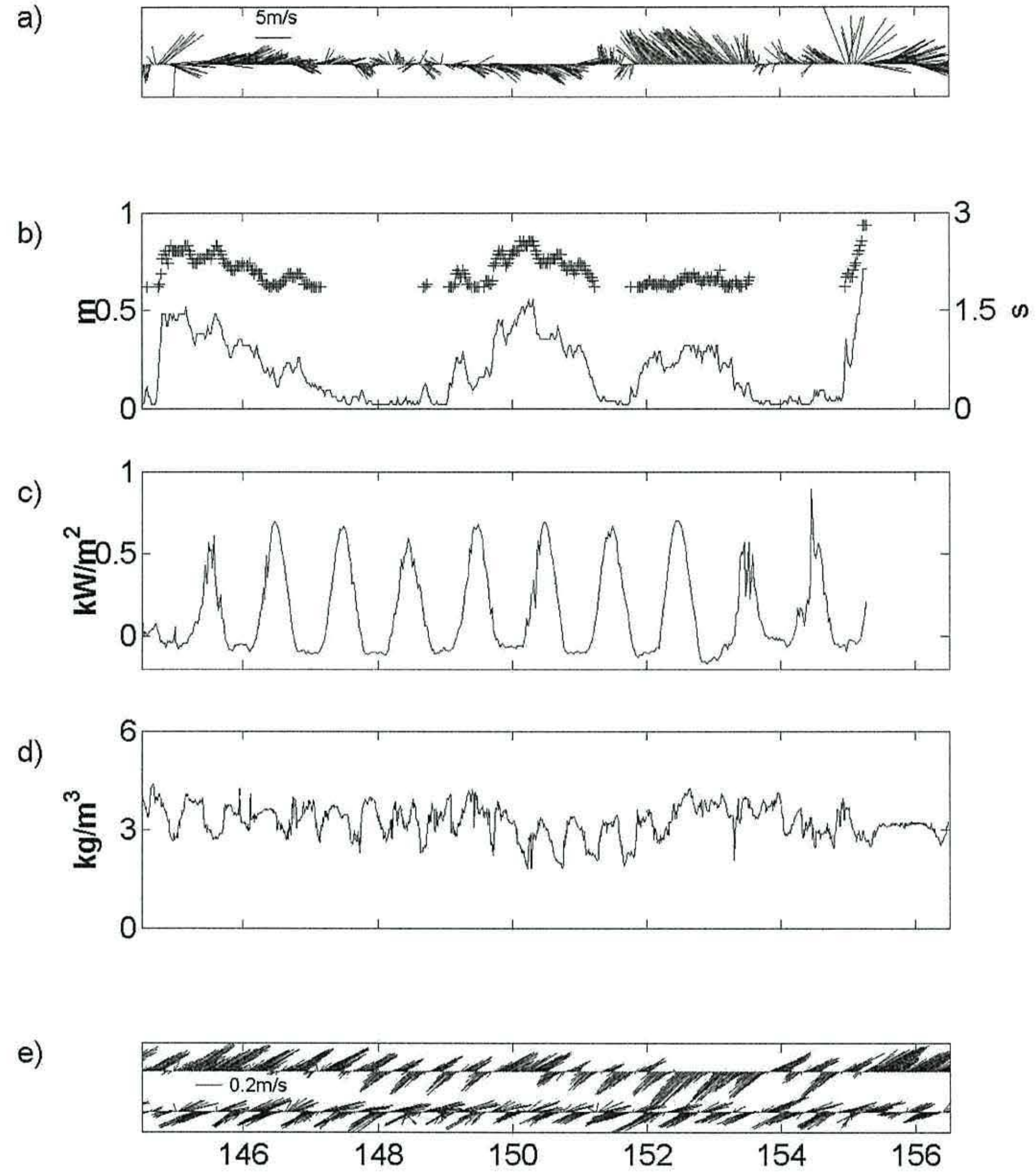

Figure 7.6. Boundary forcing conditions. a) Wind measured at the met station on Livø, the sticks indicate the direction the wind is blowing towards. b) Significant wave height (line — left axis) and mean period (+ — right axis) measured by the wave buoy moored at the mussel study site. c) Net heat transfer to water column. d) The density difference between Sallingsund and Aggersund. e) Currents measured by current meters at Aggersund (top) and Sallingsund (bottom). See figure 7.2 for a conversion from Decimal Day to Gregorian date.

7.2 Model Development

7.2.1 Water column stability

The density data can be used to make a quantitative representation of the water column stability in the form of the potential energy anomaly φ, defined as (Simpson *et al.*, 1981);

Equation 7.1 $\varphi = \frac{1}{h}\int(\bar{\rho} - \rho)gzdz$ where $\bar{\rho} = \frac{1}{h}\int \rho dz$

where $\rho(z)$ is the density profile and h is the water depth. φ represents the amount of energy required per unit volume to completely mix the water column. A large positive value of φ indicates strong stratification, and hence reduced vertical transport of scalar properties (e.g. phytoplankton). A negative value of φ represents an unstable water column.

Values of φ based on the CTD casts over both the mussel site and the sand site were always positive during the daytime measurements (figure 7.1e). Generally the φ results from the two sites track each other although those at the shallower sandy site were slightly lower. The degree of stratification (φ) increased from decimal day 146 to 149 up to a maximum value of 4.5 J m^{-3}. There was then a sharp reduction in φ on day 150 at the mussel bed site and a day earlier at the sand site.

The possible factors enhancing stratification, namely buoyancy inputs by surface heating and estuarine circulation, are compared against the opposing mixing factors, which include tidal mixing, convection, wind stirring and wave stirring. This competition shall be considered in terms of a model of water column stratification using the potential energy anomaly φ defined in equation 7.1. Following Simpson *et al.*, 1990, the contributions of the competing stratifying and mixing processes can be broken into their individual roles:

$$\left(\frac{\partial\varphi}{\partial t}\right) = \left(\frac{\partial\varphi}{\partial t}\right)_{\text{heat}} + \left(\frac{\partial\varphi}{\partial t}\right)_{\text{hdens}} + \left(\frac{\partial\varphi}{\partial t}\right)_{\text{tide}} + \left(\frac{\partial\varphi}{\partial t}\right)_{\text{waves}} + \left(\frac{\partial\varphi}{\partial t}\right)_{\text{wind}}$$

The relative significance of each of the above contributions will each be considered separately in the following sections.

7.3 Parameterisation of turbulence/mixing and environmental controls

7.3.1 Surface Heating

The change in φ due to heat transfer at the sea surface may be written:

$$\left(\frac{\partial \varphi}{\partial t}\right)_{heat} = \frac{\alpha g}{2c_{\mathrm{p}}}\left\{Q_s' G(kh) - Q_u\right\}$$

where c_{p} is the heat capacity, α is the expansion coefficient, g is gravity and $Q'_s = Q_s(1-A)$ is the incoming short wave solar radiation immediately below the surface for an above surface flux of Qs and an albedo A. The term $Q_{\mathrm{u}} = Q_{\mathrm{e}} + Q_{\mathrm{b}} + Q_{\mathrm{c}}$ represents the sum of the upward heat flux due to evaporation, long wave back radiation and sensible heat transfer, respectively. The function *G*(kh) allows for the absorption profile of the solar radiation including the heat released when radiation reaches the bottom in shallow water, which needs to be taken into account in this case (see appendix in Wiles, van Duren *et al.*, 2006)

As an illustration of the stabilising effect of surface heating, if a typical summer daily averaged heating rate of $Q_{\mathrm{t}} = Q_{\mathrm{s}}'T - Q_{\mathrm{u}} = 160\ \mathrm{W\,m^{-2}}$ is considered along with values of $\alpha = 3\times10^{-4}\ \mathrm{K^{-1}}$ and $c_{\mathrm{p}} = 4000\ \mathrm{J\,kg^{-1}\,K^{-1}}$, then the contribution to the potential energy anomaly φ is $60 \times 10^{-6}\ \mathrm{W\,m^{-3}}$, which is the equivalent of about $5\ \mathrm{J\,m^{-3}}$ per day.

7.3.2 Horizontal density gradient

For a water column that is initially vertically mixed but exists within a horizontal density gradient $\frac{\partial \rho}{\partial x}$, density currents will tend to cause denser water to flow horizontally under lighter water to induce stratification (Simpson *et al.*, 1990). There is a density gradient existing between Sallingsund (~1020 kg $\mathrm{m^{-3}}$) and Aggersund (~1016 kg $\mathrm{m^{-3}}$) of $\frac{\partial \rho}{\partial x} = 1.8\times10^{-4}\ \mathrm{kg\,m^{-3}}$ (figure 7.6), therefore a northeast flow near the bed and a southwest flow near the surface might be expected (excluding rotational effects). As the ADCP currents show (figure 7.2), this was not observed at the observational site. This stratifying contribution has therefore been omitted from the analysis.

7.3.3 Tidal Stirring

The change in φ due to tidal stirring from the bed can be written as:

$$\left(\frac{\partial\varphi}{\partial t}\right)_{tide} = -\frac{4\psi\rho c_d u_0^3}{3\pi h}$$

where ψ=0.004 is the efficiency of tidal stirring, $c_d \approx 0.0025$ is the seabed drag coefficient and u_o is the depth averaged amplitude of the tidal velocities. If values of $u_o \approx 0.1$ m s^{-1}, ρ=1017 kg m^{-3} and h=7 m are used, this corresponds to a value of $\left(\frac{\partial\varphi}{\partial t}\right)_{tide} = 0.6\times10^{-6}$ W m^{-3} mixing power supplied by tidal stirring. It can therefore be assumed that the effects of tidal stirring are negligible compared to the heating term and other processes.

7.3.4 Wind Stirring

The reduction in φ due to wind stirring at the surface in the shelf sea model is given by

$$\left(\frac{\partial\varphi}{\partial t}\right)_{\mathrm{wind}} = -\delta C_{\mathrm{d}}\gamma\rho_{\mathrm{a}}\frac{W^3}{h}$$

where $C_d \approx 2\times10^{-3}$ is the drag coefficient, $\gamma \approx 0.03$ is the ratio of surface current speed to wind speed W and ρ_a=1.24 kg m^{-3} is the air density at the sea-air interface. If a previously accepted value for the wind mixing efficiency in shelf seas of $\delta = 0.023$ (Simpson *et al.*, 1981) and a windspeed of W=5 m s^{-1} is taken, the reduction in φ due to wind stirring is of the order 30 × 10^{-6} W m^{-3}.

In the present case, where the density gradients are relatively close to the surface, wave motions are expected to play a larger part in the buoyancy flux than in the shelf sea situation where the pycnocline is typicaly at a depth of 20 - 40 m. Another term that explicitly accounts for mixing by surface waves has therefore been included. The wind speed cannot be used as a proxy for significant wave height as discussed above because winds blowing from different directions have different fetches and are thus associated with different wave conditions (figure 5.1 and figure

7.6a,b). Because wind and waves are considered separately, the wind mixing efficiency δ will take a different and as yet undetermined value from the above suggested 0.023. This becomes the first tuneable parameter in our model.

7.3.5 Wave Stirring

The typical wave period observed in this part of Limfjorden is $T_w \approx 2.5$ s which implies a wavelength $\lambda = gT^2/2\pi \approx 6\,\mathrm{m}$. Therefore the waves can reasonably be approximated as deep water waves in water of depth 7m. The rms orbital velocity |u| of waves is then given by

$$|u| = \sigma Amp = \frac{\pi SWH}{T_w}$$

where σ is the angular frequency, *Amp* is the wave amplitude and *SWH* is the significant wave height measured by the waverider buoy. If it is assumed that stirring due to the orbital motions is proportional to $|u|^3$ (Masch, 1963; Morales *et al.*, 1997), giving an input to stirring from waves of

$$\left(\frac{\partial \varphi}{\partial t}\right)_{waves} = -\eta\rho\frac{\pi^3}{h}\left(\frac{SWH}{T_w}\right)^3$$

where η is the efficiency of wave mixing. At this stage η is regarded as undetermined and is the second tuneable parameter of the model. The strongly non-linear input to mixing associated with wave steepening and breaking is represented in the cubic power of the significant wave height. Turbulence from steepening and breaking waves will be confined to the upper region of the water column where wave orbital motions are present.

7.4 Comparison of the model to the Data

The above estimates indicate that solar heating and wind/wave mixing will dominate over tidal stirring and estuarine circulation and will therefore be significant terms in the buoyancy-stirring competition. The equation for the evolution of φ will then take the form:

Equation 7.2
$$\frac{\mathrm{d}\varphi}{\mathrm{d}t} = \frac{\alpha g}{2c_\mathrm{p}}\{Q_s{}'T(kh) - Q_\mathrm{u}\} - \delta C_\mathrm{d}\gamma\rho_\mathrm{a}\frac{W^3}{h} - \eta\rho\frac{\pi^3}{h}\left(\frac{\mathrm{SWH}}{T}\right)^3$$

Forward integration in time of equation 7.2 allows us to predict whether the water column will be stratified or mixed solely from the meteorological forcing and wave conditions (Q, W, SWH and T). Values for these parameters were obtained from the meteorological station on Livø and the wave buoy.

The φ model was run for the period of observations using forcing data shown in figure 7.6. All coefficients in equation 7.1 were taken from established values except for the efficiency of wind mixing δ and wave mixing η which have been adjusted to give an optimum fit to the observations.

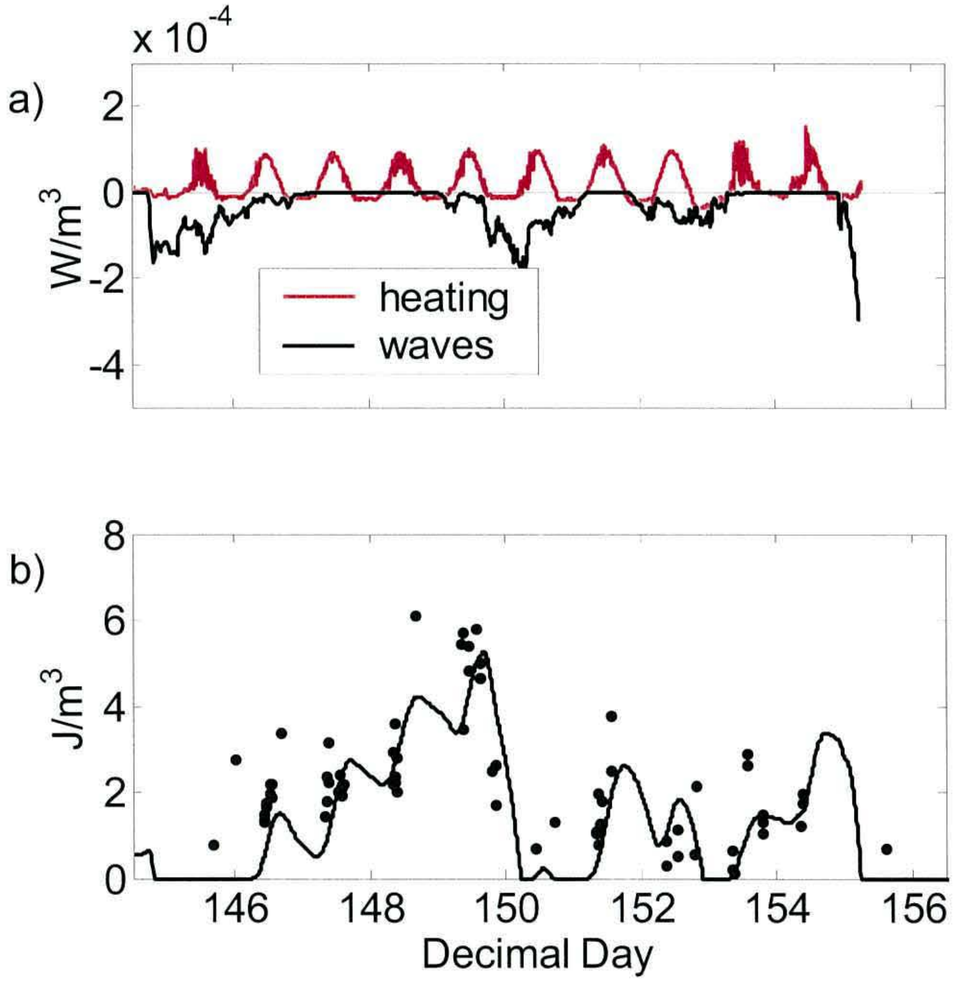

Figure 7.7. φ-simulation over the mussel site. a) The heating and wave mixing components contributing to the stratification of the water column from equation 7.2. The wave mixing term is tuned by setting $\eta = 4\times10^{-6}$. The wind mixing term disappears to zero because δ=0 give the best fit in equation 7.2. b) the value of φ obtained by cumulatively summing the inputs into equation 7.2 is given by the solid line. The dots are the individual values of φ calculated from each CTD cast.

Figure 7.7a breaks down each of the components in equation 7.2 to show the change in the potential energy anomaly φ due to surface heating and waves. The effect of wind has been omitted (see next paragraph). The diurnal heating and cooling cycle is evident, as are 3 strong mixing events due to wind-driven waves, and the start of a fourth mixing event at the end of the experimental period.

Equation 7.2 was evaluated, then $\mathrm{d}\varphi/\mathrm{d}t$ integrated in time to give an absolute value of φ (figure 7.7b). The two tuneable parameters in the model are the wind mixing efficiency, δ, and wave mixing efficiency η. The best fit was found when $\delta = 0$ and $\eta = 4\times10^{-6}$. The physical interpretation of this is that the mixing is not forced directly by wind stress, but rather by wind-driven waves. This is a different interpretation to previous applications of this model in deeper shelf seas, where wind and wave stirring can be considered together as a single input because the pycnocline is much deeper.

This reduced physics model is seen to give a fair account of the main features of the observed changes in water column stability. This includes the diurnal influence of solar heating during the day and convection due to surface cooling at night. These features can be seen in both the model line, and the values taken from the CTD casts (daytime only). The model shows the increase in water column stability during calm periods, and illustrates the dramatic decline in φ during strong mixing events. While it is reasonable to infer from the success of the model that it includes the dominant processes, it does not, however, account for all the changes in the vertical structure. For example there are clear indication of a dense water intrusion near the bed presumably in response to local horizontal density gradients (see figure 7.1, days 148-150 and days 153-155).

7.5 Summary and Discussion

The density structure, currents, waves and meteorological conditions in the Løgstør Bredning of Limfjorden were observed for a period of ten days during the summer season. Aspects of the mean and turbulent flow fields in Limfjorden have been observed using ADCP and ADV techniques. Currents away from the inflow and outflow boundaries were found to be generally weak with speeds < 0.1 m s^{-1}. During periods when the water column was stratified the flow frequently exhibited a two-layer structure with opposing flows in surface and near-bed layers. By contrast, at times of vertical homogeneity in density, flows were nearly uniform in the vertical.

Very little turbulence was generated in the bottom boundary layer and turbulence levels were generally low. Very close (2-3 cm) to the surface of a mussel patch, subtle elevations in levels of turbulence were detected that appeared not to be wave-driven. This turbulence could either be due to increased bottom roughness caused by the presence of mussels, or due to the filtering activity of the mussels themselves. The filtering effect of mussels on the water column has been shown to have an influence on the bottom boundary layer up to a height of several cm (van Duren *et al.*, 2005). The injection of heat at the bed due to solar radiation would also lead to a convective mixing layer at the bottom of the water column. These near bed TKE production mechanisms are unlikely to have an effect on food and oxygen supply to mussels in Limfjorden on the relevant scales. Information from local users (mussel farmers and researchers) indicate that during prolonged periods of calm, settled weather, entire ecosystems have been severely affected by anoxia and starvation. Drastic losses in harvest occurred during the 2006 due to a relatively stable, warm summer season.

The system switched between stratified and mixed conditions in direct response to meteorological forcing. It was postulated that the major process promoting stratification was heat exchange at the surface, and this was opposed by stirring due to wind acting through the wave field. This postulate has been tested through a simple reduced physics model, which represents water column stability in terms of the scalar parameter φ. The model follows the approach of Simpson *et al.*, 1981) but with a modified representation of the wave stirring term and surface heating which allows for the shallow depth of Limfjorden. The solar heating term was adjusted to allow for light penetration to the sea bed, which is not a factor in shelf seas.

In terms of the physical driving forces, there is little difference between the mussel and sand sites. As the energy driving vertical turbulent diffusion is from the surface wind, the presence of mussels has no effect on the diffusion rates. The lack of turbulence during calm periods allowed formation of a concentration boundary layer over the mussel site, which was observed by the biology partners of MaBenE.

8 Oosterschelde:

The field campaign in the Oosterschelde was designed to investigate the effect of mussel beds on the hydrodynamics of the overlying water column and the associated vertical fluxes of phytoplankton and nutrients. Two constrasting sites were again chosen, an area of extensive commercial mussel culture and an area of bare sand. The two sites were chosen so as to be identical except for mussel coverage. In reality, this was very difficult to achieve due to the natural variation of water depths and velocities in the Oosterschelde and granting of permission to occupy the sites by local mussel farmers.

8.1 ADCP Results

8.1.1 Stability

As discussed in section 3.5, the accuracy of the variance method depends on how accurately the ADCP is levelled. The strategy employed during this campaign was for divers to embed the ADCP within the sediment and to accurately level the instrument. This placed the height of the first ADCP bin at 0.5 m above the bed.

During the first deployment over the mussel site, the ADCP tilted due to rapid bed erosion during strong currents. The tilt introduced a significant error to the Reynolds stress estimates made using the variance method. Divers re-levelled the ADCP on May 6th. The ADCP was recovered on May 7th for data downloading and battery replacement then redeployed for a second deployment (with additional bracing) on May 8th. Divers levelled the ADCP on May 9th, and the ADCP eventually settled to a position where the orientation was 1° and 1.6° in the pitch and roll directions respectively. Beam 3 was oriented towards 300°, and therefore the ADCP was tilted at 1.6° from vertical in a direction aligned with the flood tide.

The initial approach at the sand site was also to embed the ADCP within the sediment. However the ADCP did not sit securely in the sand, and was completely scoured out during the first deployment. The ADCP was redeployed on May 8th in a secure aluminium bed frame, which lifted the first measuring bin of the ADCP to 1.3 metres above the bed.

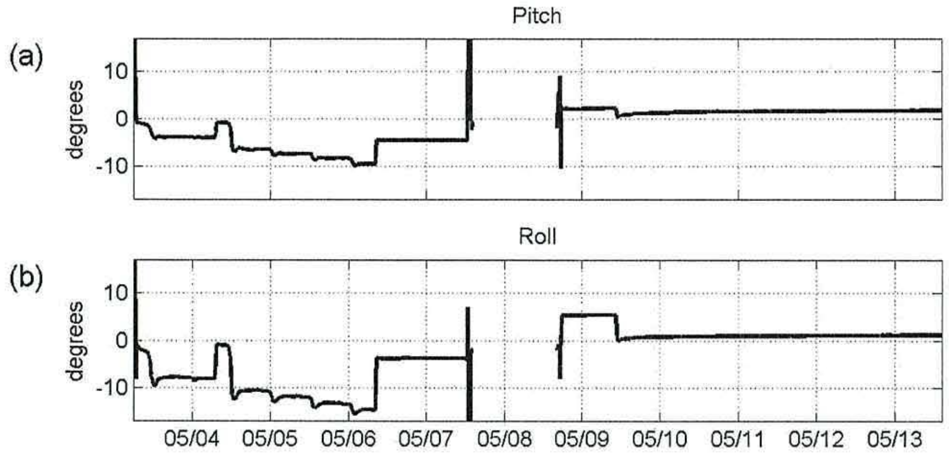

Figure 8.1. The pitch and roll of the ADCP at the mussel site. Positive pitch (roll) indicates beam 3 is higher than beam 4 (beam 2 is higher than beam 1). See figure 3.1 for a diagram of the ADCP beam orientation.

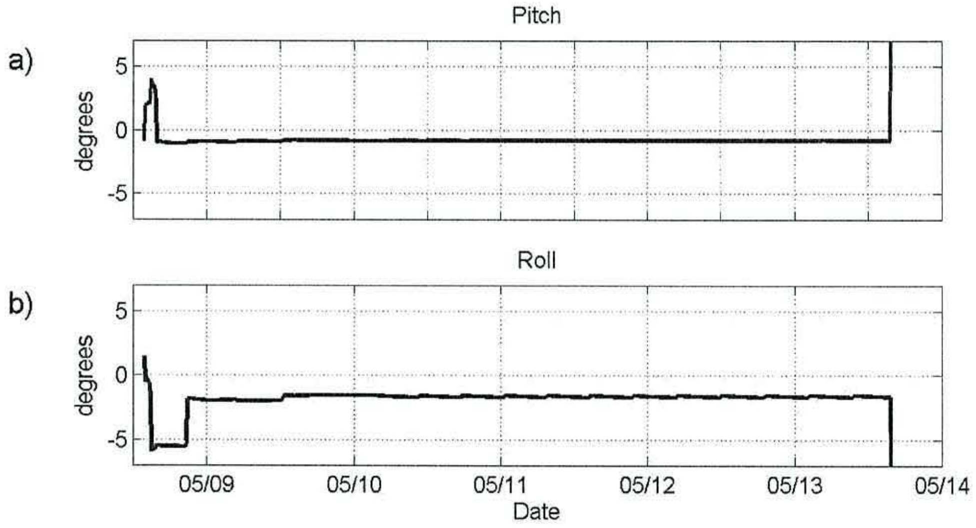

Figure 8.2. (a) Pitch and (b) roll of the ADCP over the sand site during the second deployment. . Positive pitch (roll) indicates beam 3 is higher than beam 4 (beam 2 is higher than beam 1).

The stability of the ADCP during the second deployment is shown in figure 8.2. Divers relevelled the ADCP on the afternoon of May 8th. After levelling, the ADCP was level to within 0.8° and 1.6° in the pitch and roll attitudes respectively (see figure 3.1) Given the 3rd beam of the ADCP was oriented at 40° from north, the flood tide was aligned with beams 1 and 2. The tilt of the ADCP against the direction of the flood tide was 1.6°.

The tilt of the ADCPs will affect the stress estimates and hence the seabed drag estimates. A tilt into the flow will increase the stress estimates, whereas a tilt away from the flow will decrease the stress estimates. Hence when calculating the seabed drag coefficient over both the flood and ebb cycles, they should balance out.

8.1.2 Velocities

The along and across stream velocities over the mussel site (figure 8.3 and figure 8.4) vary by a factor of 2.1 over the springs-neaps cycle (springs on May 6th and neaps on May 12th). The tide is rectilinear, but is not a simple M2 flow. There are 2 peaks in velocities on the flood tide and a less pronounced 'shoulder' after the maximum velocity on the ebb tide. The strong deceleration after the peaks in flow coincides with the water level rising above the main channel and flooding the intertidal sand banks. The first velocity maximum is shorter and weaker than the second velocity maximum on the flood tide. Slack water is short lived at both high and low tide. During springs, the flow reaches a maximum of ~ 0.9 m s^{-1} on the flood tide and ~ 0.5 m s^{-1} on the ebb tide. The across stream velocities are much smaller (~ 0.1 m s^{-1}) than the along stream velocities, but not negligible. The presence of a lateral secondary flow is not surprising given the complicated local topography (see figure 5.3)

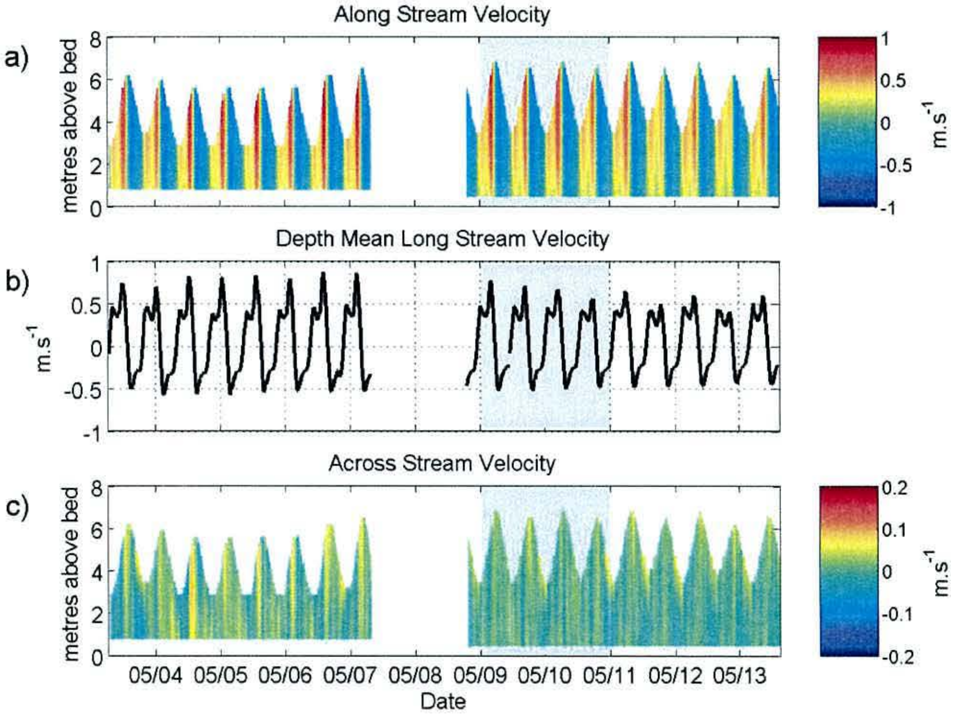

Figure 8.3 The 10 minute averaged velocities above the mussel bed. Coordinates have been rotated into along stream (towards 127°) and across stream velocities. a) Along stream velocities,

b) depth mean along stream velocities and c) across stream velocities. The ADCP was recovered for data downloading and battery replacement on May 7th-8th. Note that the across stream velocities are on a different colour scale. The shaded region is blown up in figure 8.4.

The velocities at the sand site (figure 8.5) are similar to the velocities at the mussel site. The flood tide is stronger than the ebb tide, reaching a maximum of 0.9 m s^{-1} during the deployment. There are 2 maxima on the flood tide. The first peak occurs 1hr 40mins after low water slack and the second peak 2 hrs before high water slack. The ebb tide is shorter and weaker (max 0.5m/s) than the flood tide.

Comparison of velocities at the two sites show only small differences (figure 8.6). The first peak occurs slightly later over the sand site. The velocities on the flood tide are slightly larger over the sand site. The second peak (at 0500), slack water (at around 0630) and maximum ebb flow (at around 0800) are also delayed over the sand site by about 20 minutes. The velocities on the ebb tide are slightly larger over the mussel site.

These differences are highlighted in figure 8.7. Velocities are higher over the sand site on the flood tide and higher over the mussel site on the ebb tide. The slight lead in phase over the mussel bed opens out an eccentric ellipse in the velocity comparison.

At peak flood flow, the velocities are significantly higher over the sand site, however shear is stronger over the mussel site (figure 8.8). During peak ebb flow, the velocities over the sand site are stronger near the surface, however the shear is also stronger over the mussel site.

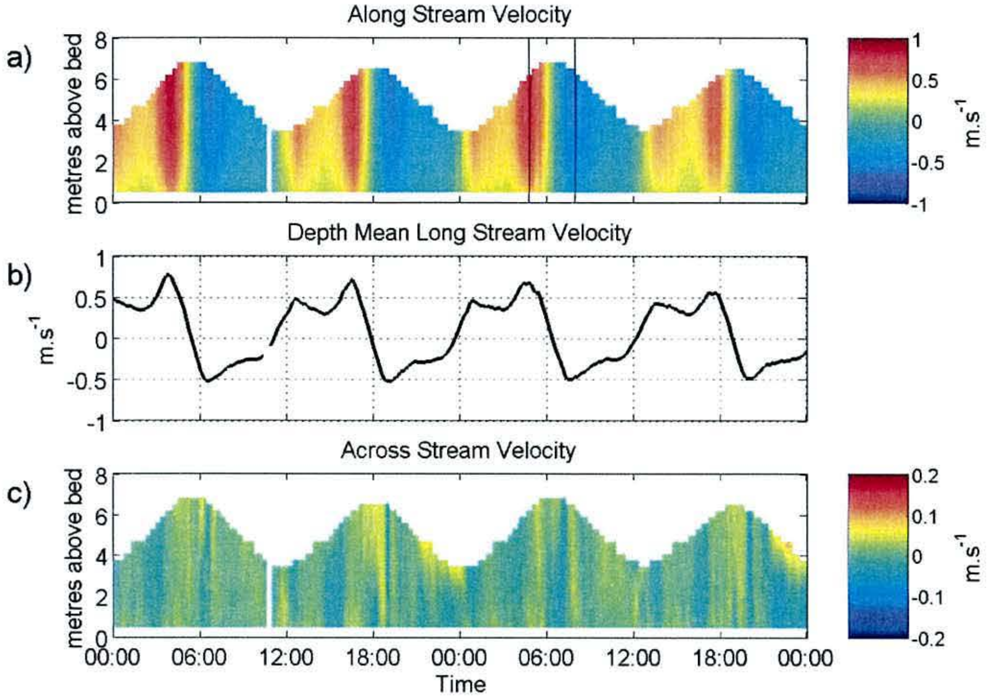

Figure 8.4. Along and across stream velocities above the mussel site focussed on 9th-10th May 2004. (a) along stream velocities, (b) depth mean along stream velocities and (c) across stream velocities. The vertical lines in (a) indicate the time used for the profiles shown in figure 8.8.

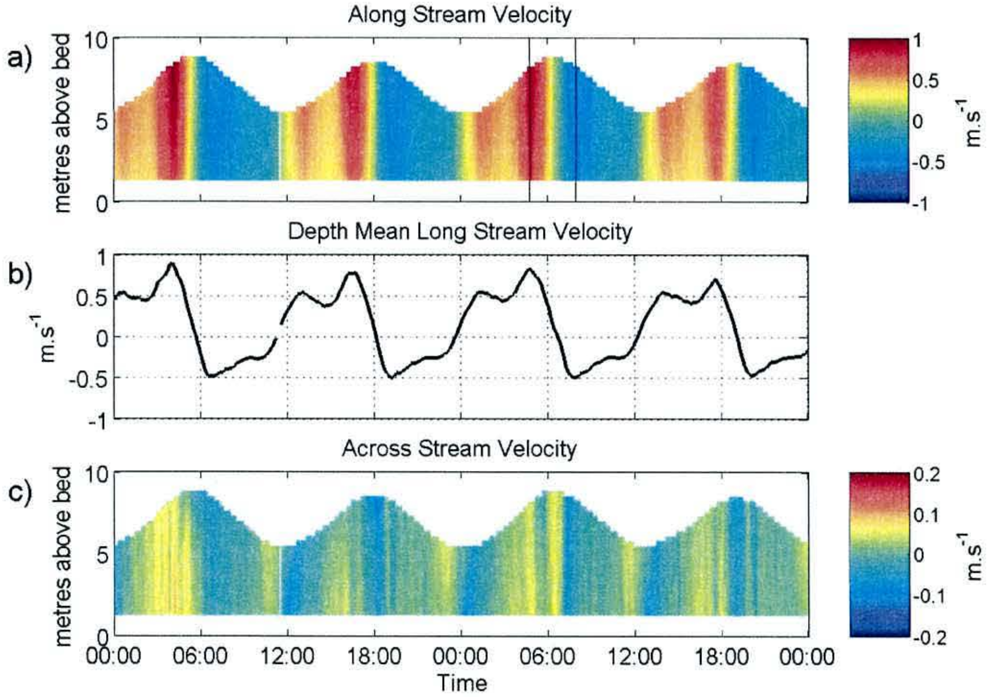

Figure 8.5. Velocities above the sand site over the 9th-10th May. (a) along stream velocities (towards 127°), (b) depth mean along stream velocities and (c) across stream velocities. The vertical lines in (a) indicate the time used for the profiles shown in figure 8.8.

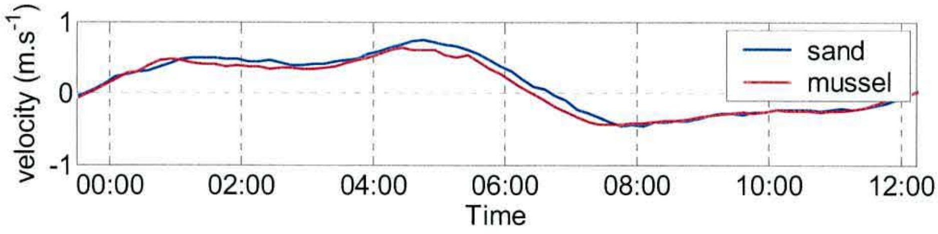

Figure 8.6. Velocities at 2 m above the bed over the mussel (blue) and sand (red) site on May 10th.

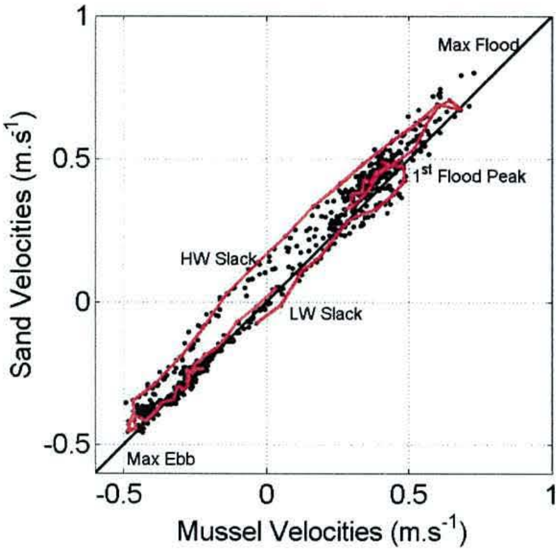

Figure 8.7. 10 minute averaged sand velocities vs mussel velocities at 2 m above the bed. The red line traces the evolution of the velocities on the afternoon-evening of May 9th. The ellipse moves in an anti-clockwise direction. The black line indicates a 1:1 relationship. The phases of the tide are written on the axis.

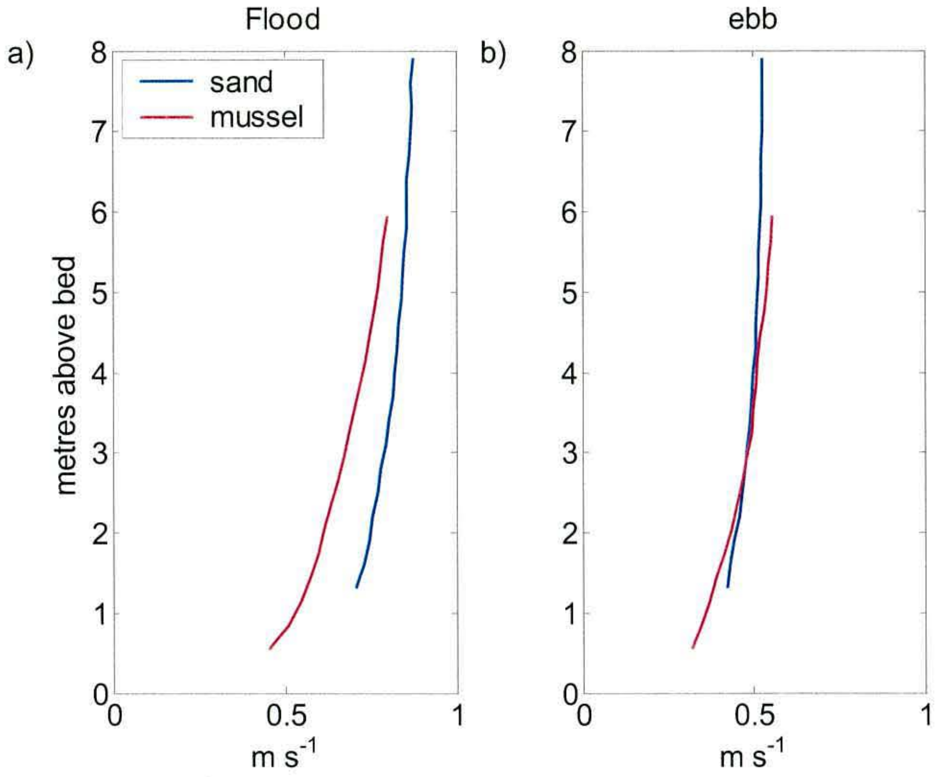

Figure 8.8. Velocity profiles over sand and mussels during (a) the flood tide (May 10th 0445) and (b) the ebb tide (May 10th 0755).

8.1.3 Stresses

The Reynolds stresses over the mussel site (figure 8.9a) are considerably stronger on the flood tide (up to 1.5 N m^{-2} during springs) than on the ebb tide (maximum of 0.5 N m^{-2} during springs). The two peaks evident in the flood velocities (section 8.1.2) are also observed in the flood stresses. The strongest stresses are found near the bed and decrease towards zero at the surface. There appears to be a decrease in the stresses in the bottom few bins over the mussel site, which has also been observed in previous datasets (Rippeth *et al.*, 2002). Negative stresses during positive flow are consistent with the seabed exerting a retarding force on the water column.

The Reynolds stresses over sand (figure 8.9b) are smaller than over mussels. The time evolution is similar, exhibiting a double peak on the flood tide. The first peak has a value of 0.7 Pa and the second peak has a value of 1 Pa during springs. The stresses on the ebb tide are much smaller, with values of 0.3 N.m^{-2} during springs.

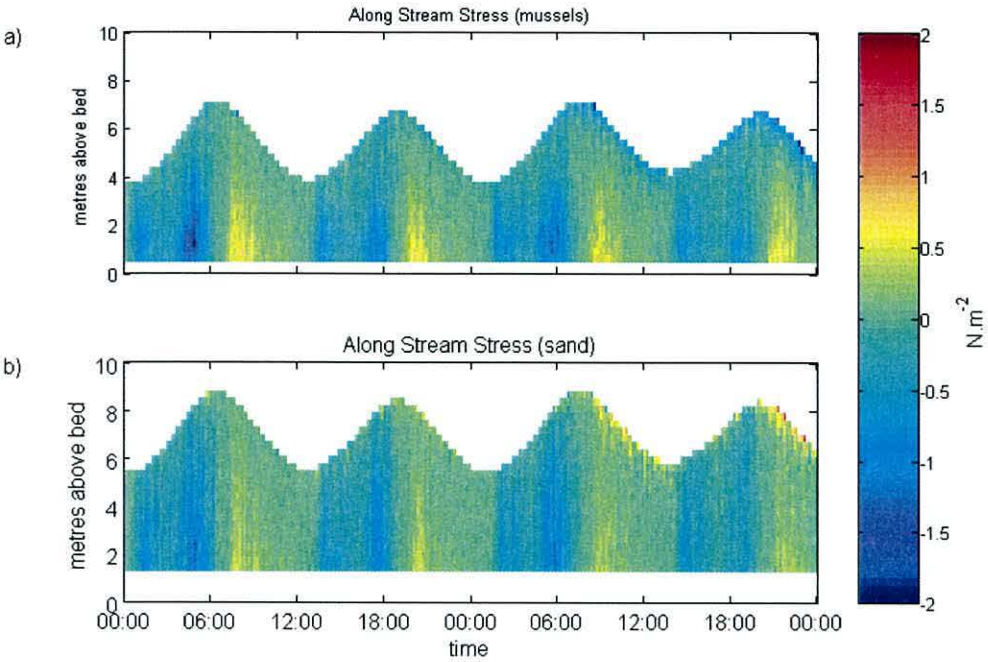

Figure 8.9. a) Along stream stresses at the mussel site. b). Along stream stresses at the sand site. (a 10 minute averaging period was used for the calculation). The plot is over the time period 9th-10th May 2004.

A comparison of the Reynolds stresses above the mussel and sand site (figure 8.10) shows the magnitude of the stresses track well over the two sites. The delay observed in the velocities is also observed in the stresses, however due to the relatively higher noise this is less obvious.

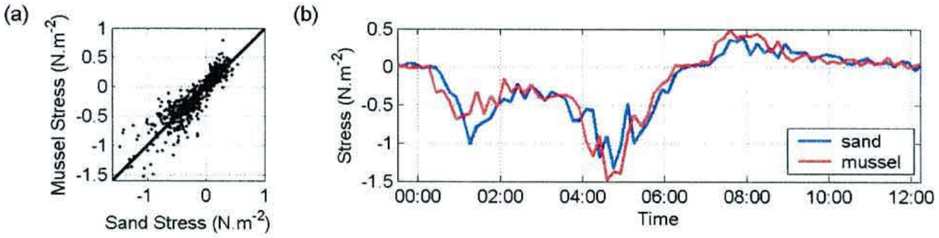

Figure 8.10. Comparison of the Reynolds stresses at 2 metres above bed at the mussel and sand sites. (a) Plot of stress above the mussel bed vs stress above the sand site over the second deployment period. (b) Time plot of stress over the mussel and stress over sand on the morning of May 10th 2004.

8.1.4 Stress vs Shear comparison

A comparison of stress and shear (figure 8.11) gives an indication of the reliability of the Reynolds stress measurements. We expect production P and eddy viscosity N_z both to be positive; negative P and N_z would imply the unlikely scenario of energy being transferred from turbulence to themean flow. Since $N_z = \frac{-\tau}{\rho \frac{\partial u}{\partial z}}$, positive N_z requires that τ and $\frac{\partial u}{\partial z}$ have opposite signs so that in a plot of τversus $\frac{\partial u}{\partial z}$ the data should lie in the second and fourth quadrants.

Most of the data points in figure 8.11 and figure 8.12 do fall in the expected secpond and fourth quadrants. As the shear goes towards zero, the residual noise (twice the rms) in the stress drops to a level of ~ 0.1 Pa. The ratio of the stress to the shear is a measure of N_z . Inspection of the slope of the scatter plots with respect to height shows that N_z has a maximum at midwater.

In the TKE P and ε estimates below, data where the shear and stress are in the first and third quadrants are taken as unreliable and the data is masked from the plots.

8.1.5 Bottom Drag Coefficient

Estimates of the drag coefficient are calculated from the ratio of the square of the velocity at 2m ($\overline{u(200)}^2$) to the extrapolated bed shear stress (τ_b), i.e. the quadratic drag law. The estimate of the drag coefficient at the mussel site ($C_{200} = 0.0032 \pm 0.0003$, see figure 8.13a) is significantly different to the estimate at the sand site ($C_{200} = 0.0026 \pm 0.0003$ see figure 8.13b). These values are comparable with values found in other literature (Chriss *et al.*, 1982 and Soulsby, 1983).

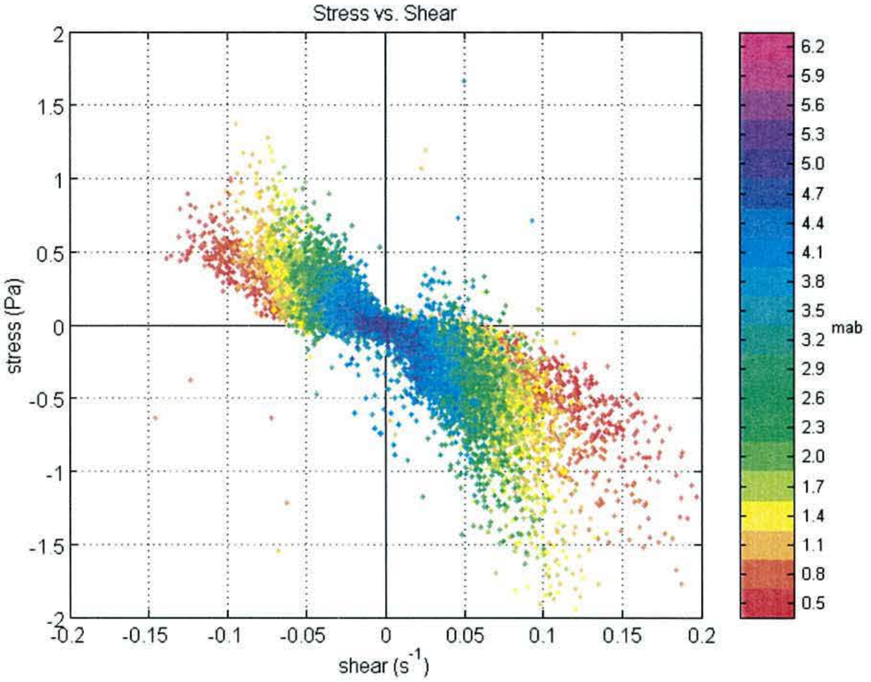

Figure 8.11. Reynolds stress plotted against shear for each height bin at the mussel site. The colour of the dots indicate how far above bed the comparisons are made.

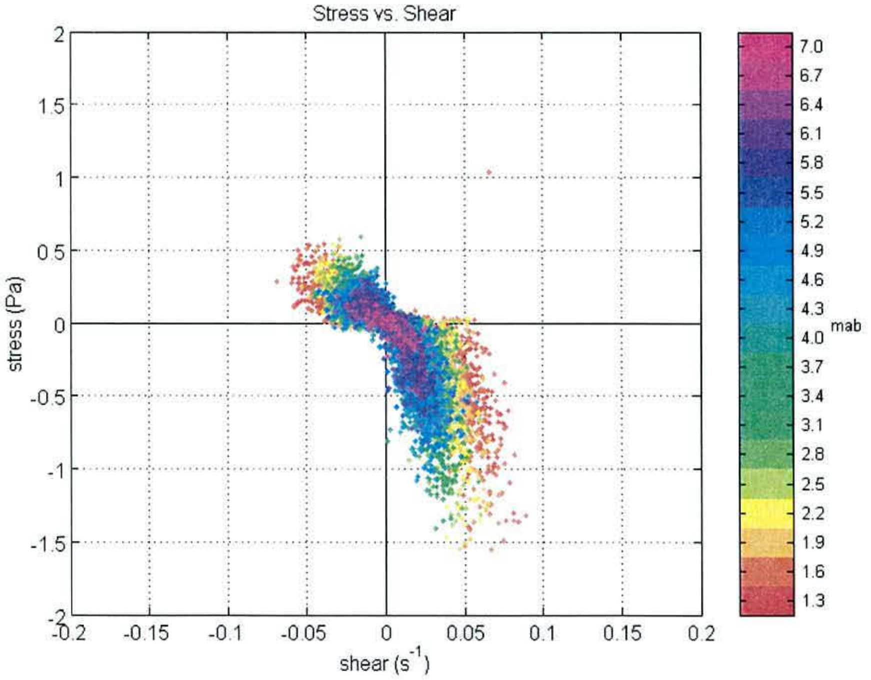

Figure 8.12. Reynolds stress plotted against shear for each height bin at the sand site. The colour of the dots indicates how far above bed the comparison is made.

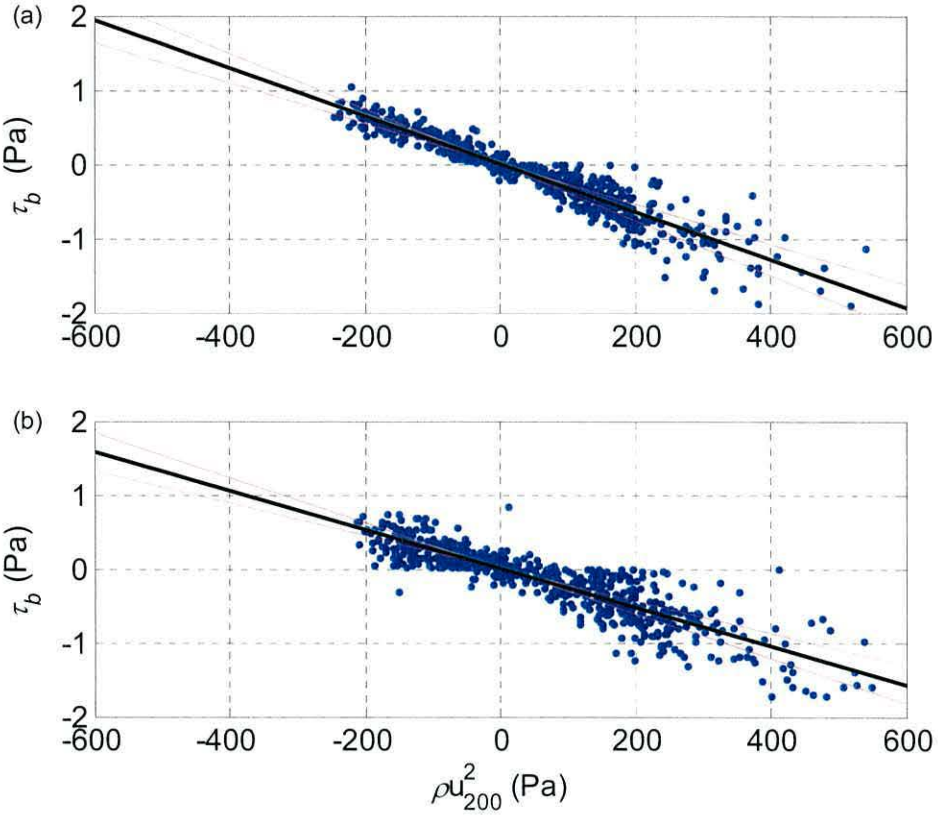

Figure 8.13. Bed shear stress τ_b plotted against ρU_{200}^2 (.). The slope of the black line gives the seabed drag coefficient via the quadratic drag law. The red lines either side are the 95% (2×std deviation) confidence interval error lines. (a) At the mussel site (C_{200} = 0.0032±0.0003) and (b) at the sand site (C_{200} = 0.0026±0.0002)

8.1.6 Turbulent Kinetic Energy Production Rates

The TKE Production rate estimates over the mussel bed (figure 8.14a) also reflect the two maxima on the flood tide. The first peak occurs 1 hour after low water slack, has a magnitude of 0.1 W m^{-3} and lasts for about 50 minutes. The second maximum is 5 hours after low water slack, is twice as strong (0.2 W m^{-3}) and lasts twice as long (~100 minutes) as the first peak. The TKE Production rate on the ebb tide is weaker (maximum of 0.02 W m^{-3}) and does not exhibit a double maxima.

The time development of *P* over the sand site (figure 8.14b) is similar to the mussel site, however the estimates of *P* are significantly lower. The maximum value of TKE Production is ~1 W m^{-3}. Because the ADCP's lowest bin is at 1.34 metres above the bed, the region of maximum TKE Production near the bed is not captured.

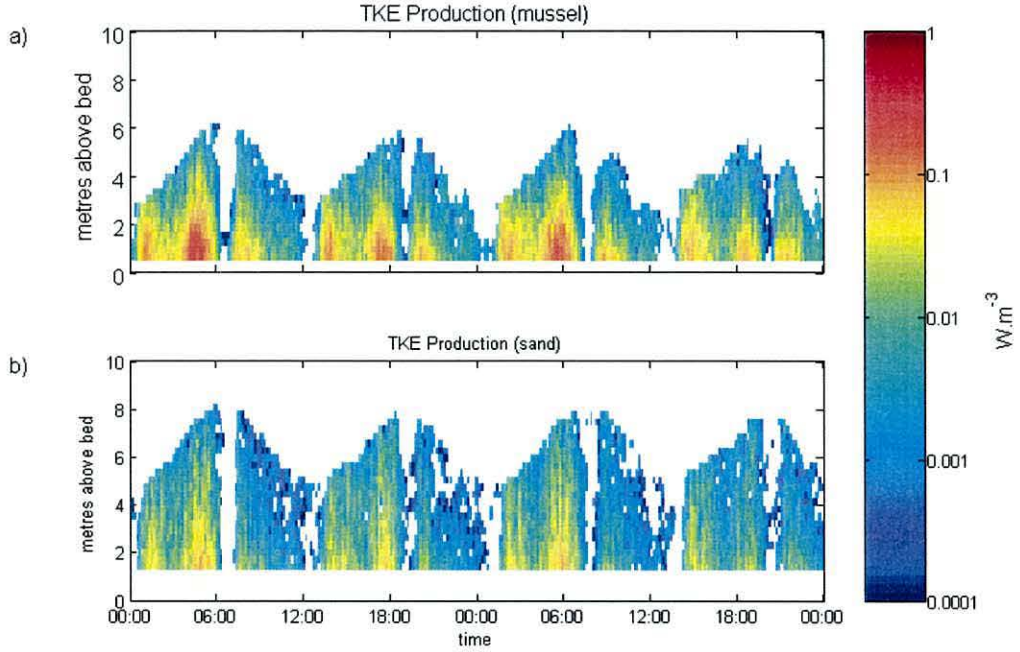

Figure 8.14 TKE Production rate, the white patches are where the data become unreliable as the production rates go negative. The time scale is hours on the 9th and 10th of May 2004.

The TKE Production rates over the mussel and sand sites track each other well (figure 8.15). The values at 2 metres above the bed are higher over the mussel site by up to a factor of two.

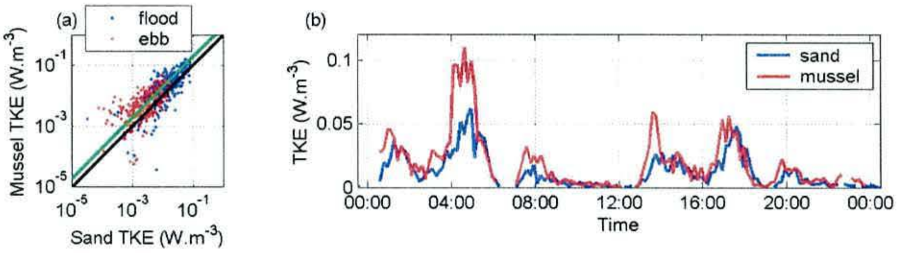

Figure 8.15. The TKE Production rates over the mussel and sand site at 2 mab. (a) The 10 minute averaged production rates plotted against each other. Blue dots are the flood tide and red dots are the ebb tide. The black line indicates a ratio of 1:1, the green line indicates a ratio of 2:1 (mussel TKE Production values higher). (b) a temporal comparison of the TKE production rates. The time scale is in hours on May 10th.

8.1.7 Turbulent Dissipation Rates

The turbulent dissipation rates (ε) estimated by the structure function method over the mussel site (figure 8.16a) are similar to P measured using the variance method, however the absolute values are higher. The structure function estimates miss the high dissipation region near the bed, hence the dissipation estimates visually appear lower. Over mussels, the ratio of $\varepsilon_{SF}/P = 1.74 \pm .03$.

Similarly, ε estimates over sand (figure 8.16b) track the P (see figure 8.14) estimates well. The structure function algorithm does have a larger blanking interval near the bed, and hence misses more of the high dissipation region. Over sand, the ratio of $\varepsilon_{SF}/P = 2.18 \pm .05$.

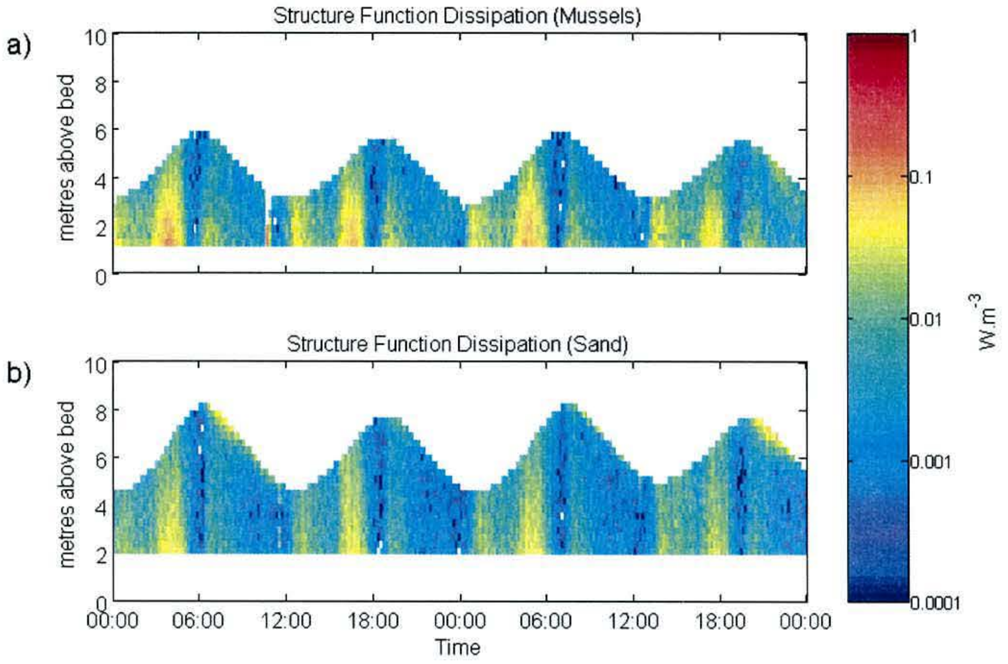

Figure 8.16. Dissipation rates measured by the structure function method. The white patches are where the data was unreliable because of a poor signal:noise ratio. The time scale is hours on the 9th and 10th of May 2004. (a) At the mussel bed and (b) at the sand site.

8.1.8 Turbulent Diffusion Coefficient

The maximum eddy viscosity (N_z) measured by the ADCP over mussels (figure 8.17) is 2×10^{-2} m^2 s^{-1}, during maximum flood flow. The lowest measurable eddy viscosities are 10^{-3} m^2 s^{-1} (the low noise threshold is determined by the data in the negative quadrants in section 8.1.4). Temporally, two maxima in N_z are observed on the flood tide and a single maximum is observed on the ebb tide, each coinciding with a peak in the flood velocities. N_z was lower during the ebb.

Maximum values of N_z are found in mid-water, agreeing with the theoretical hyperbolic vertical structure of eddy viscosity (Rippeth *et al.*, 2002); the nearbed region is not, however, captured. At slack water, estimates of eddy viscosity go towards zero. At the same time, estimates of both Reynolds stress and shear tend to zero, hence estimates of N_z (see section 3.4.2) become undefined (see section 8.1.4). The data has been masked by white at these times.

Estimates of N_z over the sand site were generally larger (figure 8.17). They ranged from a minimum detectable value of 10^{-3} m^2 s^{-1} to a maximum reliable value of 5×10^{-2} m^2 s^{-1}. The maximum value of eddy viscosity was again generally found in mid-water.

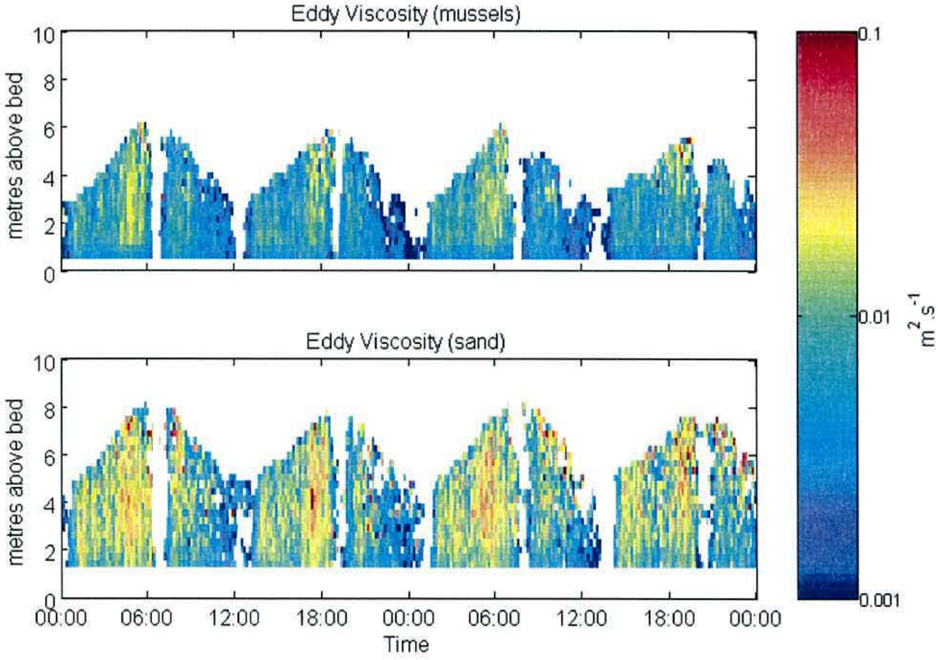

Figure 8.17. Eddy viscosity over the mussel and sand bed. The white patches are where the data became unreliable. The time scale is hours on the 9th and 10th of May 2004.

Non dimensionalised profiles of eddy viscosity values ($N_{z\,\mathrm{nondim}} = \dfrac{N_z}{hu_*}$ see Rippeth *et al.*, 2002) follow a hyperbolic shape (figure 8.18). Values of $N_{z\,\mathrm{nondim}}$ were higher over the sand site (average midwater value of ~ 0.18) than over the mussel bed (average midwater value of ~ 0.1).

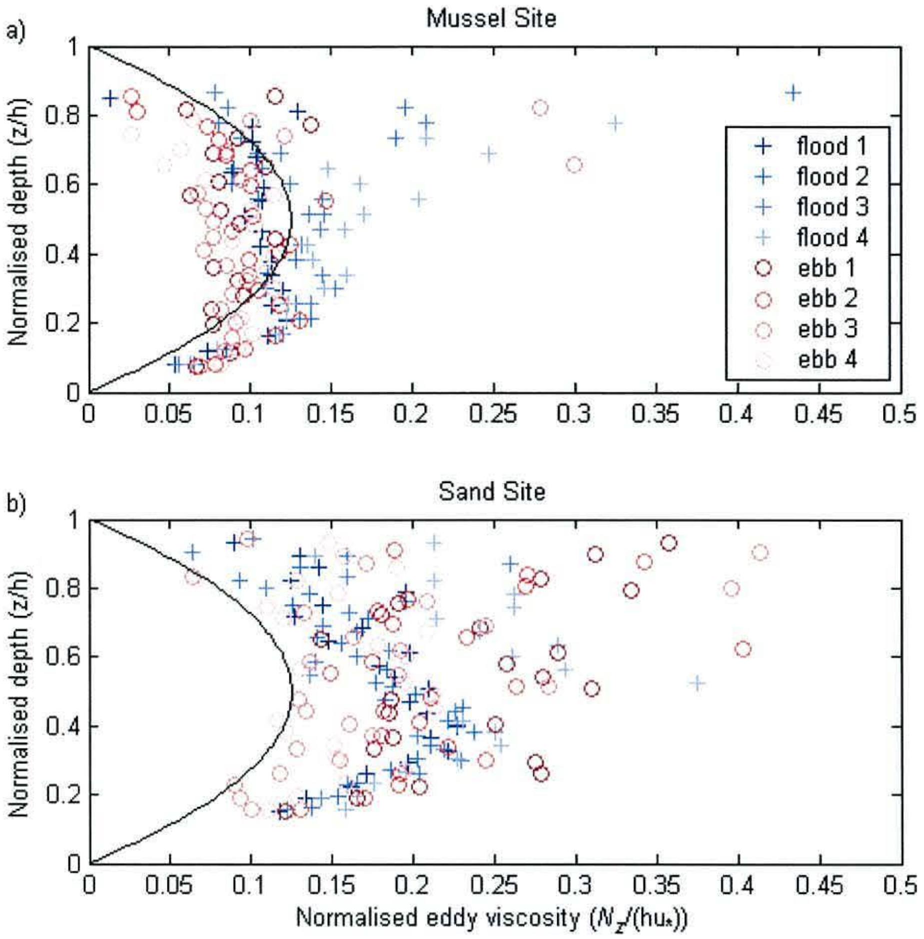

Figure 8.18. Non-dimensionalised estimates of N_z (60 minute averages) at peak flood and ebb times over (a) the mussel site and (b) the sand site. The blue crosses are on the flood tide and the red circles are on the ebb tide. The floods and ebbs are shaded in order from 1-4 (the numbers count M_2 cycles starting on May 7th). The black line indicates the ideal non-dimensionalised profile.

8.1.9 Mixing Time Scale

A mixing time scale describing the time taken for a point dump of tracer to be mixed vertically through the water column can be defined as

Equation 8.1 $$T_{mixing} = \frac{h^2}{\pi^2 N_z}$$

The evolution of this time scale over the tidal cycle (figure 8.19) is estimated using a midwater value for N_z over both the mussel and sand site. This mixing time scale is relevant to the erosion of a benthic phytoplankton depletion layer (which can be formed at slack water).

During the flood tide the mixing timescale over both mussels and sand is ~ 5 minutes. Although the TKE Production and eddy viscosity are lower on the first peak compared with the second peak on the flood tide (figure 8.14 and 8.18), the first peak in the flood tide is characterised by a slightly shorter mixing time scale due to shallower water at this time.

During the ebb tide, the mixing time scale was of the order of 10 minutes and was sustained over a shorter period of time (~ 3 hours).

Towards slack water, the mixing time scale over both the mussels and sand becomes much longer (4+ hours). Due to the increased noise in the denominator N_z in equation 8.1, the estimation of the mixing time scale becomes extremely noisy, hence the large scatter of data points around slack water. A long mixing timescale at slack water inhibits the vertical supply of phytoplankton to the benthic mussels, allowing the growth of a depletion boundary layer.

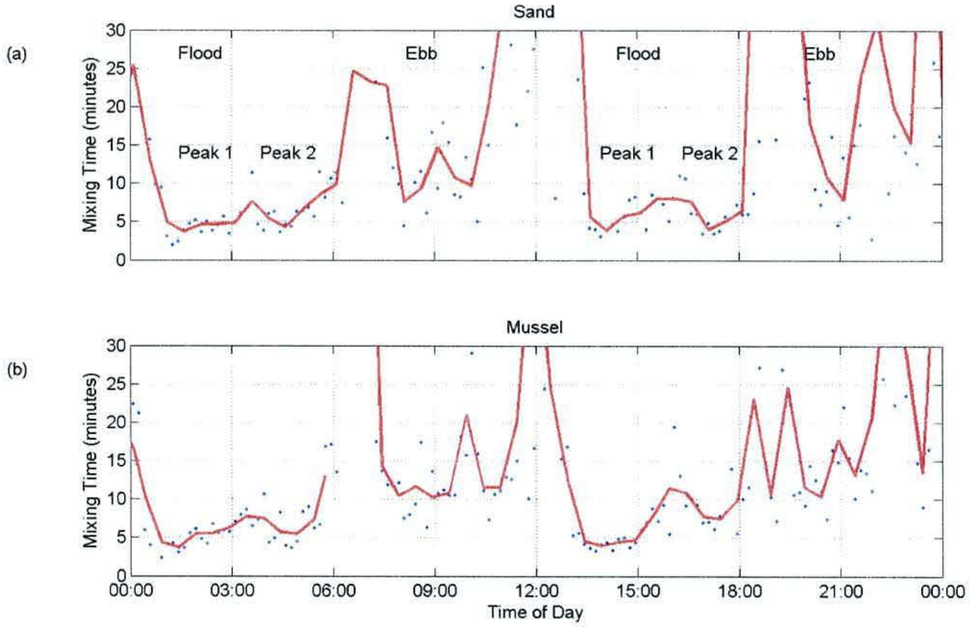

Figure 8.19. Mixing time scales estimated over (a) the Sand site and (b) the mussel bed on May 10th. The blue dots are 10 minute estimates of the mixing time scale. The red line is a low pass filtered form of the data.

8.1.10 Log-Profile fits.

Estimates of z_0 at the mussel site were obtained by fitting velocity data to the log profile (figure 8.20) and a mean of 0.022 ± 0.002 m was calculated using a bootstrap resampling technique. Substituting this into equation 3.21 (using a value of z =2m) gives a drag coefficient of 0.0079 ± 0.0004 m over mussels.

u_* ranged from .02 m s^{-1} to .07 m s^{-1} at the mussel site. Values for u_* estimated using the log method were higher compared with u_* estimated from the variance method. The ratio of the two was 0.64 ± 0.02, and hence the ratio between the calculated bed stresses (and hence drag coefficients – see section 8.1.5) was 0.41 ± 0.02.

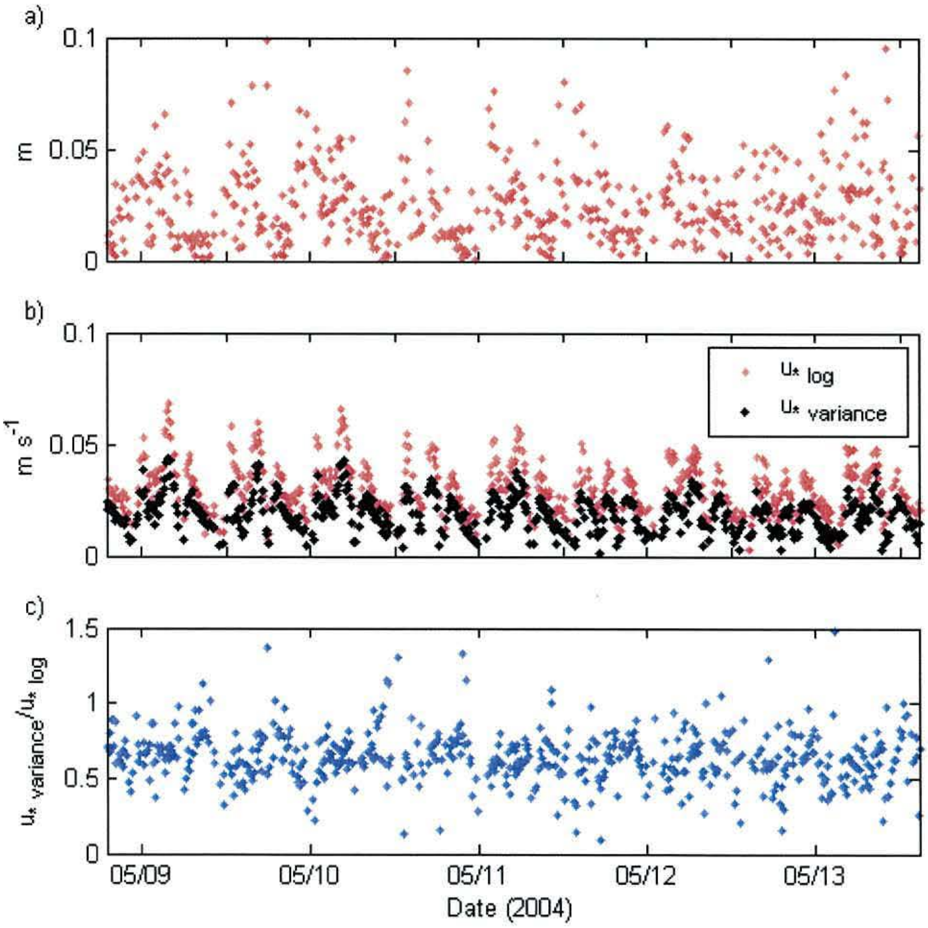

Figure 8.20. Results from log profile fit to data at the mussel site. a) z_0 , b) u_* estimated from log profile fits and u_* estimated by extrapolating the stress estimated via the variance method to the bed. c) The ratio of u_* from the variance method : u_* from the log method.

Similarly, estimates of z_0 over sand (figure 8.21) had a value of 0.0053 ± 0.0013, giving a comparable C_{200} of 0.0045 ± 0.0004.

Estimates of u_* from the log profile method ranged from .02 to .05 m s^{-1} at the sand site. u_* from the variance method consistently gave a lower value for u_* by a factor of 0.742 ± 0.034 (and therefore a ratio of $\tau_{\text{bed (variance)}}/\tau_{\text{bed (logprofile)}} = 0.55 \pm 0.03$).

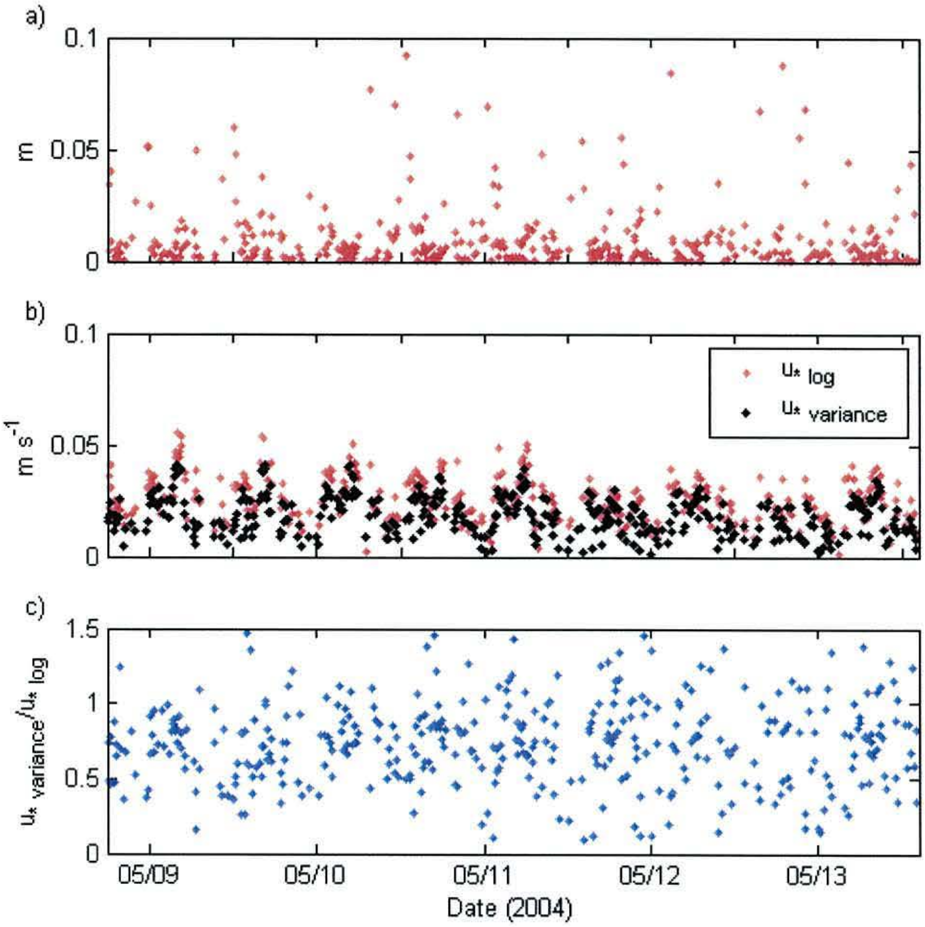

Figure 8.21. Results of log fit over sand site. a) z_0 b) u_* from the log profile (red) and the variance method (black) and c) the ratio of u_* estimated via the variance method : u_* estimated using the log profile fit.

The ratio of u_* over sand : u_* over mussels using a log approach is 0.83 ± 0.03 (figure 8.22).

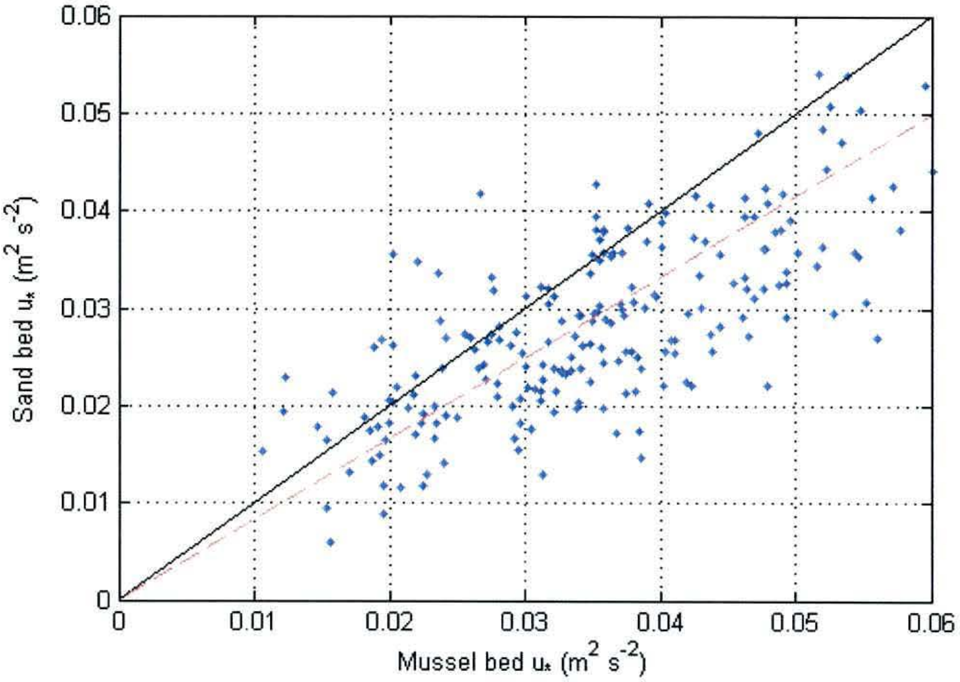

Figure 8.22 Ratio of u_* estimated using the log profile over the sand site and over the mussel site. The black line shows a 1:1 relation, while the red line is the line of best fit, which has a slope of 0.83±0.03.

8.1.11 Validity of log-profile fits

The validity of the log profile method at these sites is questionable. Von Karman's original 'law of the wall' hypothesis relies on the assumption that the shear in the water column depends only on the friction at the boundary and distance from the wall. Dimensional analysis gives

Equation 8.2 $$\frac{\partial u}{\partial z} = \frac{u_*}{\kappa z}$$

Therefore, $\kappa z \frac{\partial u}{\partial z}$ $(= u_*)$ should be constant with respect to height above bed, however the data indicates that this assumption was not well-founded in these datasets (figure 8.23). There appears to be a decrease in u_* near the bed at both the mussel bed and the sand site. The lower bins of the mussel site ADCP show a region where u_* drops markedly below 1.5 mab, unfortunately, the sand ADCP does not capture this region. Further away from the bed the signal to noise ratio obscures any trend, although the mussel site shows a decrease in u_* in the upper third of the water column.

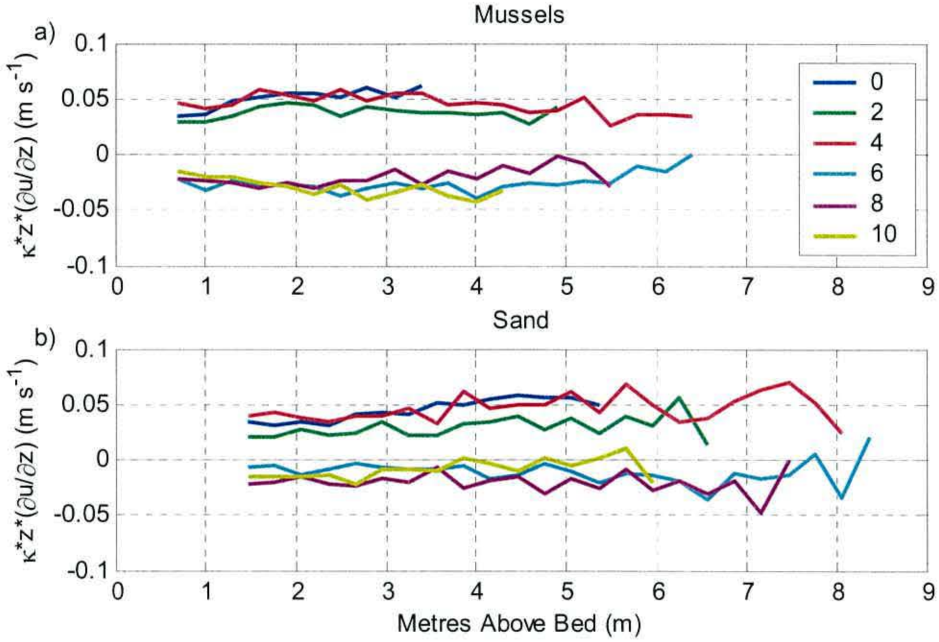

Figure 8.23. Plots of $\kappa z \frac{\partial u}{\partial z}$ (averaged over an hour) over the (a) the mussel site and (b) the sand site. The colours of the lines indicate the stage of the tidal cycle in hours from profile 0 (the start of the flood tide at 0100 on the morning of May 10th).

8.2 ADV Results

The mean velocities estimated from the ADV over the mussel site (figure 8.24a) are slower than the velocities over the sand site, despite the mussel deployment being closer to spring tides. Velocities from the ADCP extrapolated to 7 cm above the bed (figure 8.24a) using a log profile track well over the sand site, but not over the mussel bed. The varied nature of the mussel bed give rise to the likelihood that the ADV suffered from 'flow-blocking' during various stages of the tide, for example, it appears as if there is no reverse flow over the mussel bed.

The absolute turbulent kinetic intensity values at 7 cm above the bed are significantly larger over the sand site than over the mussel bed (figure 8.24b), however the normalised TKE intensities (= [modulus of velocity standard deviations] ÷ [modulus of mean velocity components]) are much higher over the mussel bed than over sand (figure 8.24c).

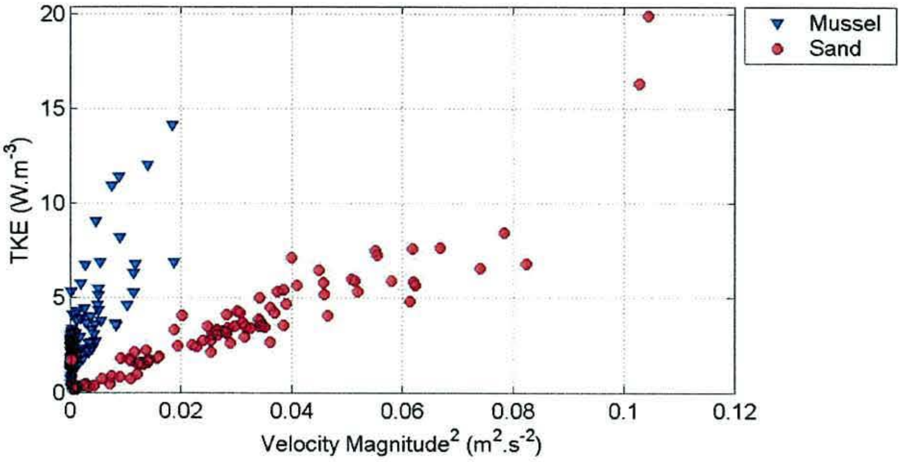

Figure 8.25. Absolute turbulent kinetic energy intensity plotted against the square of the mean velocity magnitude.

8.3 Discussion of results

These results show an influence of mussels on the near bed and mid-water hydrodynamics of the Oosterschelde. Evidence has previously been published in the literature of the very near bed hydrodynamic influence of mussels both in a flume (van Duren *et al.*, 2005) and in the field (Abelson *et al.*, 1993), however this dataset indicates the extent to which mussels influence turbulence higher in the water column.

ADCP results

The lack of strong wind and waves during most of the campaign allow the influence of waves on the dataset to be neglected. It is difficult to use the ADCP measurements to compare turbulence over the mussels and sand for 2 reasons. i) The ADCPs do not capture the very near bed region of the water column (especially the sand-site ADCP which did not have zed-head technology) and ii) the water depths and surrounding bathymetry at the two sites were different. A comparison between sites shows the velocities are slightly different at each site and the water depths differ by a factor of up to 30% at low water.

The delay in the phase of the M2 tidal velocities over the sand site (section 8.1.2) of the order of several minutes cannot be explained by a delay in the propagating tide. Using a mean depth of 7 m and a separation of 200 m, the propagation time for the tide between the sites is $T_{delay} = 200m/\sqrt{9.8ms^{-1} \times 7m} = 24s$.

The delay can be attributed to either increased friction over the mussel site, or local topography effects on the water velocities.

The comparison of the seabed drag coefficients using bed shear stress estimated from the variance method and the log profile method indicate a significant difference between the sites. Variance method estimates of the drag coefficient are 0.0032 ± 0.0003 over mussels and 0.0026 ± 0.0002 over sand. These values are close to the value of 0.0025 typically applied to flat, cohesionless seabeds. Log-profile estimates of the drag coefficient over mussels (0.0079 ± 0.0004) and over sand (0.0045 ± 0.0004) are similar to the values obtained for C_{100} by Green *et al.*, 1998 over horse mussels (using a similar log-profile approach).

The ratio of drag coefficients calculated using the variance method to the log profile method are 0.41 ± 0.02 over mussels and 0.55 ± 0.03 over sand. The ratio of 0.41 over mussels is remarkably consistant to that found by Lu *et al.*, 2000.

An increase in the drag coefficient over mussels suggests they are altering their surrounding hydrodynamics. This 'ecosystem-engineering' effect close to the sea bed has been described elsewhere in literature (van Duren *et al.*, 2005: Wildish *et al.*, 1984) and has implications for the structure of benthic mussel communities. An increase in turbulence over mussel beds caused by a larger drag coefficient enhances vertical diffusion, hence giving the mussels increased access to phytoplankton richer water higher in the water column, away from the mussels themselves.

It is observed that mussels tend to clump together in estuaries in order to create banded patterns of hummocks of the scale of metres (figure 6.1). It has been hypothesised that this increases the binding strength of the mussels to the sea bed. The increase in the size of bedforms also changes the effect of the mussels on the hydrodynamics. If the bed was uniformly covered with mussels of ~ 3 cm length, then this will act as a skin-friction effect on the flow of the water. On the other hand, if the mussels congregate together to form larger bedforms, then form drag plays a significant role.

The vertical profiles of velocity shown in figure 8.8 have interesting implications. Flow at the bottom boundary must decrease to 0. Therefore the shear in the near bed region (< 1m) over the mussel site must be low compared to the sand site. Although $\overline{u'w'}$ decreases as form drag becomes imporant near the bed, as shear is the denominator in equation 2.14, a significantly lower shear over mussels indicates an increase in N_z over mussels within the bottom metre.

The ADV data suggests measurable differences in hydrodynamics near the bed between the mussel and sand site. Near bed velocities estimated by extrapolating the ADCP velocities using the log-layer parameterisation match well over sand, indicating a log profile was reasonably well defined. However, over mussels, the measured ADV velocities were significantly lower than the interpolated log layer velocities.

The ADV was located over the centre of a patch of mussels, which develops it's own local boundary layer. By comparison, the log layer estimates are derived from the ADCP, which measures velocities higher in the water column where the boundary layer is a result of average upstream bed conditions. The ADV therefore measures velocities within an inner boundary layer and hence measures lower velocities.

The observation of a local internal boundary layer is supported by the TKE levels over the sites. Increased absolute TKE levels near the bed at the sand site support the hypothesis of enhanced bed roughness due to the presence of mussels. As the flow over the sand site is less turbulent, the shear (and hence the dominant TKE production region over sand) is concentrated in a region very near the bed (figure 8.26). This is reflected in the absolute TKE levels shown in figure 8.24b.

Normalising the TKE levels by the velocities (which are much stronger near the bed at the sand site – see figure 8.26) indicates that, relative to the mean flow, turbulence over the mussel site is up to an order of magnitude greater than that at the sandy site (figure 8.24c and 7.31). The near bed region over mussels is therefore slower, yet relatively more turbulent than the near bed region over sand. The above results indicate the presence of an internal boundary layer over the mussels where form drag plays a singificant role.

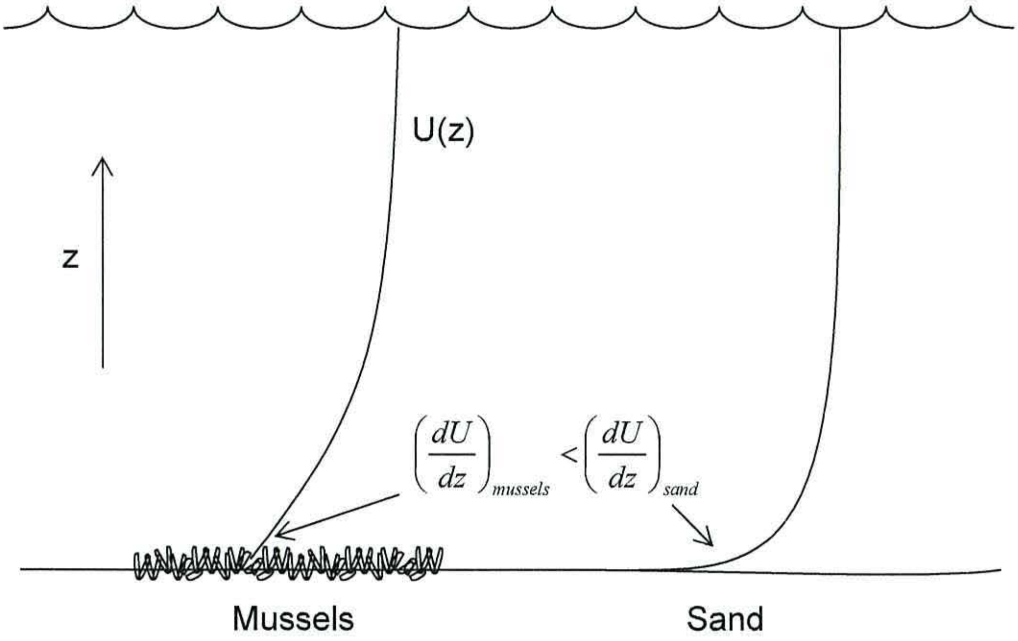

Figure 8.26. Schematic showing enhanced near-bed shear over the sand site.

To summarise the vertical flow structure: over sand there is a region of high shear near the bed and low normalised turbulence, above which the velocity is relatively constant. By contrast, over the mussel bed there is a region near the bed of low shear, slow velocities (compared to the near bed region at the sand site), above which there is greater midwater shear (compared to the midwater shear at the sand site).

Meanwhile, the vertical profile of Reynolds stress decrease linearly from the bed shear stress at the sea bed to 0 at the surface. Neglecting the 23% difference between the bed stress[‡] (and hence also midwater stresses) at the sites, equation 2.14 indicates that higher in the water column the diffusivity must be greater over the sand site (due to the decreased shear).

Mid-water estimates of N_z over the sand site are significantly higher than over the mussel bed. The greater water depth and hence associated length scales at the sand site would contribute to an increased N_z. However, non-dimensionalised values of N are still higher over sand compared to mussels. The greater $\partial u/\partial z$ in midwater over the mussel site contributes to a smaller N_z over the mussels.

ADCP estimates of TKE P in mid-water are higher over mussels than sand, as are values of ε made using the structure function method. A comparison between the

---

[‡] A increase in drag coefficient from 0.0026 over sand to 0.0032 over mussels will increase the bed stress by 23%

mussel and sand sites is difficult to quantify, however, because of the different water depths at the two sites.

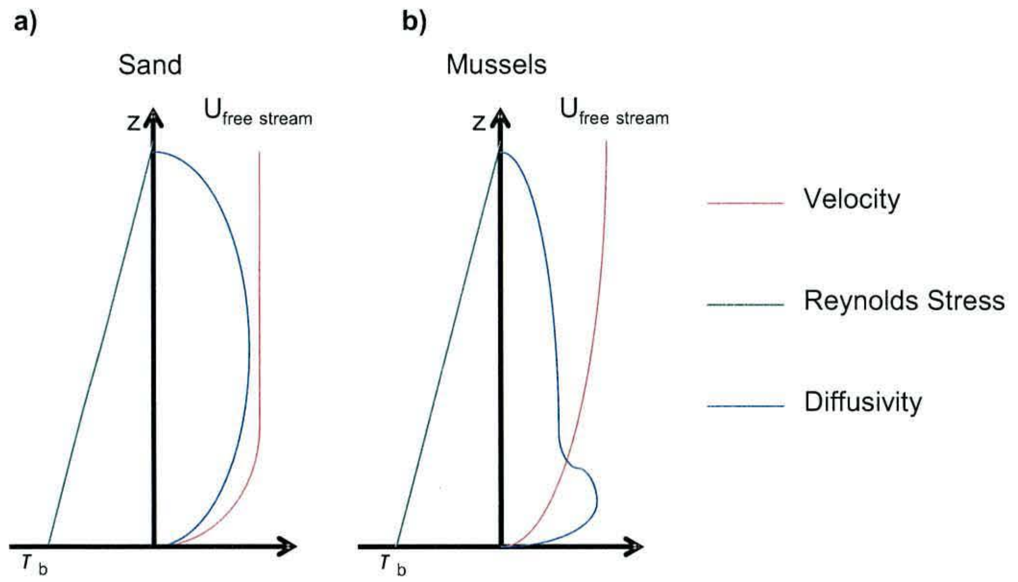

Figure 8.27. Idealised profiles of velocity, Reynolds stresses and diffusivity over (a) a sandy bed and (b) a mussel bed. The velocities show increased near bed shear over the sand site and its implications.

	Near Bed		Mid Water	
	Stress and Shear	Implications	Stress and Shear	Implications
Sand	$> \overline{u'w'}$ $>> \frac{\partial u}{\partial z}$	Decrease N Increase P	$< \overline{u'w'}$ $< \frac{\partial u}{\partial z}$	Increase N Decrease P
Mussels	$< \overline{u'w'}$ $<< \frac{\partial u}{\partial z}$	Increase N Decrease P	$> \overline{u'w'}$ $> \frac{\partial u}{\partial z}$	Decrease N Increase P

Table 8-1. Summary of results from Figure 8.27. (Near bed comparisons are relative only to near bed, midwater comparison are only relative to midwater. << indicates a strong decrease, < indicates a decrease, > indicates an increase and >> indicates a strong increase). The Implications are taken both from the definitions of *N* (equation 2.14) and *P* (equation 2.9) and from the observations.

Differences in the bed shear stress estimated from the law of the wall method and the variance method are consistent with previous studies. Lu *et al.*, 2000 found the stresses estimated at 3.6 mab were 41% of the bed shear stress estimated using the log profile, identical to the ratio obtained with the mussel site dataset. They attribute the overestimation of near bed stresses by the log profile method to the form drag caused by bed forms. This would provide an explanation for a closer ratio between the log-layer estimated bed stress and variance method estimated bed stress at the sand site, as mussel bed-forms were not present at the sand site. Some studies have been published investigating the existence of multiple log layers caused by form drag (Chriss *et al.*, 1982: van Duren *et al.*, 2005) however the non-conformance to von Karman's original hypothesis (see section 8.1.10) raises reservations about any interpretation from a log-layer approach.

The increased values of u_* higher in the water column (figure 8.23) could also be attributed to the effect of form drag caused by the mussels (Sanford *et al.*, 1999). An empirical formula for partitioning the friction into form drag and skin friction over a rippled bed was developed by Li, 1994. By setting the height of the mussel patches to 5-15 cm and the friction velocity to 0.05 m s^{-1}, it is estimated that 50%-59% of the stress experienced higher in the water column is due to form drag. The decrease in near bed Reynolds stresses shown in figure 8.9a which is consistant with the decrease in the near bed value of $\kappa z \frac{\partial u}{\partial z}$ shown in figure 8.23 indicate that the bottom bins of the ADCP are probably measuring a transition zone from the outer boundary layer to the inner boundary layer.

Time scales of diffusion at peak flow are similar over both sites, of the order of 5-10 minutes. The mixing time scale is larger than the advection time of water over an individual mussel plot at maximum flow ($100 \text{ m} \div 0.8 \text{ m s}^{-1} \approx 2$ minutes), implying that a benthic concentration boundary layer can develop over a mussel plot (figure 9.1).

The remnant of turbulence over the mussels during slack water (figure 8.25) measured by the ADV cannot be attributed to friction. This residual turbulence is produced by the exhalent jets of the filtering mussels (van Duren *et al.*, 2005). The exhalent jet turbulence is produced in and confined to a region close to the bed - it affects near-bed processes (e.g. remineralisation) but does not influence the larger scale vertical mixing of the water column.

9 Discussion

The development of a numerical model to describe the ecosystem of various estuaries containing aquaculture is a useful step to help manage such environments. Vertical mixing is a key component of such models and needs to be properly parameterised for the models to give a realistic hydrodynamic representation and to describe the interaction of the hydrodynamics with benthic mussel beds.

The coupling of benthic mussel communities with the overlying watercolumn is essential for their survival. In the absence of turbulence the mussels are isolated from their food and oxygen supply. In the two sites studied in this thesis, the energy supplied to vertical mixing comes from different sources.

Increased turbulence over biogenic structures is known to affect particle transport in various systems. The ability of organisms to influence their own food supply by modifying their physical environment is often called "ecosystem engineering" (Crooks *et al.*, 1999: Fogel *et al.*, 2004: Green *et al.*, 1998). The effect of increased bottom roughness, causing form drag, is a major factor influencing local vertical exchange. In the Oosterschelde, this is a dominant mechanism because of the strong influence of the tides. Due to the very low flow velocities and the consequently limited generation of turbulence at the bed, the scope for ecosystem engineering by mussels in systems such as Limfjorden is limited in comparison to tidally driven systems with higher velocities. This in accordance with the findings of Ackerman *et al.*, 2001 who also found that in low energy environments such as lakes, zebra mussels, *Dreissena polymorpha* had a more limited effect on the water column than previously thought. In Limfjorden the mussels depend on sinking and wave-driven mixing for access to food higher up in the water column.

9.1 Limfjorden

In the Limfjorden vertical mixing is driven by meteorological forcing. The weak tidal and residual flow also means that there is little advection of phytoplantkon and primary production occurs locally. Over the most recent summer (2006), stable weather patterns experienced in northern Denmark allowed stratification to persist for prolonged periods of time. The commercial crop of mussels was seriously depleted, despite the high levels of algal growth near the surface (where the phytplankton were not subjected to the grazing pressures of mussels). The economic impacts of this are obvious.

Model calculations for the wind-driven micro-tidal conditions in Limfjorden suggest that vertical mixing is the main transport mechanism in the water column providing mussels with food. This confirms the findings of Dolmer, 2000, and is in agreement with the relatively long water residence time in Limfjorden compared to other systems (Dame *et al.*, 1998). Mixing depths in the shallow Limfjorden are not critical for phytoplankton production, assuming a Secchi depth of 7 m. Thus, even during mixing to full depth, phytoplankton may have enough light to grow and out-compete the grazing pressure of the mussels. As a consequence, the development of phytoplankton and mussel populations depends mainly on the time scales of mussel clearance rates, phytoplankton growth rates, and the alternation of mixing and stratification.

The presence of stratification has an immediate negative impact on the supply of phytoplankton to benthic mussel beds. However, in the Limfjorden, the long-term average effects of the regular switching between a stratified and a fully mixed water column remain to be assessed and may be beneficial. If the water column is continuously fully mixed, then the benthic community is coupled to the pelagic phytoplankton population throughout the entire water column. In a relatively confined shallow basin, this may allow the benthic filter feeders to graze upon and deplete the total phytoplankton population to low levels, as has been demonstrated in several Danish estuaries (Møhlenberg, 1995: Riisgård *et al.*, 1998: Riisgård *et al.*, 2004). In a stratified situation where the benthos has no access to the upper part of the water column, phytoplankton blooms can develop in the upper layer, provided that nutrients are not limiting and zooplankton is not able to exert top-down control (Cloern, 1982: Daborn, 1986: Officer *et al.*, 1982). When the water column subsequently mixes during a wind/wave event, the benthic filter feeders get access to this high concentration of phytoplankton in the upper water region. If the prevailing situation in the system is the fully mixed, brief periods of stratification would provide the phytoplankton with a temporary refuge, allowing the algal population to recover. Møhlenberg (1995) showed that in the Roskilde fjord in Denmark algal concentrations increased very rapidly under stratified conditions, but were reduced sharply due to mussel filtration in fully mixed periods.

If the total production of phytoplankton integrated over time is less in the continuously mixed case than in the alternately mixed/stratified case, and mussels are assumed to be the dominant consumers, this could imply that brief periods of stratification could ultimately be beneficial to the mussel population in this region. Whether or not the mussel population benefits from brief stratification periods, or whether stratification limits mussel growth, will depend on a large number of factors, including the periodicity of events, algal production rate in the mixed and stratified situation and the time it takes for the mussels to deplete the whole water column of algae. The latter prerequisite seems likely to be fulfilled in Limfjorden, due to the extent of the mussel beds, the limited depth of the water column and the limited advection of water masses. The total balance clearly needs further investigation.

The major factors influencing stratification during summer in the Limfjorden were identified to be solar heating and wave stirring. During winter the heat exchange term is negative and leads to convective overturning during cold atmospheric conditions. All of these factors are driven by the local weather conditions. Therefore the time scale of these events is likely to be similar to the passing weather systems. During the period of our fieldwork, this was about 5-7 days. More investigation into existing stratification and weather data sets would clarify this relationship and the effect this has on local mussel aquaculture.

9.2 Oosterschelde

The Oosterschelde is dominated by the predictable cycles of the tides. The strong mixing generated by the tides keeps the water column fully mixed and hence the mussels tightly coupled to the phytoplankton population. The mussels therefore continually graze on the phytoplankton and keep the population levels in check. Primary production does occur locally, but a significant proportion of phytoplankton are advected from outside the embayment.

A semi-analytical model describing the flow of water over mussel patches, the grazing of the mussels and the associated decrease in food supply to mussels is to be developed. Such a model will help determine the optimal size of mussel patches, the spatial pattern of food supply over the patches and the associated growth rates. The supply of phytoplankton to the mussel patch is affected by local primary productivity, mixing time scales, water velocities and depths, plot sizes, distance between plots and mussel filtration rates.

As indicated in figure 9.1, the leading edge of the mussel patch will experience a relatively high concentration of phytoplankton. Further back in the mussel patch, a concentration boundary layer will start to form. As the distance from the leading edge increases, the phytoplankton concentration continues to decrease. Eventually, the concentrations drop so low that it will not be profitable for mussels to grow in that location. A region of bare sand will allow phytoplankton concentrations to diffuse back into the bottom boundary layer and the cycle then starts again.

In a tidal situation the flow usually reverses every 6 hours. When the flow reverses direction, what was a trailing edge becomes a leading edge and vice versa. The patch is likely to therefore exhibit symmetry in the flood ebb direction.

Table 9-1 suggests some simple results expected from the model. If the mussel clearance rate and mixing time scale are much longer than the time taken for a water parcel to be advected over the mussel plot then a concentration boundary layer will form.

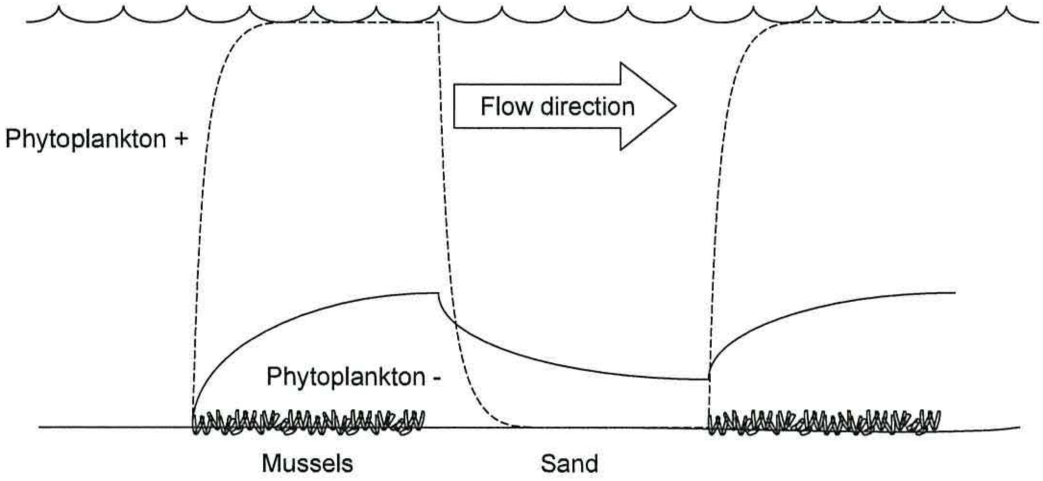

Figure 9.1. Height of depletion boundary layer over mussel plots (not to scale) – assuming an instantaneous change in turbulence at the edges of the mussel plots. The lines indicate an arbitrary level of phytoplankton concentration The solid line indicates when the mixing time scale is comparable to the advection time scale – the near mussel phytoplankton concentration will be relatively low. The dashed line is when the mixing time scale is much shorter than the advection time scale over each plot – the near mussel phytoplankton concentration will be relatively high.

F(Mixing Time Scale,Filtration Rate) **/** **Advection time scale**	**Implications**
>>1	Concentration Boundary Layer (CBL) forms. Mussels away from the leading edge of the plot will experience severe depletion of phytoplankton
~1	CBL starts to form. Mussels away from the leading edge of the plot will begin to experience depletion
<<1	No CBL forms, vertical mixing continuously supplies phytoplankton

Table 9-1. Relationship between mussel plot size and vertical mixing time scale. The left column is a function of the mixing time scale and mussel filtration rate divided by the advection time scale, the right column is the implications this has on the mussels in the plot.

9.3 Differences between estuaries

The two systems studied here support large mussel industries with similar methods of cultivation (benthic). However they possess contrasting physical characteristics. Limfjorden is micro-tidal – local primary production is an important factor, advection is not a dominant process in food supply, and vertical mixing during summer occurs only during periods of high winds (and less significantly, at night), hence mixing and stratification cycles have the period of a few days-weeks.

By contrast, the velocities in the Oosterschelde embayment are dominated by strong tides. Horizontal advection plays a complicated role – high concentrations of phytoplankton are advected through the storm surge barrier, however this only affects the western end of the Oosterschelde (The tidal excursion of a fluid parcel travelling in an M2 tidal motion with velocity amplitude 0.8 m s^{-1} is 11.5 km). Mussel aquaculture is not omnipresent in the Oosterschelde, so there are regions where phytoplankton can grow unmolested by mussels and then be advected over cultivated areas. Primary production within the estuary is important, as the flushing time is of the order of 6 days. Vertical diffusion is driven by the tidal forcing and is therefore ubiquitous – tidal stirring is always strong enough to prevent stratification developing, even during neap tides and (the very short) slack water.

Waves are an important mixing generation mechanism in Limfjorden. The waves couple the wind energy to the water column, increasing the wind mixing efficiency. The amount of turbulence therefore depends on the fetch and hence the direction of the wind. The bottom boundary layer turbulence created by wave orbital motions is small, but measurable.

Wind speed, significant wave height, wave period and water depth at the Oosterschelde fieldsite are similar to Limfjorden. Both field sites border the North Sea, and experience similar climatic conditions. But because turbulence is driven primarily by the tides in the Oosterschelde, the wind and waves are not important in the local TKE budget.

9.4 Effects of ecological-engineering

The ability of mussels to affect their local environment, either as an individual or collectively influences mussel behaviour and distribution patterns (Van de Koppel *et al.*, 2001). The ability to generate turbulence at the small scale by the exhalant siphon is well documented (van Duren *et al.*, 2005), and clear evidence is again presented here. While the exhalant siphon jet allows the mussels to influence the very near bed region, this does not affect flow on a larger scale.

The observation of a greater drag coefficient over mussel beds provides evidence that mussels do influence the local hydrodynamics on a water depth scale. Models written 20 years previous (Wildish *et al.*, 1979) use very simple parameterisations to describe vertical food supply to mussels. The application of datasets similar to those discussed in this thesis combined with the associated phytoplankton measurements allow the validity of these models to be investigated. Such work is currently being prepared for publication.

9.5 Development of ADCP technology

Existing ADCP methods of estimating turbulence were successfully employed in the Oosterschelde. This allowed the estimation of Reynolds stresses, TKE production rates and turbulent diffusivities.

A novel method of using ADCPs to estimate turbulent dissipation rates has been presented and successfully compared with exisitng measurements of turbulent dissipation rates.

9.6 Generality of findings and Future developments in ADCP algorithms

The 1D analytical model developed for Limfjorden in section 7.3 has potential to be applied to other shallow estuaries. A knowledge of the depth and meteorological conditions – combined with a wave model (also including tides and horizontal density gradient if they are deemed important) is required to drive the model and predict periods of extended stratification. This would help mussel farmers predict periods of extended stratification and identify suitable regions for mussel production. Funding has been sought by NERI (National Environmental Research Institute – Denmark) to analyze Danish meteorological and hydrodynamic databases to extend the use of the model to other Danish fjords.

The development of the 'refuge model' (section 9.1) and of the advection-grazing model (section 9.2) will probe the impact of vertical mixing time scales, grazing rates, primary production rates, velocities, etc. on mussel cultivation in a larger context.

Initially it was proposed to measure turbulence parameters using microstructure profiling instruments. With hindsight it was prudent to use the ADCP instead. The free-falling profiler takes 5-10 metres to reach a stable fall speed, which is too deep for these environments. The profiler would have also required a team of people to operate it while measurements were taken. In contrast, the ADCP measures most of the water column except for a (very important!) small region near the bed and near the surface. Once deployed, the ADCP operates autonomously until either the battery runs down or the memory is full.

An unaccomplished aim of the experiments was to estimate vertical fluxes of phytoplankton and nutrients at the mussel/water interface. This was to be achieved by combining the turbulence measurements of the ADCP with near bed phytoplankton gradients measured using a siphon mimic apparatus. The desired datasets were not gathered in these two environments because 1) in Limfjorden the turbulence levels were too low for the ADCPs to measure reliably and 2) in the Oosterschelde, the field campaign coincided with a phaeocystis bloom, which disrupted the phytoplankton measurements and the mussel feeding behaviour.

Recent developments, such as using the ADCP in pulse coherent mode (Lorke *et al.*, 2005) and the structure function method (section 4) lower the noise of the turbulence measurements. The ability to measure low turbulence levels in low energy benthic boundary layer opens interesting avenues. Turbulence data has recently been collected from lake Bala with a pulse coherent Doppler. The internal seiching of the lake produces bed-driven turbulence which has been measured by the ADCP. These measurements have a very low noise threshold of $\sim 10^{-6}$ W m^{-3}, comparable with the FLY microstructure profiler. Lorke *et al.*, 2005 used similar measurements in conjunction with nutrient gradient to estimate benthic fluxes. An opportunity to revisit the Limfjorden using the new technology would allow the concurrent measurements of turbulence and phytoplankton profiles to be made, hence enabling us to make estimates of vertical nutrient and carbon fluxes.

Experiments are proposed to combine a 3D particle tracking instrument (Alex Nimmo-Smith, personal communication) with the ADCP to investigate the structure of benthic turbulence and it's influence on ADCP measurements (for example, the effect of turbulent vortices on the structure function calculations). Field experiments are also planned in summer 2007 by the phytoplankton component of the MaBenE consortium and funding is currently being sought to use the ADCPs to measure turbulence along side.

The prospect of turbulence measurements from a moving vessel using the structure function approach could allow the mapping of island wakes and the mapping of the horizontal structure of turbulence generation, advection and dissipation. Datasets have been recently collected from the Prince Madog with a 600 kHz downlooking ADCP which awaits analysis. The application of the structure function approach to lowered ADCPs is also another promising avenue to pursue.

The potential to reduce the vertical averaging of the structure function method shows promise in stratified regions. This still has to be investigated, as does the influence of waves (internal and surface) on the structure function approach.

Other algorithm developments have also to be investigated. An eddy covariance method, using the ability of the ADCP to measure velocity and particle concentration at the same time and space has been tested alongside microstructure profiler casts with encouraging results.

10 Appendices.

10.1 Structure Function Method

A mathematical basis for the $r^{2/3}$ relationship for the structure function is presented below.

Kolmogorov theory describes the spectral distribution of turbulent kinetic energy ($S(k)$) over the wavenumber distribution (k) in relation to the turbulent kinetic energy dissipation ε as;

$$S(k) = A\varepsilon^{2/3}k^{-5/3}$$

by performing a Fourier transform, this is converted to the spatial domain:

$$S(r) = \int_0^\infty e^{ikr} A\varepsilon^{2/3}k^{-5/3}dk$$

The constants (with respect to r) $A\varepsilon^{2/3}$ can be moved outside the bracket and the relation $dk = \frac{1}{r}d(kr)$ can be substituted to give

$$S(r) = A\varepsilon^{2/3}\frac{1}{r}\int_0^\infty e^{ikr}k^{-5/3}d(kr)$$

$$S(r) = A\varepsilon^{2/3}\frac{r^{5/3}}{r}\int_0^\infty e^{ikr}(kr)^{-5/3}d(kr)$$

$$S(r) = A\varepsilon^{2/3}r^{2/3}[\text{Constant}]$$

equating the constant to an arbitrary C_v^2:

$$S(r) = C_v^2\varepsilon^{2/3}r^{2/3}$$

10.2 General Bias in ADCP velocities near the bed

Due to the range-gating method used by the ADCP to divide the water column up into depth bins, the measured velocities are averaged over a triangular weighting function with respect to depth (RDInstruments, 1996).

Presented here is an analysis on how this vertical averaging affects velocity estimates from the ADCP in a logarithmic boundary layer.

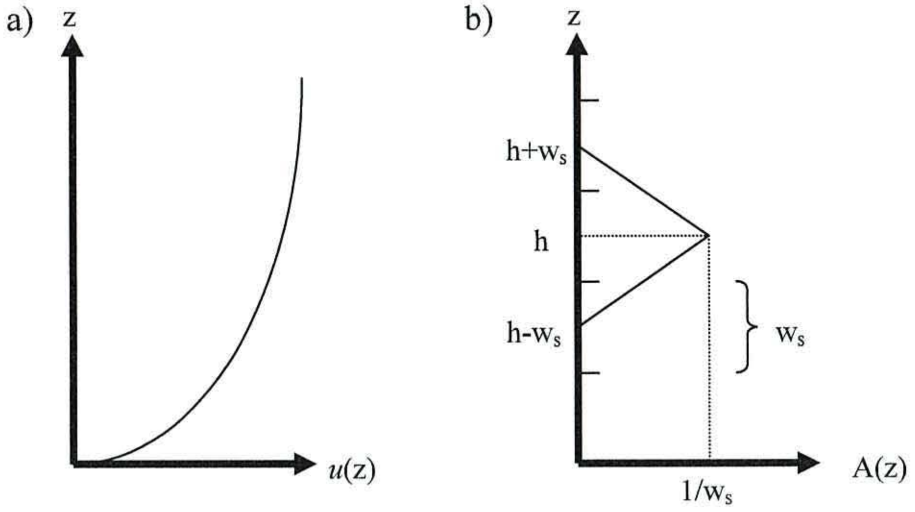

Figure 10.1 a) Logarithmic velocity profile, b)the weighting window of the ADCP velocity estimate. If an ADCP is set to have bins of size w$_s$, the actual velocity measured at the centre of the depth bin (h) will be a triangle weighted average including half of the adjacent bins (RDInstruments, 1996).

Given a logarithmic velocity profile as in figure 10.1a, which can be described as

$$u(z) = \frac{u_*}{\kappa}\ln\left(\frac{z}{z_0}\right)$$

and a velocity weighting function as in figure 10.1b, which can be described as

$$A(z) = \left.\begin{array}{ll} \frac{1}{w_s^{\,2}}\left(z-(h-w_s)\right) & h-w_s < z \le h \\ \frac{1}{w_s^{\,2}}\left(-z+(h+w_s)\right) & h < z < h+w_s \end{array}\right\}$$

Then the actual velocity measured by the ADCP will be given by:

$$U_{measured}(z) = \int_{bin} u(z)A(z)dz$$

$$= \int_{h-w_s}^{h+w_s} \frac{u_*}{\kappa}\ln\left(\frac{z}{z_0}\right)A(z)dz$$

Equation 10.1

$$U_{measured}(z) = \frac{u_*}{w_s^{\,2}\kappa}\left[\int_{h-w_s}^{h}(\ln(z)-\ln(z_0))(z-(h-w_s))dz + \int_{h}^{h+w_s}(\ln(z)-\ln(z_0))(-z+(h+w_s))dz\right]$$

The first integral can be expanded to:

$$= \int_{h-w_s}^{h} z\ln(z) - z\ln(z_0) - (h-w_s)\ln(z) + (h-w_s)\ln(z_0)dz$$

$$= \left[\frac{z^2}{2}\ln(z) - \frac{z^2}{4} - \frac{z^2}{2}\ln(z_0) - (h-w_s)(z\ln(z)-z) + z(h-w_s)\ln(z_0)\right]_{h-w_s}^{h}$$

$$= \ln(h)\left(-\frac{h^2}{2}+hw\right) + \frac{(h-w_s)}{2}\ln(h-w_s) - \frac{w_s^{\,2}}{2}\ln(z_0) + \frac{hw_s}{2} - 3\frac{w_s^{\,2}}{4}$$

Similarly, the second integral goes to give:

$$= \ln(h)\left(-\frac{h^2}{2}-hw\right) + \frac{(h+w_s)^2}{2}\ln(h+w_s) - \frac{w_s^{\,2}}{2}\ln(z_0) - \frac{hw_s}{2} - 3\frac{w_s^{\,2}}{4}$$

Recombining back into Equation 10.1 gives:

$$U_{measured}(z) = \frac{u_*}{\kappa w_s^{\,2}}\left[\begin{array}{c}\frac{(h-w_s)^2}{2}\ln(h-w_s) + \frac{(h+w_s)^2}{2}\ln(h+w_s) \\ -h^2\ln(h) - w_s^{\,2}\ln(z_0) - \frac{3}{2}w_s^{\,2}\end{array}\right]$$

or alternatively:

$$U_{measured}(z) = \frac{u_*}{\kappa w_s^{\,2}}\left[\begin{array}{c}\frac{h^2+w_s^{\,2}}{2}\ln(h^2-w_s^{\,2}) + hw_s\ln\left(\frac{h+w_s}{h-w_s}\right) \\ -h^2\ln(h) - w_s^{\,2}\ln(z_0) - \frac{3}{2}w_s^{\,2}\end{array}\right]$$

So does this make a real difference?

Figure 10.2a,b shows the effect this has on the mean velocity. There is a difference of 2.5% between the measured and idealised velocity at 0.31 m above the bed (The ADCP cannot measure closer to the bed than one bin length due to the triangular weighting). As adjacent ADCP bins are separated by 0.3 m, this will have a minimal impact on mean velocities and shear.

The estimated values of $z\frac{\partial u}{\partial z}$ are actually increased by the triangular averaging figure 10.2c, indicating that the decrease in $z\frac{\partial u}{\partial z}$ given in (section 8.1.10) are physical rather than an artefact of the ADCP.

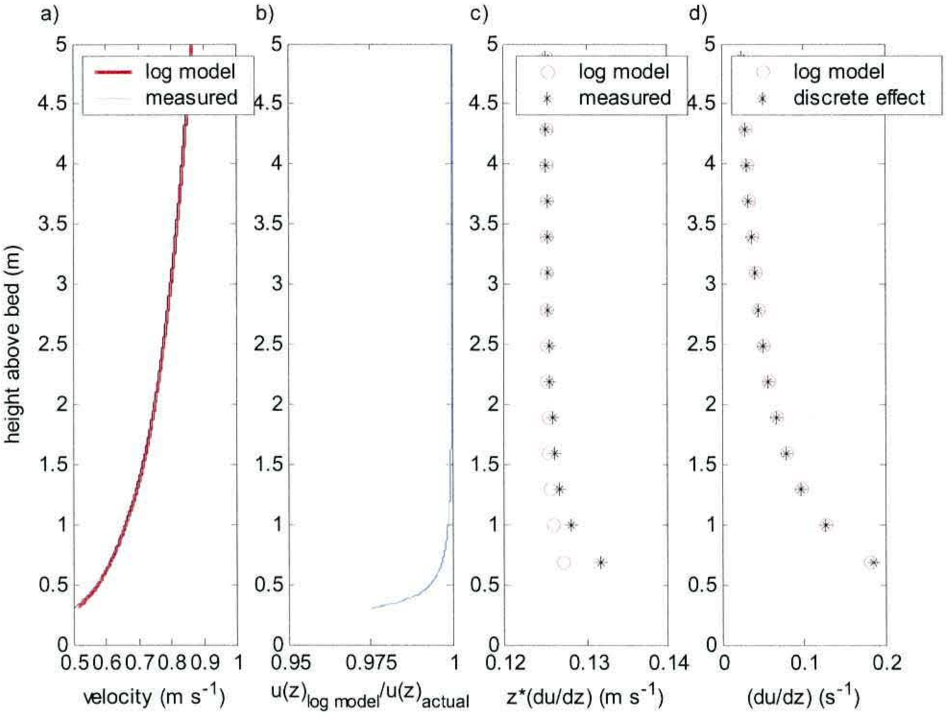

Figure 10.2 The effect of the triangular weighting on ADCP velocities. a) The actual velocities calculated using the law of the wall approach ($u(z)=\frac{u_*}{\kappa}\ln\left(\frac{z}{z_0}\right)$), and the effect of the triangular weighting. b) The ratio of measured velocity to idealised velocity and c) The impact this has on the u_* estimate ($u_*=0.4\frac{du(z)}{d\ln(z)}$). The values used here are similar to the values over the mussel site, i.e. u_*=0.05 m s^{-1}, z_0=0.005 m and ADCP bin length w_s=0.3 m. d) the error in the shear estimate from using a discrete difference.

Figure 10.2c also indicates an increase in $z\frac{\partial u}{\partial z}$ even when triangle weighting is not considered. The use of a finite difference in calculating the shear also has an effect on the estimated shear;

A comparison of the log layer estimate of the shear:

$$\frac{\partial u}{\partial z} = \frac{u_*}{\kappa z}$$

with a measured estimate of the shear using a finite difference method (figure 10.3), which is given by

$$\frac{\Delta u}{\Delta z} = \frac{\frac{u_*}{\kappa}\ln\left(\frac{z+\frac{\Delta z}{2}}{z_0}\right) - \frac{u_*}{\kappa}\ln\left(\frac{z-\frac{\Delta z}{2}}{z_0}\right)}{\Delta z}$$

$$\frac{\Delta u}{\Delta z} = \frac{u_*}{\kappa}\ln\left(\frac{z+\frac{\Delta z}{2}}{z-\frac{\Delta z}{2}}\right)\frac{1}{\Delta z}$$

is shown in figure 10.2d. In the shear region close to the bed, the estimated shear is slightly larger than the shear predicted by the log model.

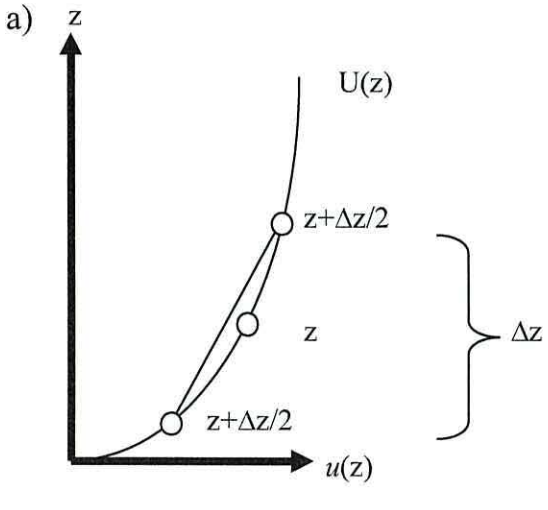

Figure 10.3. Effect of finite difference on the calculated velocity shear in a log layer. The actual gradient of U(z) is overestimated when using a finite difference approach.

References

Abelson, A., M. Miloh, and L. Yossi, 1993: Flow patterns induced by substrata and body morphologies of benthic organisms and their roles in determining availability of food particles. *Limnology and Oceanography*, **38,** 1116-1124.

Ackerman, J. D., M. R. Loewen, and P. F. Hamblin, 2001: Benthic-pelagic coupling over a zebra mussel reef in western lake erie. *Limnology and Oceanography*, **46,** 892-904.

Baumert, H., J. H. Simpson, and J. Sündermann, 2005: *Marine turbulence. Theories, observations and models. Results of the cartum project.* Cambridge University Press.

Chriss, T. M. and D. R. Caldwell, 1982: Evidence for the influence of form drag on bottom boundary-layer flow. *Journal of Geophysical Research-Oceans and Atmospheres*, **87,** 4148-4154.

Cloern, J. E., 1982: Does the benthos control phytoplankton biomass in south san francisco bay? *Marine ecology progress series. Oldendorf*, **9,** 191-202.

Coelho, H. S., R. J. J. Neves, M. White, P. C. Leitã, and A. J. Santos, 2002: A model for ocean circulation on the iberian coast. *Journal of Marine Systems*, **32,** 153-179.

Crooks, A. J. and H. S. Khim, 1999: Architectural vs. Biological effects of a habitat-altering, exotic mussel, *musculista senhousia*. *Journal of Experimental Marine Biology*, **240,** 53-75.

Daborn, G. R., 1986: Effects of tidal mixing on the plankton and benthos of estuarine regions of the bay of fundy, 390-413.

Dame, R. F. and T. C. Prins, 1998: Bivalve carrying capacity in coastal ecosystems. *Aquatic Ecology*, **31,** 409-421.

Dewey, R. K., W. R. Crawford, A. E. Gargett, and N. S. Oakey, 1987: A microstructure instrument for profiling oceanic turbulence in coastal bottom boundary layers. *J. Atmos. Ocean. Technol.*, **4,** 288-297.

Dolmer, P., 2000: Algal concentration profiles above mussel beds. *Journal of Sea Research [J. Sea Res.].* **43,** 113-119.

Dolmer, P. and R. P. Frandsen, 2002: Evaluation of the danish mussel fishery: Suggestions for an ecosystem management approach. *Helgoland Marine Research [Helgol. Mar. Res.].* **56,** 13-20.

Drinkwaard, A. C., 1998: Introductions and developments of oysters in the north sea area: A review. *Helgoland Meeresuntersuchungen*, **52,** 301-308.

11-References

Fernandes, L., S. Saraiva, P. C. Leitã, P. Pina, A. D. Santos, F. Braunschweig, and R. Neves, 2006: Managing benthic ecosystems in relation to physical forcing and environmental constraints (mabene)MaBenE Deliverable D1.1b.

Fogel, B. N., C. M. Crain, and M. D. Bertness, 2004: Community level engineering effects of *triglochin maritima* (seaside arrowgrass) in a salt marsh in northern new england, USA. *Journal of Ecology*, **92,** 589-597.

Frisch, U., 1995: *Turbulence : The legacy of A.N. Kolmogorov*. Cambridge University Press.

Gargett, A. E., 1978: Microstructure and fine structure in an upper ocean frontal regime. *J. Geophys. Res.*, **83,** 5123-5134.

Green, M. O., J. E. Hewitt, and S. F. Thrush, 1998: Seabed drag coefficient over natural beds of horse mussels (atrina zelandica). *Journal of Marine Systems*, **56,** 613-637.

Herman, P. M. J., J. J. Middelburg, J. Van de Koppel, and C. H. R. Heip, 1999: Ecology of estuarine macrobenthos. *Advances in ecological research, vol 29, academic press inc*, 195-240.

Howarth, M., 2002: Estimates of reynolds and bottom stress from fast sample adcps deployed in continental shelf seas. *Proceedings of Hydraulic Measurements and Experimental Methods 2002*, 10.

Howarth, M. and A. Souza, 2005: Reynolds stress observations in continental shelf seas. *Deep-Sea Research Part Ii-Topical Studies in Oceanography*, **52,** 1075-1086.

Howarth, M. J., 1999: Wave measurements with an adcp. *Proc. of the IEEE/OES Working Conference on Current Measurement Technology*, 41-44.

Hyder, P. and A. J. Elliott, 1995: Observations and model simluations of a near-shore tidal eddy. *Journal of Marine Environmental Engineering*, **1,** 315-333.

Klepper, 1989: A model of carbon flows in relation to macrobenthic food supply in the oosterschelde estuary (s.W. Netherlands). University of Wageningen, 270.

Kolmogorov, A. N., 1941: The local structure of turbulence in an incompressible viscous fluid for very large reynolds number. *Izv. Acad. Sci., USSR*, **30,** 301-305.

Kundu, P. K., 1990: *Fluid mechanics*. Academic Press, Inc.

Lhermitte, R., 1968: Turbulent air motion as observed by doppler radar. *13th Radar Meteorological Conference*, McGill University, American Meterological Society, 498-503.

——, 1973: Meteorological doppler radar. *Science*, **182,** 258-262.

Li, M. Z., 1994: Direct skin friction measurements and stress partitioning over movable sand ripples. *Journal of geophysical Research-Oceans*, **99,** 791-799.

Lohrmann, A., B. Hackett, and L. P. Roed, 1990: High-resolution measurements of turbulence, velocity and stress using a pulse-to-pulse coherent sonar. *J. Atmos. Ocean. Technol.*, **7,** 19-37.

Lorke, A. and A. Wüest, 2005: Application of coherent adcp for turbulence measurements in the bottom boundary layer. *Journal of Atmospheric and Oceanic Technology*, **22,** 1821-1828.

Lu, Y. and R. G. Lueck, 1999a: Using a broadband adcp in a tidal channel. Part i: Mean flow and shear. *J. Atmos. Ocean. Technol.*, **16,** 1556-1567.

——, 1999b: Using a broadband adcp in a tidal channel. Part ii: Turbulence. *J. Atmos. Ocean. Technol.*, **16,** 1568-1579.

Lu, Y., R. G. Lueck, and D. Huang, 2000: Turbulence characteristics in a tidal channel. *J. Phys. Oceanogr.*, **30,** 855-867.

Masch, F. D., 1963: Mixing and dispersion of wastes by wind and wave action. *Int J Air Water Poll*, **7,** 697-720.

Møhlenberg, F., 1995: Regulating mechanisms of phytoplankton growth and biomass in a shallow estuary. *Ophelia*, **42,** 239-256.

Morales, R. A., A. J. Elliott, and T. Lunel, 1997: The influence of tidal currents and wind on mixing in the surface layers of the sea. *Marine Pollution Bulletin*, **34,** 15-25.

Mulder, J. P. M. and T. Louters, 1994: Changes in basin geomorphology after implementation of the oosterschelde estuary project. *Hydrobiologia*, **282-283,** 29 - 39.

Nienhuis, P. H. and A. C. Smaal, 1994: The oosterschelde estuary, a case-study of a changing ecosystem: An introduction. *Hydrobiologia*, **282-283,** 1-14.

Nikora, V. I. and D. G. Goring, 1998: Adv measurements of turbulence: Can we improve their interpretation? *J. Hydraul. Eng.*, **124,** 630-634.

Oakey, N. S. and B. J. W. Greenan, 2004: Mixing in a coastal environment: 2. A view from microstructure measurements. *J. Geophys. Res.*, **109**.

Officer, C. B., T. J. Smayda, and R. Mann, 1982: Benthic filter feeding - a natural eutrophication control. *Marine Ecology-Progress Series*, **9,** 203-210.

Osborn, T. R., 1980: Estimates of the local rate of vertical diffusion from dissipation measurements. *J. Phys. Oceanogr.*, **10,** 83-89.

Peters, H. and R. Bokhorst, 2001: Microstructure observations of turbulent mixing in a partially mixed estuary. Part ii: Salt flux and stress. *J. Phys. Oceanogr.*, **31,** 1105-1119.

Pinkel, R., 1979: Observations of strongly nonlinear internal motion in the open sea using a range-gated doppler sonar. *J. Phys. Oceanogr.*, **9,** 675-686.

RDInstruments, 1996: *Acoustic doppler current profiler, principles of operation, a practical primer*. RD Instruments, 52 pp.

Riisgård, H. U., A. S. Jensen, and C. Jurgensen, 1998: Hydrography near-bottom currents, and grazing impact of the filter feeding ascidian *ciona intestinalis* in a danish fjord. *Ophelia*, **49,** 1-16.

Riisgård, H. U., D. F. Seerup, M. H. Jensen, E. Glob, and P. S. Larsen, 2004: Grazing impact of filter-feeding zobenthos in a danish fjord. *Journal of Experimental Marine Biology*, **307,** 261-271.

Rippeth, T. P., 2005: Mixing in seasonally stratified shelf seas: A shifting paradigm. *Philos T Roy Soc A*, **363,** 2837-2854.

Rippeth, T. P., E. Williams, and J. H. Simpson, 2002: Reynolds stress and turbulent energy production in a tidal channel. *J. Phys. Oceanogr.*, **32,** 1242-1251.

Rippeth, T. P., J. H. Simpson, E. Williams, and M. E. Inall, 2003: Measurement of the rates of production and dissipation of turbulent kinetic energy in an energetic tidal flow: Red wharf bay revisited. *J. Phys. Oceanogr.*, **33,** 1889-1901.

Rippeth, T. P., M. R. Palmer, J. H. Simpson, N. R. Fisher, and J. Sharples, 2005: Thermocline mixing in summer stratified continental shelf seas. *Geophysical Research Letters*, **32,** L05602.

Sanford, T. B. and R.-C. Lien, 1999: Turbulent properties in a homogeneous tidal bottom boundary layer. *Journal of Geophysical Research. C. Oceans [J. Geophys. Res.*, **104,** 1245-1257.

Sauvageot, H., 1992: *Radar meteorology*. Artech House Books, 384 pp.

Seitz, R. C., 1971: Results of a field study using the 3-axis doppler shift current meter. *Tech. Rep. Chesapeake Bay Inst*, **72.**

Simpson, J. H. and D. Bowers, 1981: Models of stratification and frontal movement in shelf seas. *Deep-Sea Research*, **28,** 727-738.

Simpson, J. H., J. Brown, J. Matthews, and G. Allen, 1990: Tidal straining, density currents, and stirring in the control of estuarine stratification. *Estuaries*, **13,** 125-132.

Simpson, J. H., P. Hyder, T. P. Rippeth, and I. M. Lucas, 2002: Forced oscillations near the critical latitude for diurnal-inertial resonance. *J. Phys. Oceanogr.*, **32,** 177-187.

Smaal, A. C. and P. H. Nienhuis, 1992: The eastern scheldt (the netherlands), from an estuary to a tidal bay: A review of responses at the ecosystem level. *Netherlands Journal of Sea Research,* **30,** 161-173.

Smaal, A. C., J. H. G. Verhagen, H. A. Haas, and J. Coosen, 1986: Interaction between seston quantity and quality and benthic suspension feeders in the oosterschelde (the netherlands). *Ophelia,* **26,** 385-399.

Soulsby, R. L., 1983: The bottom boundary layer of shelf seas. 189-266 pp.

Stacey, M. T., S. G. Monismith, and J. R. Burau, 1999a: Measurements of reynolds stress profiles in unstratified tidal flow. *J. Geophys. Res.*, **104,** 10933-10949.

——, 1999b: Observations of turbulence in a partially stratified estuary. *J. Phys. Oceanogr.*, **29,** 1950-1970.

Stansfield, K., 2001: The probability distribution of the thorpe displacement within overturns in juan de fuca strait. *Journal of Physical Oceanography,* **12,** 3421-3434.

Taylor, G. I., 1935: Statistical theory of turbulence. *Proceedings of the Royal Society of London A,* **151,** 421-444.

——, 1938: Production and dissipation of vorticity in a turbulent fluid. *Proceedings of the Royal Society A,* **164,** 15-23.

Ten Brinke, W. B. M., J. Dronkers, and J. P. M. Mulder, 1994: Fine sediments in the oosterschelde tidal basin before and after partial closure. *Hydrobiologia,* **282/283.**

Turner, J. S., 1981: Small-scale mixing processes. *The evolution of physical oceanography*, MIT Press.

Van de Koppel, J., P. M. J. Herman, P. Thoolen, and C. H. R. Heip, 2001: Do alternate stable states occur in natural ecosystems? Evidence from a tidal flat. *Ecology,* **82,** 3440-2461.

van Duren, L. A., P. M. J. Herman, A. J. J. Sandee, and C. H. R. Heip, 2005: Effects of mussel filtering activity on boundary layer structure. *Journal of Sea Research,* **55,** 3-14.

Vroon, J., 1994: Hydrodynamic characteristics of the oosterschelde in recent decades. *Hydrobiologia,* **282-283,** 17-27.

11-References

Wildish, D. J. and D. D. Kristmanson, 1979: Tidal energy and sublittoral macrobenthic animals in estuaries. *Journal of the Fisheries Research Board of Canada*, **36,** 1197-1206.

——, 1984: Importance to mussels of the benthic boundary layer. *Canadian Journal of Fisheries and Aquatic Sciences*, **41,** 1618-1625.

Wiles, P., L. A. van Duren, C. Häse, J. Larsen, and J. H. Simpson, 2006: Stratification and mixing in the limfjørden in relation to mussel culture. *Journal of Marine Systems*, **60,** 129-143.

Wiles, P. J., T. P. Rippeth, J. H. Simpson, and P. J. Hendricks, 2006: A novel technique for measuring the rate of turbulent dissipation in the marine environment. *Geophysical Research Letters*, **33,** L21608.

Williams, E. and J. H. Simpson, 2004: Uncertainties in estimates of reynolds stress and tke production rate using the adcp variance method. *J. Atmos. Ocean. Technol.*, **21,** 347-357.